



Norwegian University of  
Science and Technology

# Robust Magnetic Surface Doping of Transition Metal Dichalcogenides

**Mathieu Le Boulvais Børkja**

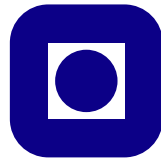
Master of Science in Physics and Mathematics

Submission date: July 2016

Supervisor: Justin Wells, IFY

Norwegian University of Science and Technology  
Department of Physics





NTNU

MASTER'S THESIS

# Robust Magnetic Surface Doping of Transition Metal Dichalcogenides

*Mathieu Børkja*

supervised by  
Justin WELLS

Spring 2016

## Abstract

The growth and potential intercalation of Fe on naturally grown MoS<sub>2</sub> has been studied using a number of surface techniques. An initial sample characterization revealed that samples extracted from the natural MoS<sub>2</sub> crystal contained few impurities and were well suited to the purposes of this experiment. Fe thermally evaporated onto the MoS<sub>2</sub> surface was found to be only weakly interacting with it, easily desorbing during heating. For the quantities of Fe used in this experiment the growth appeared to be uniform. When deposited at room temperature, and when annealed at temperatures up to 100°C, the Fe did not show any signs of having intercalated into the MoS<sub>2</sub>. On Fe dosed samples annealed at higher temperatures (400°C+) ARXPS measurements revealed hints that the Fe may have intercalated. However, due to the amount of Fe that was thermally desorbed in the annealing process, this cannot be concluded with certainty. The Fe was observed to surface dope the sample. It was additionally found that this shift could be reversed by deposition of an alkali metal. A series of preliminary electronic band structure measurements were made on the new hybrid materials. These measurements revealed no clear evidence of band structure alterations due to magnetic effects.

## Sammendrag

Veksten av jern på naturlig grodd  $\text{MoS}_2$  har blitt studert ved bruk av en rekke eksperimentelle overflateteknikker. Spesiell interesse er gitt til muligheten for at jernet kan bli innskutt mellom lagene i det lagvise materialet. En innledende undersøkelse av den naturlige krystallen avslørte at den inneholdt få urenheter og var godt egnet til eksperimentets hensikter. Vekselvirkningen mellom jern termisk fordampet på  $\text{MoS}_2$  overflaten og den samme overflaten viste seg å være svake. Jernet desorberte lett under varmebehandling av prøvene. For de mengdene jern brukt i dette eksperimentet var veksten tilsynelatende uniform. Når jernet ble avsatt på prøven ved romtemperatur, og når det ble utsatt for gløding ved temperaturer opp mot  $100^\circ\text{C}$ , ble det ikke observert noe tegn til innskyting. På lignende prøver utsatt for gløding ved høyere temperaturer ( $400^\circ\text{C}+$ ), viste ARXPS målinger tegn til at jernet mulig hadde blitt innskutt mellom lagene i krystallen. Det er derimot vanskelig å konkludere dette med sikkerhet ettersom mesteparten av jernet ble desorbent i glødingsprosessen. Det ble i tillegg observert at avsetningen av jern overflatedopet prøven. Denne dopingen ble vist å kunne bli reversert gjennom avsetning av et alkalimetall på overflaten. En rekke innledende målinger av det nye hybridmaterialets elektroniske bandstruktur ble også foretatt. Disse målingene viste ingen klare tegn på endringer i bandstrukturen som følge av magnetiske effekter.

## Preface

This thesis is written as the concluding part of a master's degree in Applied Physics at the Norwegian University of Science and Technology (NTNU). The experiments presented in this thesis were performed in two parts. One part in Justin Well's laboratory at NTNU in Trondheim and the other in Phil King's laboratory at St. Andrews University in St. Andrews. All of the experiments, as well as the writing of the thesis itself, were carried out during the spring semester of 2016.

Mathieu Børkja

Trondheim, Spring 2016

## Acknowledgements

I would like to take this opportunity to thank the handful of people whose wisdom and guidance helped shape this project into what it ultimately became. First I would like to extend my gratitude to Dr. Simon Cooil and Dr. Federico Mazzola for their invaluable help in matters both experimental and analytical. I would like to thank my supervisor Justin Wells for his guidance and role in shaping the direction of this project. Also for giving me the opportunity to participate in exciting research both in the Master's degree and in the preceding specialization project. Thanks also to Phil King and his research group for their collaboration with the experiments performed in St. Andrews, as well as for the use of their lab.

Finally I extend a special thanks to fellow master student Kristoffer Hunvik who was part to all the experimental work presented in this thesis.

# Contents

Preface . . . . .	i
Acknowledgements . . . . .	ii
<b>1 Introduction</b>	<b>1</b>
<b>2 Theory</b>	<b>3</b>
2.1 Transition Metal Dichalcogenides . . . . .	4
2.1.1 Spin-orbit Interaction and Valley Degree of Freedom . . . . .	5
2.1.2 Magnetic Doping of TMDCs . . . . .	7
2.1.3 MoS <sub>2</sub> . . . . .	8
2.2 Thin Film Growth . . . . .	9
2.3 Photoelectron Spectroscopy . . . . .	11
2.3.1 XPS . . . . .	23
2.3.2 ARXPS . . . . .	28
2.3.3 UPS . . . . .	30
2.3.4 ARPES . . . . .	32
2.4 Low Energy Electron Diffraction (LEED) . . . . .	35
2.5 Ultra High Vacuum . . . . .	39
<b>3 Procedure</b>	<b>43</b>
3.1 Experimental Setup . . . . .	43
3.2 Sample Preparation . . . . .	53
3.3 Analysis of Experimental Data . . . . .	55
<b>4 Results</b>	<b>59</b>
4.1 Sample Characterization . . . . .	59
4.2 Fe Growth and Intercalation . . . . .	64
4.3 Doping and Counter-doping . . . . .	75
4.4 Preliminary Band Structure Measurements . . . . .	80

<b>5</b>	<b>Discussion</b>	<b>86</b>
5.1	Sample Characterization . . . . .	86
5.2	Fe Growth and Intercalation . . . . .	89
5.3	Film Thickness Estimation . . . . .	92
5.4	Doping and Counter-doping . . . . .	93
5.5	Band Structure Measurements . . . . .	96
5.6	Future work . . . . .	98
<b>6</b>	<b>Conclusion</b>	<b>99</b>
<b>A</b>	<b>Film Thickness</b>	<b>1</b>

# List of Abbreviations

**AES** Auger Electron Spectroscopy.

**AMD** Alkali Metal Dispenser.

**APES** Ambient Pressure Photoemission Spectroscopy.

**ARPES** Angle-resolved Photoemission Spectroscopy.

**ARXPS** Angle-resolved X-ray Photoelectron Spectroscopy.

**CCD** Charge-Coupled Device.

**EAL** Effective Attenuation Length.

**EDC** Energy Distribution Curve.

**ESCA** Electron Spectroscopy for Chemical Analysis.

**FAT** Fixed Analyzer Transmission.

**HAXPES** Hard X-ray Photoelectron Spectroscopy.

**HSA** Hemispherical Sector Analyzer.

**IMFP** Inelastic Mean Free Path.

**LEED** Low Energy Electron Diffraction.

**MDC** Momentum Distribution Curve.

**PES** Photoelectron Spectroscopy.

**SOI** Spin-Orbit Interaction.

**TMDC** Transition Metal Dichalcogenide.

**UHV** Ultra-High Vacuum.

**UPS** Ultraviolet Photoelectron Spectroscopy.

**UV** Ultraviolet.

**XPS** X-ray Photoelectron Spectroscopy.

# Chapter 1

## Introduction

As conventional solid state electronics shrink to ever smaller sizes they run into a number of problems. Be it the increased problem of heat dissipation from charge current or quantum size effects, these issues may well impose a final limit on their dimensions. To circumvent this a host of other potential device applications making use of quantum effects are being explored and developed. Among these are the emerging fields of spintronics and valleytronics. Their purpose is to eventually make devices which make use of spin and the so-called valley degree of freedom, rather than electric charge to carry information. A class of layered materials known as transition metal dichalcogenides (TMDCs) have been attracting much attention for potential use in such devices due to their rich spin and valley physics. The ability to control and tune the spin and valley properties in materials such as these will be of vital importance to the development of spintronic and valleytronic devices. One way through which this can be achieved is by the manipulation of the magnetic properties of the materials. In TMDCs a great potential way to do this is by transition metal doping. Magnetic dopants such as these are of considerable interest because the TMDCs are by themselves intrinsically non-magnetic. Thus the magnetism in the doped material arises nearly exclusively from interactions between the dopants. This enables the tuning of the magnetic interaction simply by varying the dopant concentration and/or the type of dopant. Thermal evaporation of transition metals onto TMDC surfaces provides an expedient and versatile method to perform this doping. However, the adsorption of transition metals to the surfaces makes them highly reactive and prone to oxidation. If these atoms could be made to intercalate to reside in the van der Waals gap between the molecu-

lar layers of the TMDC, this should drastically reduce the surface reactivity while preserving the desired magnetic effects. The latter would of course make the resulting hybrid material much more suitable for potential device applications.

The purpose of this thesis is to investigate the conditions needed to realize such a robust magnetic surface doping of the TMDCs. To this end, this experiment will examine the growth and potential intercalation of iron thermally evaporated onto the surface of MoS<sub>2</sub> using a number of different surface techniques. The dopant depth profile will be monitored before and after annealing the Fe dosed samples to high temperatures. Additionally the possibility of reversing any potential electronic doping effects of the Fe deposition will be explored. This will serve to make any potential changes to the electronic band structure less ambiguously attributable to magnetic effects. Finally preliminary measurements of this band structure will be made. The ultimate goal of this experiment is to enable future, more in depth band structure measurements to be made under varying dopant profiles.

This thesis will begin by explaining certain key concepts relevant to the experiments performed. Special attention will be given to the materials studied as well as the experimental techniques employed in their study. Then will follow a description of certain specifics of the experimental procedure. Following this the results of the investigation will be presented and discussed, before a conclusion is drawn. Each of the major chapters of this thesis will include a brief introduction explaining its purpose and content.

# Chapter 2

## Theory

This chapter will present and explain certain key concepts important to the topic of this thesis. Special attention will be paid to the class of materials studied as well as the experimental techniques used to study them. The first section will also serve to contextualize the experiment within the published literature. Due to the impracticality of a ground-up approach this chapter will assume the reader has a rudimentary understanding of solid state physics.

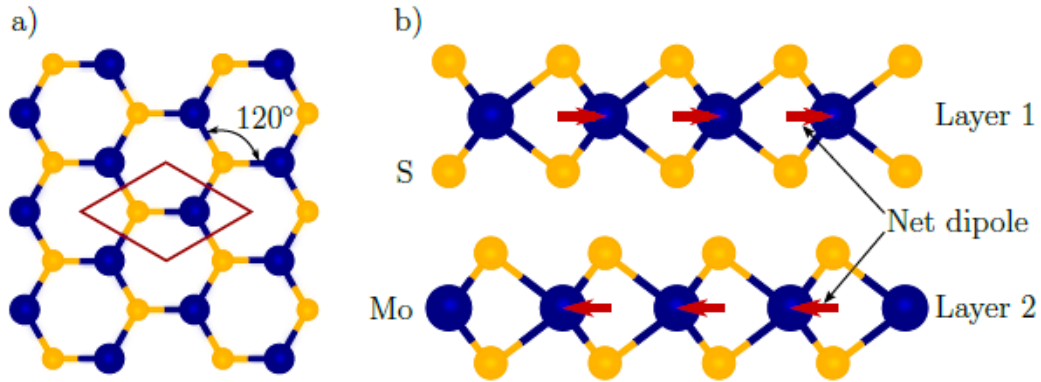


Figure 2.1: Crystal structure of  $\text{MoS}_2$ . a) Top view showing the hexagonal structure of the Mo (blue spheres) and S (yellow spheres) layers. The red rhombus marks the unit cell. b) Side view illustration showing two  $\text{MoS}_2$  layers in the 2H structure. The unit cell contains two S-Mo-S units, each having a net in plane dipole (marked by the red arrows) in opposite directions.

## 2.1 Transition Metal Dichalcogenides

Transition metal dichalcogenides (TMDCs) are a class of layered materials that have long been studied for their mechanical[1], optical and electronic properties[2]. In more recent times the discovery of graphene by mechanical exfoliation of graphite[3] has kindled a resurgence of scientific and engineering interest in layered materials, especially in their single layer, two dimensional forms. Once thought to be unstable due to thermal fluctuations[4, 5], these 2D materials have since proven host to a variety of exotic physics with wide ranging potential applications[6]. Among the layered materials, TMDCs with their variety of properties ranging from metallic, to semiconducting, to superconducting, have received particular interest.

TMDCs have a general chemical formula of  $\text{MX}_2$ , where M is a transition metal atom (e.g. Mo, W, Ti, Zr, Ta, Nb) and X is a chalcogen atom (e.g. S, Se, Te). Each layer of these materials consists of covalently bonded X-M-X networks having a  $D_{3h}^1$  space group as shown in Figure 2.1. This figure shows the crystal structure of  $\text{MoS}_2$ , the most common of the TMDCs. Its structure is analogous to that of the other materials of this class. The bulk form of the TMDCs is made up by the stacking of such two dimensional layers, bound only by relatively weak van der Waals interactions. This weak inter-layer bonding means that each of the layers making up the bulk can be considered

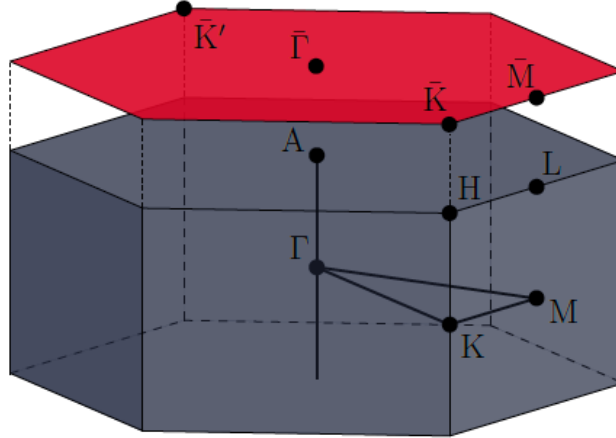


Figure 2.2: First Brillouin zone of MoS<sub>2</sub> with points of high symmetry marked on the figure. Both the bulk (blue) and surface (red) Brillouin zones are represented.

quasi two dimensional systems. Consequently TMDCs are highly anisotropic materials, having different properties in in-plane and out-of-plane directions. While several different bulk phases exist, made up by stacking the layers in different ways[7], this thesis will mainly concern itself with the so-called 2H polytype. This bulk phase, depicted in Figure 2.1 b), has a bilayer unit cell with space group  $D_{6h}^4$ . The reciprocal lattice of the TMDCs preserves the hexagonal symmetry of the real space lattice. Figure 2.2 shows the bulk and surface Brillouin zone of MoS<sub>2</sub> and labels the points of high symmetry. These labels are frequently used to specify crystallographic directions. Note that the points of high symmetry of the surface Brillouin zone are distinguished from those of the bulk Brillouin zone by the addition of a bar (e.g.  $\bar{\Gamma}$  as opposed to  $\Gamma$ ).

### 2.1.1 Spin-orbit Interaction and Valley Degree of Freedom

What truly sets TMDCs apart from other two dimensional materials is their strong spin-orbit interaction. The spin-orbit interaction (SOI), alternatively spin-orbit coupling, is a relativistic effect arising from the coupling of a particle's spin  $\mathbf{s}$  with its momentum  $\mathbf{p}$  under an external electric field  $\mathbf{E}$ . To give an idea of the factors influencing the SOI it is useful to note that it can

be described by the SOI Hamiltonian[8]

$$\hat{H}_{so} = -\mu_B \boldsymbol{\sigma} \cdot (\mathbf{p} \times \mathbf{E}/2mc^2). \quad (2.1)$$

Here  $\mu_B$  is the Bohr magneton,  $\boldsymbol{\sigma}$  the spin Pauli matrices,  $m$  the effective mass of the carriers and  $c$  the speed of light. Clearly, the strength of the interaction depends on the effective magnetic field  $\mathbf{B}_{\text{eff}} = (\mathbf{p} \times \mathbf{E}/2mc^2)$  and consequently on  $\mathbf{p}$  and  $\mathbf{E}$  and their relative orientations[9, 10]. This interaction is particularly important for TMDCs because of the strong spin-orbit coupling of the  $d$  orbitals of the transition metals.

In non-magnetic centrosymmetric materials, such as the bulk 2H phase of TMDCs, the combination of inversion symmetry and time-reversal symmetry ensures that its electronic states must be doubly spin degenerate. If inversion symmetry is broken, however, the SOI can lift this degeneracy at generic  $k$ -points in the Brillouin zone and induce a momentum-dependent spin splitting. Further, it can lead to the emergence of a number of potential effects such as for example the spin Hall effect[11] or the spin-galvanic effect[12]. The inversion symmetry can be broken in a couple of different ways. One way it can be done is to apply an external electric field to create a non-centrosymmetric potential well at semiconductor heterointerfaces. This has been shown to lead to Rashba-type[10] spin splitting of electronic states around high symmetry points in the Brillouin zone with a momentum-dependent in-plane spin polarization[13, 14, 15]. As can be seen from Figure 2.1, the inversion symmetry of TMDCs is broken when going from the bulk to the monolayer form. Hints on the nature of the spin splitting in these monolayers can be gleaned from Equation 2.1. Here the electric field  $\mathbf{E}$  is dominated by an internal electric dipole field imposed by the net in-plane dipole in each structural unit (marked by red arrows in Figure 2.1 b)). Being a two dimensional material,  $\mathbf{p}$  is also primarily confined to in-plane directions, meaning that the effective magnetic field  $\mathbf{B}_{\text{eff}}$  must be largely perpendicular to the plane. In WSe<sub>2</sub>[8, 16] and MoS<sub>2</sub>[17, 18, 19] this has been shown to give rise to a Zeeman-type spin splitting and an out-of-plane spin polarization at and around the corners ( $\bar{K}$  points) of the Brillouin zone. Due to time-reversal symmetry this polarization will have an alternating sign at opposite corners ( $\bar{K}$  and  $\bar{K}'$ ). Recently, however, a similar spin polarization has been observed in globally centrosymmetric materials in which constituent structural units break inversion symmetry[20, 21, 22], among these both WSe<sub>2</sub> and NbSe<sub>2</sub>. These properties, along with the possibility of controlling them,

make TMDCs prime candidates for spintronic devices (i.e. devices that use spin to carry signals).

In addition to this rich spin texture TMDCs show great potential for offering yet a different type of device functionality. Certain materials, TMDCs included, display conically shaped "valleys" in their electronic band structure. When two such valleys exist at the same energy but at different locations in momentum-space the system gains an additional quantum number known as the valley index. The existence of these kinds of valleys makes it possible to confine electrons, not into a specific location, but to a preferred momentum, effectively channeling the flow of charge in a particular direction. Valleytronic devices aim to make use of this valley degree of freedom in valley based electronic applications. An important part to realizing such devices is the ability to localize electrons to one momentum valley. Also referred to as valley polarization, this has been proposed and achieved in both graphene[23, 24] and TMDCs[25, 26].

TMDCs, however, display two important differences from graphene that may prove significant to the development of valleytronic devices. First is the explicit breaking of inversion symmetry in the TMDC monolayers. This can lead to both the emergence of a valley Hall effect[23] as well as valley-dependent optical selection rules for interband transitions at K points[27]. The second difference is again the strong SOI in TMDCs which has been shown to lead to coupled spin-valley physics[19]. This has been predicted[17] and shown[21, 28] to give rise to valley-dependent spin polarization. Furthermore, this spin-valley locking has been shown to play a significant role in superconductivity in ion-gated MoS<sub>2</sub>[18].

### 2.1.2 Magnetic Doping of TMDCs

The ability to tune and control these interactions will be of crucial importance to the development of novel device applications. One promising way to achieve this in the TMDCs is by manipulating their magnetic properties. Although intrinsically non-magnetic, several methods aiming to introduce stable magnetism in two dimensional materials have been proposed and explored[29]. It has been shown that grain boundaries and dislocations in TMDCs display a substantial magnetic moment[30]. This type of magnetization can further be induced by proton irradiation[31]. There are a couple of drawbacks to this method, however. First of all, the resulting magnetization depends strongly on the defect configurations. Second, in order to

achieve large system magnetism it is necessary to introduce a large number of defects to the systems. The latter may reduce carrier mobility within the layer due to the formation of scattering centers and charge-trapping sites. A different method shown to induce strong ferromagnetism in MoS<sub>2</sub> is through surface functionalization, specifically by hydrogenation[32]. Although the magnetism produced from this method is stable, experimentally achieving this result is not straightforward. Realizing the surface hydrogenation of the MoS<sub>2</sub> requires an external stress applied to it. Yet a different method is by cutting the two dimensional material into one dimensional nanoribbons. This has been proposed and achieved for MoS<sub>2</sub>[33, 34]. Again, however, these nanoribbons are difficult to prepare experimentally, further complicated by the fact that depending on their edge type not all nanoribbons are magnetic. The final method which will be discussed, and which was adopted for this experiment, is by far the most conventional and easy way to induce stable magnetism in 2D systems: doping by transition metals[35, 36]. Because the TMDCs are by themselves non-magnetic, magnetic dopants are a particularly interesting choice. The resulting magnetism in the doped TMDC will arise primarily from interactions between dopants. Consequently, the strength of the magnetic interactions in the system can be tuned by varying the dopant concentration.

TMDCs doped in this way have been shown to harbor a number of interesting properties and effects. For example, Mn doping of monolayer MoS<sub>2</sub> has been predicted to induce ferromagnetism[37]. Magnetically doped TMDCs have also been proposed as candidates for two dimensional dilute magnetic semiconductors[37, 38]. Additionally, the introduction of a magnetic field will break time-reversal symmetry in the material and thus it can lift the K/K' valley degeneracy. Although it has been demonstrated that valley polarization in MoS<sub>2</sub> can be induced from optical pumping with circularly polarized light[26], an equilibrium valley polarization would be far more useful in device applications. This has been achieved in the same material through magnetic doping[39].

### 2.1.3 MoS<sub>2</sub>

MoS<sub>2</sub> or molybdenite, is the most common of the TMDCs and the only one occurring naturally in any significant quantities. Natural MoS<sub>2</sub> can grow in both the 2H and 3R polytypes, or in some combination of the two[40]. The 2H polytype, however, is by far the most common[41], with the 3R polytype

often appearing in conjunction with a telling impurity. In its bulk form MoS<sub>2</sub> is an indirect gap semiconductor with a band gap of 1.29eV[42]. Going over to its monolayer form, it transitions into a direct gap semiconductor with a band gap of 1.8eV.

MoS<sub>2</sub> was chosen for this experiment over other TMDCs in part for its abundance due to its natural occurrence. More importantly, however, it was chosen because of its rich spin and valley texture[17, 19, 18, 25, 26, 28], and for the many potential effects of magnetically doping it[35, 37, 38, 39]. It is expected to share many properties with the other group VI transition metal dichalcogenides (e.g MoSe<sub>2</sub>, WS<sub>2</sub>, WSe<sub>2</sub>), particularly as regards to surface chemistry.

## 2.2 Thin Film Growth

The study of thin films and their growth has long been a topic relevant in many diverse contexts. Thin films have a multitude of technological applications ranging from optical coatings to more advanced semiconductor devices. They are also of considerable importance to surface science, particularly to the development and study of low-dimensional materials. Understanding and controlling the growth of thin films is thus a problem that has been the subject of much research.

A thin film is a layer of material deposited on a substrate with a thickness anywhere between fractions of a nanometer to several micrometers. The synthesis of such films typically proceeds through nucleation and several growth stages, the precise nature of which depends on a number of atomic processes at the surface. Generally, however, the growth of thin films are divided into three basic modes as shown in Figure 2.3[43, 44, 45].

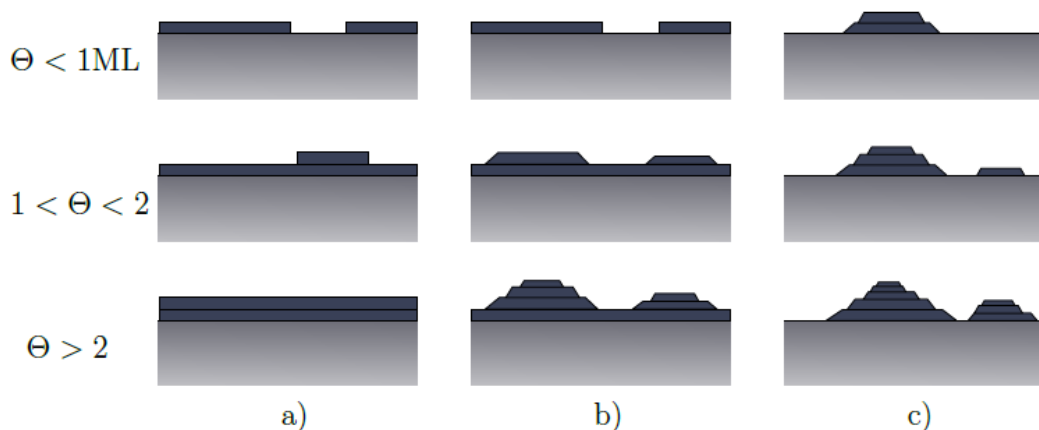


Figure 2.3: Illustration of the three basic growth modes: (a) layer growth, (b) layer followed by island growth, (c) island growth.  $\Theta$  is the coverage in monolayers.

In the layer mode (Figure 2.3 a)) the first atoms deposited will condense to form a complete monolayer on the surface. A second layer will grow once the first monolayer has formed. This growth mode happens when the atoms being deposited are more strongly bound to the substrate than they are to each other.

In the opposite case, i.e. when the atoms are more strongly bound to each other than to the substrate, the island mode (Figure 2.3 c)) is observed. Here the atoms will form small clusters on the surface directly from the condensation and subsequently grow into 3D crystallites or islands.

The layer followed by island mode (Figure 2.3 b)) is an intermediate case. Initially one or several monolayers are formed on the surface, followed by island growth on top of this. This happens when the formation of the first layers changes the growth conditions in such a way that island growth is more energetically favorable than continued layer growth.

Additional factors which can influence thin film growth are the presence of surface defects in the substrate and the possibility of interdiffusion. Surface defects (e.g. edge or screw dislocations) are important because they alter the chemistry of the surface. TMDCs provide an interesting example of this. While the surface of these materials is relatively inert, several studies[46, 47, 48] have shown that the introduction of defects creates sites with enhanced reactivity. One might expect that these will tend to serve as nucleation

sites and indeed it has been observed that several materials (e.g. alkali metals[49, 50] and Fe[51]) form clusters centered around such defects.

When growing thin films on layered materials such as TMDCs or graphite there is the added possibility for intercalation. The weak inter-layer bonding in these materials makes it so that many compounds on the surface readily intercalate to reside in the van der Waals gap between layers. The likelihood of a given element intercalating depends both on the element and the substrate. In the case of TMDCs it also depends on the layer structure and number of layers.

## 2.3 Photoelectron Spectroscopy

Photoelectron spectroscopy (PES), or alternatively photoemission spectroscopy, is a general term for techniques which make use of the photoelectric effect to investigate properties of matter. There exists a wide range of such techniques which each serves as a powerful tool in the study of the characteristics of atoms, molecules, solids and surfaces. The photoelectric effect is a phenomenon, first detected by Hertz[52] in 1887, by which light incident on a material can cause electrons to be emitted. In 1905 Einstein explained the effect in his Nobel prize winning work[53] by invoking the quantum nature of light. He proposed that light rather than having its energy continuously distributed in space as it does in the wave theory of light, it instead consists of a finite number of energy quanta localized in space. When incident on a material these quanta, or photons as they have since been named, can be absorbed by an electron in the material causing it to be ejected with a maximum kinetic energy,  $E_{kin}$ , given by

$$E_{kin} = h\nu - \phi. \quad (2.2)$$

Here  $h$  is Planck's constant,  $\nu$  is the photon frequency and  $\phi$  is a material specific quantity known as the work function. Note that electrons emitted through the photoelectric effect are commonly referred to as photoelectrons. The work function of a solid is defined as the energy difference between the Fermi level and the vacuum level. For a metal this is equivalent to the minimum energy required to remove an electron from the solid to a point in the vacuum immediately outside the surface (or infinitely far away from the surface depending on the definition). Metals typically have a work function of around 4-5eV.

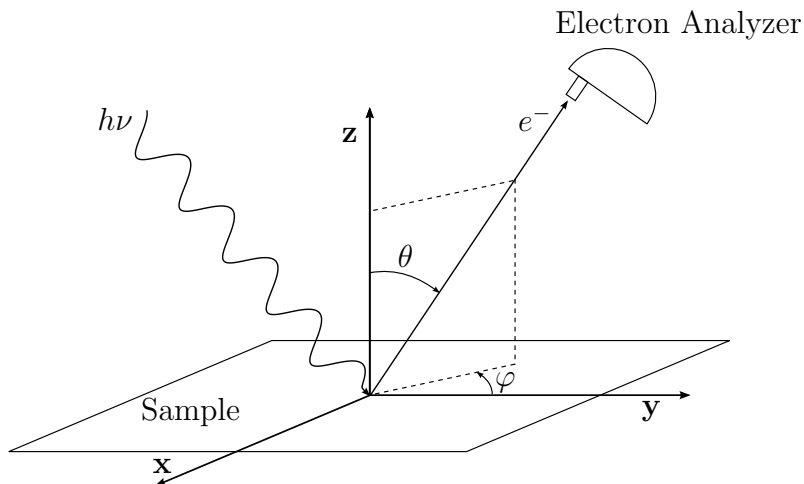


Figure 2.4: Basic geometry of a PES experiment. A photon incident on a sample knocks loose an electron by the photoelectric effect. This photoelectron is then collected in an electron analyzer and its kinetic energy is measured. The emission direction of the photoelectron is specified by the polar ( $\theta$ ) and the azimuthal ( $\varphi$ ) angles.

Figure 2.4 shows the basic geometry of a PES experiment. A quasi-monochromatic beam of photons is directed at a sample. At the sample the incident photons may be absorbed and in turn knock loose electrons by the photoelectric effect. After being emitted from the surface, the photoelectrons are collected by an electron energy analyzer with a finite acceptance angle. In this way it is possible to measure the kinetic energy of the photoelectron at a given emission direction.

As a side note: If the sample is not grounded, or is non-conductive, the depletion of electrons at the surface caused by repeated photoemission events will cause the surface to gain a net positive charge. This will change the potential at the surface and consequently the kinetic energy of the electrons escaping the material. In conductive samples this problem is avoided by placing the sample in contact with a source of electrons, usually the ground of the measurement system. In non-conductive samples the charging must be accounted for in some other way[54, 55].

The kinetic energy, along with the polar ( $\theta$ ) and azimuthal ( $\varphi$ ) emission angles, uniquely determines the momentum  $\mathbf{k}$  of the photoelectron in vacuum. Using this knowledge to determine the characteristics of the electrons

as they were inside the solid is then the problem of photoemission theories.

The complexity of the photoemission process presents a considerable challenge to the formulation of an exact photoemission theory. As such, quantitative analysis is typically done using various simplifying assumptions. Two of the most common of which, namely the three-step model and the sudden approximation, will be briefly discussed in this section. First, however, a couple of key arguments can be made from conservation laws and symmetry.

Consider a photon incident on an  $N$ -electron system. The quantum mechanical picture of a photoemission event is a single-step process. An illustration of the process can be seen on the right hand side of Figure 2.7. It is an optical transition from an initial state,  $\psi_i$ , one of the possible  $N$ -electron eigenstates of the system, to a final state,  $\psi_f$ , one of the possible  $(N - 1)$ -electron eigenstates of the now ionized solid. In order to account for the escaping photoelectron  $\psi_f$  must also contain a propagating plane wave with a finite amplitude inside the solid (The so called inverse Low Energy Electron Diffraction[56, 57] wave function is often used for  $\psi_f$ ). The latter is necessary in order for there to be some overlap between the initial and final state. In addition to this, the process must obey certain conservation laws of energy and momentum. First, conservation of energy requires that

$$E_f - E_i = h\nu, \quad (2.3)$$

where  $E_f$  and  $E_i$  are the energies of the final and the initial states of the system. Meaning simply that the total energy change in the system cannot exceed the energy supplied to it by the photon. Second, conservation of momentum requires that

$$\mathbf{k}_f - \mathbf{k}_i = \mathbf{k}_{h\nu}, \quad (2.4)$$

where  $\mathbf{k}_f$ ,  $\mathbf{k}_i$  and  $\mathbf{k}_{h\nu}$  are the momenta of the system in the final state, the system in the initial state, and of the photon respectively. Since the momentum of the photon in most cases relevant to PES is small compared with electron momenta, it can often safely be neglected.

Using conservation of energy, combining Equation 2.3 and Equation 2.2, provides a way to relate the kinetic energy of the photoelectron in vacuum to the binding energy,  $E_B$ , of the electronic state in the solid:

$$E_{kin} = h\nu - \phi - |E_B| \quad (2.5)$$

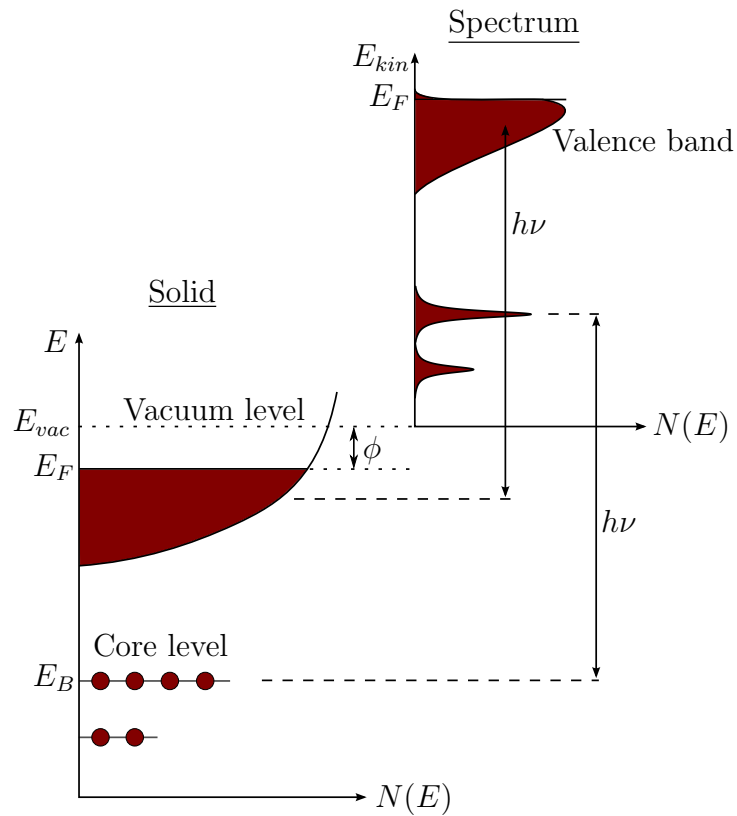


Figure 2.5: Illustration of the energies involved in photoelectron spectroscopy. It shows the relation between the energy levels in a solid and the electron energy distribution produced by photons of energy  $h\nu$ . The solid, a metal in this case, has core levels and a valence band. Figure adapted from Hüfner[57].

The binding energy is a measure of the energy required to remove the electron from the solid and is defined with reference to the Fermi level, i.e.  $E_B = 0$  at  $E_F$ . Figure 2.5 depicts the energy level diagram of a solid, a metal in this case, and the related energy distribution of photoemitted electrons. The Fermi level is located at the top of the valence band, separated from the vacuum level,  $E_{vac}$ , by the work function. It should be mentioned that Equation 2.5 is only valid under the assumption of non-interacting electrons. Meaning that any energy the photoelectron might gain or lose as a result of many-body interactions would need to be added to or subtracted from the right hand side of the equation.

Naturally the resulting spectrum of photoelectrons depends on the photon energy,  $h\nu$ , used to create it. It can be seen, for example, that for an electron with binding energy  $E_B$  to be photoemitted, the photon must supply to it at least an energy  $h\nu > |E_B| + \phi$ . This means that using different photon energies permits accessing different parts of the spectrum. Indeed, many PES techniques are named with reference to the ionization source used, the archetypal examples being XPS and UPS. X-ray photoelectron spectroscopy or XPS uses high energy photons ( $\approx 100 - 10000eV$ ) to study primarily electronic core levels, which can yield a wealth of information for elemental and chemical analysis. Ultraviolet photoelectron spectroscopy or UPS on the other hand uses low energy photons ( $\approx 7 - 60eV$ ) to study primarily valence states which offer information on electronic structure and bonding.

Another consequence of the energy range involved in PES experiments is the resulting short inelastic mean free path (IMFP) of the photoelectrons. The inelastic mean free path is a material parameter and is a measure of how far an electron can travel, on average, through a material before it is scattered inelastically. More specifically it can be defined as the distance an electron beam can travel before its intensity decays to  $1/e$  of its initial value. Figure 2.6 shows how the IMFP varies with the kinetic energy of electrons. It is called the "universal" IMFP curve because although the kinetic energy dependence is different from element to element (the black dots in Figure 2.6 each represents a different material or transition) it tends to follow a similar trend. This is because the inelastic scattering of electrons in this energy range mostly involves excitations of conduction electrons, and the density of conduction electrons is similar for the elemental solids[59]. The short IMFP has a profound impact on all photoemission experiments. Considering electrons that escape a solid parallel to the sample normal it means that approximately 65% of the collected signal will come from a depth of less than the IMFP,

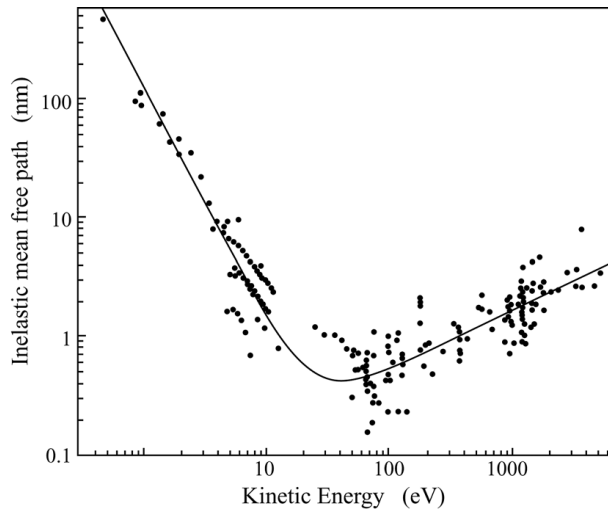


Figure 2.6: The "universal" inelastic mean free path curve. It shows the kinetic energy dependence of the inelastic mean free path of excited electrons in solids. Figure taken from Seah, M.P. and Dench, W.A.[58].

85% from less than twice the IMFP, and 95% from less than thrice the IMFP. Although the incoming photons can excite photoelectrons much further down in the sample (on the order of microns for X-rays) only electrons emitted within a few layers of the surface escape without losing significant amounts of energy. This is what makes PES surface sensitive; the IMFP determines the effective probing depth of the technique. In UPS, for example, the photoelectrons will typically have a kinetic energy of around 10 – 15eV. From Figure 2.6 it can be seen that such electrons have an IMFP of about 1nm. Meaning that UPS as a technique is only sensitive to electrons emanating from the first few atomic layers of the sample. Of course, techniques employing higher energy ionization sources will have longer probing depths. Take for instance hard X-ray photoelectron spectroscopy (HAXPES), which uses photon energies in the range 2 – 15keV. It can have probing depths from 30 – 100Å, making it more sensitive to bulk properties and less sensitive to surface effects.

The high surface sensitivity of PES makes it reliant on samples having clean (atomically clean in many cases) surfaces as any contaminants will affect the measurements. This restriction means that PES must be performed under high vacuum conditions. Otherwise the sample might become too

contaminated in the matter of minutes or even seconds (depending on the type of sample of course). Another reason, and the most important, why PES must be performed in vacuum is that electron energy analyzers only work under high vacuum conditions. The inelastic scattering of electrons between when they leave the sample and when they are finally detected would cause too much of the signal to be lost and introduce too much noise. It should be mentioned that several systems capable of ambient pressure photoemission spectroscopy (APPES) have been built[60, 61, 62], notably at the synchrotron light sources ALS in Berkeley and BESSY in Berlin. These systems rely on clever pumping schemes that allow the sample to be in a higher pressure environment while still keeping the electron energy analyzer in vacuum conditions.

Returning to the conservation laws, this time to see what can be gleaned about the electron's momentum in the sample. Assuming a smooth sample surface, translational symmetry in the  $x$ - $y$  plane (specified by the axes in Figure 2.4) requires that the component of the electron momentum parallel to the surface,  $\mathbf{k}_{\parallel}$ , must be conserved. With the knowledge that  $E_{kin} = \frac{\mathbf{p}^2}{2m}$ , where  $m$  is the electron mass, and  $\mathbf{k} = \frac{\mathbf{p}}{\hbar}$  it can be seen directly from Figure 2.4 that:

$$\mathbf{k}_{\parallel} = \frac{1}{\hbar} \sqrt{2mE_{kin}} \sin \theta, \quad (2.6)$$

both for the electron inside the solid and for the freed photoelectron. The same argument cannot be made for the component of the momentum perpendicular to the surface,  $\mathbf{k}_{\perp}$ . In this direction there is no translational symmetry, and  $\mathbf{k}_{\perp}$  is not conserved. It loses parts of its energy and momentum to overcome the surface potential. To determine this component it is necessary to either use methods requiring supplemental data or to make additional assumptions. One approach is to assume that the final in-crystal electron states are nearly-free electron states[63] which gives as a final result

$$\mathbf{k}_{\perp} = \frac{1}{\hbar} \sqrt{2m(E_{kin} \cos^2 \theta + V_0)} \quad (2.7)$$

where  $V_0$  is the inner potential. It is defined as the energy difference between the bottom of the valence band and the vacuum level. This step introduces a certain amount of uncertainty to  $\mathbf{k}_{\perp}$  depending on how appropriate the methods used/assumptions made are to the materials studied. The uncertainty in  $\mathbf{k}_{\perp}$  is, however, less relevant for certain systems. Particularly for

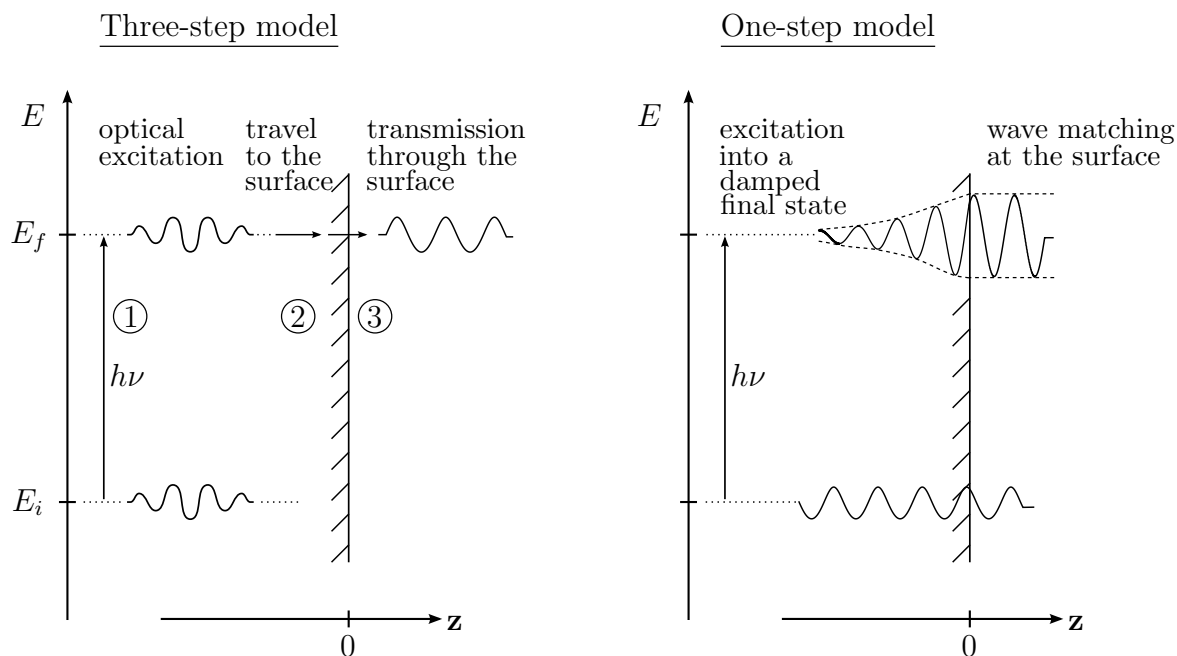


Figure 2.7: Schematic of the three-step model as contrasted to the one-step model. In the three-step model, depicted on the left, the photoemission process is divided into three independent steps: 1) optical excitation of an electron inside the solid, 2) travel of the photoelectron to the surface, and 3) Transmission of the photoelectron through the surface potential barrier and escape into vacuum. On the right the more accurate one-step model is depicted. Figure from Hüfner[57].

low dimensional, anisotropic systems with low dispersion along the surface normal. In this case the electronic dispersion is determined primarily by  $\mathbf{k}_{\parallel}$ .

Clearly, much can be learned from PES using only a handful of relatively simple considerations. In many cases, however, it can be quite helpful, even necessary, to calculate the photoemission intensity in order to understand the finer points of an acquired spectrum. To this end a more formal quantum mechanical description is necessary.

### Three-Step Model

As mentioned earlier the photoemission process should realistically be described as a single-step process[64]. In many cases, due to the complexity

of the one-step model, the conceptually simpler three-step model is used instead. Figure 2.7 shows illustrations of both the three-step model and the one-step model. The three-step model is an approximation introduced by Berglund and Spicer[65] that, despite being considered crude by some, has proved extremely useful. It consists of breaking the photoemission process into three independent steps:

1. Photoionization: a photon is absorbed and an electron is excited.
2. Travel of the photoelectron to the surface.
3. Transmission of the photoelectron through the surface potential barrier and escape into vacuum.

The resulting photoemission intensity, or photocurrent, is then proportional to the product of the probabilities corresponding to each step. Let the total probability for the optical transition be represented by  $P(E_{kin}, h\nu)$ , the scattering probability for the travelling photoelectron by  $T(E_{kin}, h\nu)$ , and the transmission probability through the surface by  $D(E_{kin})$ . The photoemission intensity,  $I$ , is then

$$I \propto P(E_{kin}, h\nu) T(E_{kin}, h\nu) D(E_{kin}). \quad (2.8)$$

The first part,  $P(E_{kin}, h\nu)$ , contains all the information on the electronic states of the solid in the initial state. The second part,  $T(E_{kin}, h\nu)$ , includes information on the inelastic scattering processes that can affect the photoelectron, and can be described in terms of an effective mean free path related to the IMFP discussed previously. A notable way in which this step manifests itself in photoemission spectra is by the continuous background formed by inelastically scattered electrons. The third part,  $D(E_{kin})$ , depends on the energy of the photoelectron and of the material work function. Practically it imposes the condition

$$\frac{\hbar^2 \mathbf{k}_\perp^2}{2m} \geq |E_0| + \phi, \quad (2.9)$$

where  $\hbar$  is the reduced Planck's constant and  $|E_0|$  is the energy of the bottom of the valence band referenced to the Fermi level. If this is not fulfilled, then no transmission is possible.

Treating the interaction with the photon as a small perturbation, the probability of an optical transition between an  $N$ -electron ground state  $\psi_i^N$

and one of the possible final states  $\psi_f^N$  is denoted  $w_{fi}$  and can be approximated by Fermi's golden rule:

$$w_{fi} = \frac{2\pi}{\hbar} |\langle \psi_f^N | \Delta | \psi_i^N \rangle|^2 \delta(E_f^N - E_i^N - h\nu). \quad (2.10)$$

The delta function is included to impose conservation of energy and  $E_i^N$  and  $E_f^N$  are the initial and final state energies of the  $N$ -electron system.  $\Delta$  is the perturbation which can be expressed as

$$\Delta = \frac{e}{2mc} (\mathbf{A} \cdot \mathbf{p} + \mathbf{p} \cdot \mathbf{A}) - e\phi, + \frac{e^2}{2mc^2} \mathbf{A} \cdot \mathbf{A} \quad (2.11)$$

where  $c$  is the speed of light,  $e$  is the elementary charge,  $\mathbf{A}$  and  $\phi$  are the vector and scalar electromagnetic potentials respectively, and  $\mathbf{p}$  is the momentum operator  $\mathbf{p} = i\hbar\nabla$ . This expression can be simplified using a couple of assumptions. First, it is always possible to choose a gauge such that the scalar potential  $\phi = 0$ . Second, using the commutation relation  $[\mathbf{p}, \mathbf{A}] = -i\hbar\nabla \cdot \mathbf{A}$ :

$$\mathbf{A} \cdot \mathbf{p} + \mathbf{p} \cdot \mathbf{A} = 2\mathbf{A} \cdot \mathbf{p} + i\hbar(\nabla \cdot \mathbf{A}). \quad (2.12)$$

The term  $\nabla \cdot \mathbf{A}$  disappears under the dipole approximation. That is that  $\mathbf{A}$  is constant over atomic dimensions, in which case  $\nabla \cdot \mathbf{A} = 0$ . Note that this assumption is not always valid, particularly at the surface where the dielectric constant changes going from the surface and to the vacuum. This gives rise to a number of surface effects such as, for example, the surface photoelectric effect[66]. Finally, restricting the calculation to first-order perturbation theory, effectively neglecting the term of order  $|\mathbf{A}|^2$  which represents two-photon processes, the perturbation reduces to

$$\Delta = \frac{e}{mc} \mathbf{A} \cdot \mathbf{p}. \quad (2.13)$$

While the three-step model is useful it has a couple of obvious shortcomings. First, it tends to focus most of the attention on the first step, the excitation, and as a result neglect the remaining two steps, the scattering and the transmission. In cases where the latter become important, e.g. when photoelectron diffraction effects come into play such as in photoelectron holography[67], the model might be less applicable. Further, despite dedicating one of the three steps to the surface, the model fails to account for many

of the ways the presence of a surface affects the photoemission spectrum. As an example it does not differentiate the electronic structure of the surface layers from that of the bulk. The former of which will always be different because of the symmetry breaking at the surface. Finally, as photoemission is a single quantum mechanical process each of the three steps modelled in the three-step model can interfere with each other. The three-step model is most reliable in cases where the independent particle model is applicable, and more so for higher photon energies.

## Sudden Approximation

The sudden approximation[68] deals with a complication that arises in the first step of the three-step model. During the photoexcitation process the remaining  $(N - 1)$ -electron system is left in an excited state. When the system subsequently relaxes it can affect the electron on its way out of the solid. In the sudden approximation it is assumed that the electron removal is sudden, or in other words, that the effective potential of the system changes discontinuously at the instant of optical excitation. This approximation works best when the escape time of the photoelectron is much lower than the relaxation time of the system. Meaning that it is more accurate when applied to higher kinetic energy electrons.

A main advantage of the sudden approximation is that it makes it possible to decouple the photoelectron from the remaining solid in the final state  $|\psi_f^N\rangle$ :

$$\psi_f^N = \mathcal{A} \phi_f^{\mathbf{k}} \psi_f^{N-1}. \quad (2.14)$$

Here  $\phi_f^{\mathbf{k}}$  is the wavefunction of the photoelectron with momentum  $\mathbf{k}$  and  $\psi_f^{N-1}$  is the final state of the  $(N - 1)$ -electron system. The antisymmetric operator  $\mathcal{A}$  ensures that the  $N$ -electron wavefunction satisfies the Pauli-principle. In a similar way it is possible, using Hartree-Fock formalism, to factorize the initial state into a one-electron orbital  $\phi_i^{\mathbf{k}}$  and an  $(N - 1)$ -particle term such that

$$\psi_i^N = \mathcal{A} \phi_i^{\mathbf{k}} c_{\mathbf{k}} \psi_i^{N-1} = \mathcal{A} \phi_i^{\mathbf{k}} \psi_i^{N-1}, \quad (2.15)$$

where  $c_{\mathbf{k}}$  is an annihilation operator for an electron with momentum  $\mathbf{k}$ . If  $\psi_f^{N-1}$  is chosen to be an excited state with eigenfunction  $\psi_m^{N-1}$  and energy  $E_m^{N-1}$ , the matrix elements in Equation 2.10 can be rewritten as:

$$\langle \psi_f^N | \Delta | \psi_i^N \rangle = \langle \phi_f^{\mathbf{k}} | \Delta | \phi_i^{\mathbf{k}} \rangle \langle \psi_m^{N-1} | \psi_i^{N-1} \rangle. \quad (2.16)$$

This gives for the total photoemission intensity

$$I(\mathbf{k}, E_{kin}) = \sum_{f,i} w_{fi} \quad (2.17)$$

$$= \sum_{f,i} |M_{f,i}^{\mathbf{k}}|^2 \sum_m |c_{m,i}|^2 \delta(E_{kin} + E_m^{N-1} - E_i^N - h\nu) \quad (2.18)$$

where  $M_{f,i}^{\mathbf{k}} = \langle \phi_f^{\mathbf{k}} | \Delta | \phi_i^{\mathbf{k}} \rangle$  is the dipole matrix element and  $|c_{m,i}|^2 = |\langle \psi_m^{N-1} | \psi_i^{N-1} \rangle|^2$  is the probability that a photoexcitation event from an initial state  $i$  will leave the system in the excited state  $m$ .

The main drawback to using the sudden approximation is that all extrinsic losses are neglected. An extrinsic loss, in the context of the three-step model, refers to any energy loss the photoelectron might suffer after the first step.

## Line width and Resolution

As depicted in Figure 2.5 the experimental spectrum of a given energy level in a solid will not be sharply localized at a single energy. Instead it will have some finite width and shape determined by a number of natural and experimental factors. The most fundamental contribution to the line width comes from lifetime broadening arising as a result of the time-energy uncertainty principle. Because the photohole left behind in the photoemission process has a finite lifetime, the binding energy of the state can not be measured with arbitrary precision. This effect will, due to the physics involved, add a Lorentzian contribution to the line shape[69]. A point which will be interesting later is that valence hole states are generally much longer lived than core hole states. In most cases, excluding surface states, the lifetime of the photoelectron in the solid also contributes to the broadening, reflecting final state scattering processes. The photoemission peak will further be affected by the thermal broadening of the ground state, adding a roughly Gaussian component to the line shape with a width of about  $\approx 0.1\text{eV}$ . Additionally, the shape can be affected by various many body correlations[70] both in the initial and final states.

On the experimental side one of the most important factors that contribute to the line width of peaks in the spectrum is the line width of the exciting radiation. The spectrometer resolution is attributable to a combination of various stochastic effects and thus add a Gaussian component to

the line shape. Finally, all peaks in photoemission spectra will have a "tail" on the lower kinetic energy side due to inelastically scattered electrons.

### 2.3.1 XPS

X-ray photoelectron spectroscopy (XPS) is a powerful experimental technique used for elemental and chemical analysis. Although the technique has been developed in increments since the discovery of x-rays and the photoelectric effect at the beginning of the 20th century, much of the work on high resolution XPS was done by Kai Siegbahn and his research group[71] in Uppsala, Sweden in the years following the second world war. Siegbahn received the 1981 Nobel prize for his efforts in developing XPS in its modern form, which he and his colleagues referred to as electron spectroscopy for chemical analysis (ESCA).

In broad terms XPS consists of irradiating a sample with x-rays (photons in the energy range 100eV to 10keV) and measuring the kinetic energy of the emitted photoelectrons. The relatively high energy of the employed photons means that it is well suited for, and indeed most often used for, core level spectroscopy. That is to say measuring the kinetic energy distribution of photoelectrons excited from core electron states (see Figure 2.5). Doing this makes it possible to identify which elements, and in what relative quantities, are present at the surface of the sample, seeing as each element gives rise to a characteristic set of peaks in the XPS spectrum. Furthermore, the energy at which a peak is located also provides information about the chemical environment of the species present because the nature of the environment gives rise to well defined energy shifts. These are called chemical shifts and have their origin in either initial state or final state effects[72]. Initial state effects are mainly influenced by the charge distribution on the atom prior to photoemission, which can provide information on the type of bonding present. For example, in the case of carbon based substances, the magnitude of the chemical shift of the carbon peak (C 1s) will indicate the type of hybridization present in the carbon bonds. Final state effects occurs after photoemission and includes effects such as core-hole screening, relaxation of electron orbitals and the polarization of surrounding ions. These are often dominant in influencing the magnitude of the chemical shift.

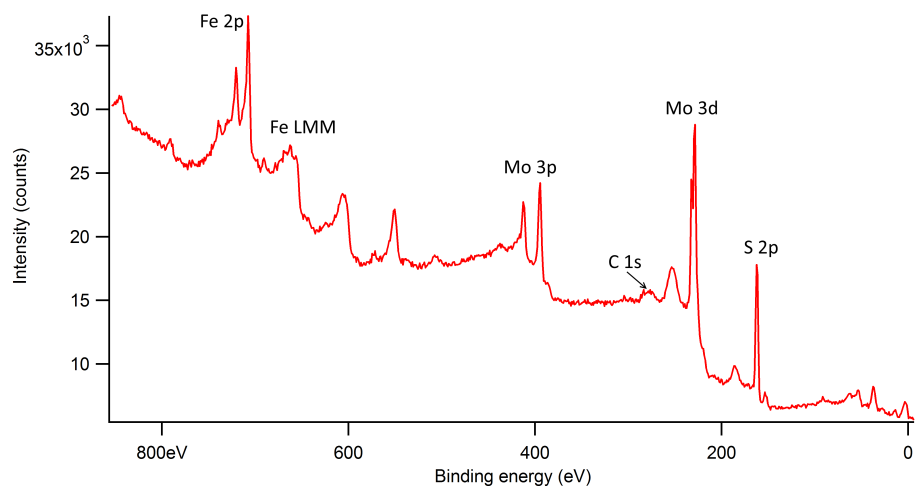


Figure 2.8: XPS wide-scan taken with  $\text{MgK}\alpha$  radiation (1253.6eV) of  $\text{Fe}/\text{MoS}_2$ . The main photoemission lines are marked according to their origin.

## Features of an XPS spectrum

Figure 2.8 shows an example XPS spectrum taken on  $\text{MoS}_2$  with a thin iron overlayer. It is displayed as a plot of electron binding energy (referenced to the Fermi level for conductive solids) versus the number of electrons registered by the detector. The spectrum shows a series of peaks superimposed on a continuous background. In general the well defined peaks are those coming from electrons which have left the sample without losing energy, while electrons that have been inelastically scattered make up the background. It should be noted that while the background is usually subtracted from the spectrum during analysis it is not without worth. Particularly, the shape of the background can reveal a lot about the type of loss processes the electrons can go through on their way out of the sample.

The main features of the spectrum[73] are briefly described in the following:

### Photoelectron Lines

These are the most intense lines in the spectrum and the primary point of interest for XPS. They are the lines caused by electrons photoemitted from the sample which have escaped without losing any energy. Peaks due to photoemission of electrons from core levels are named according to the core

electronic state they came from (i.e. 1s2s2p and so forth...). Analyzing the location and area of these peaks provides most of the information obtained by XPS. In the case of the spectrum in Figure 2.8, they reveal the presence of molybdenum, sulfur, iron and carbon in the sample. At a first glance it also indicates that the sample contains a relatively larger fraction of molybdenum than carbon. However, when comparing the areas of peaks in XPS in any way it is important to take into account the photoionization cross-section. The photoionization cross-section, usually denoted  $\sigma$ , is the probability of the emission of an electron due to the effect of the incoming radiation. It depends on several factors such as the element being considered, the orbital from which the electron is emitted and the energy of the exciting radiation. Conveniently, however, it is relatively unaffected by the chemical environment the atom is in, making it possible to use the calculated atomic cross-sections. As an example of this consider the peaks labelled Mo 3d and S 2s in Figure 2.8. Taking the cross-section into account reveals that, although the peak to background height of the Mo 3d peak is higher than that of the S 2p, the sample contains roughly twice as much sulfur as molybdenum.

Another important feature of several core level peaks can be seen in Figure 2.9. It shows a better resolved spectrum of the Mo 3d core level. Importantly, the 3d peak is split into two peaks labeled  $3d_{3/2}$  and  $3d_{5/2}$ . This splitting is caused by the spin-orbit interaction (j-j coupling), and the subscript is given by the quantum number  $j = l + s$ , where  $l$  is the angular momentum quantum number and  $s$  is the spin quantum number. Because  $s$  can take on the values  $\pm\frac{1}{2}$ , all orbital levels (except the s levels where  $l = 0$ ) give rise to a spin-orbit split doublet. The spin-orbit splitting is an initial state effect and nearly entirely atomic in nature, meaning the size of the splitting can be used as an additional characteristic quantity. Furthermore, the peaks will have a specific area ratio given by the degeneracy of each of the spin states. In the case of the Mo 3d doublet this ratio is 2:3.

Other factors that might provide useful insights are the shape and the symmetry of the peak. The shape can for example indicate whether a peak has several components, each from an atom in a slightly different environment. And while most peaks are symmetric, metallic core levels give rise to asymmetric peaks due to coupling with conduction electrons.

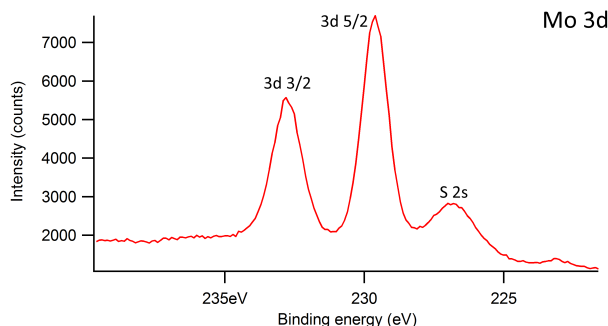


Figure 2.9: XPS spectrum taken with  $\text{AlK}\alpha$  radiation (1486.6eV) of the Mo 3d core level. Visible are the two spin-orbit split components of the Mo 3d peak and the S 2s peak.

### Auger Lines

When a core electron is emitted as a result of a photoemission event the atom it leaves behind is left in an excited state. It can subsequently relax by filling the vacancy with an electron from a higher energy level, losing energy in the process. This energy can be emitted in the form of a photon or it can instead be transferred to another electron which is ejected from the atom (or some combination of the two). The latter is known as the Auger effect and the ejected electron is called an Auger electron. During an XPS measurement a certain number of these electrons will be emitted and recorded in the spectrum. The resulting peaks are classified according to the transition that produced them. For example, the peak labeled Fe LMM in Figure 2.8 is due to an Auger transition in an iron atom in which a core hole in the K shell (first letter) is filled by an electron from the M shell (second letter), transferring the energy to an electron in the M shell (third letter) which is emitted. The energy of these peaks are characteristic of the binding energies of the core electrons and the Auger effect is the basis of an alternative experimental technique known as Auger electron spectroscopy (AES). An important point about the energy of the Auger peaks in the context of XPS is that, unlike the photoelectrons, the kinetic energy of the Auger electrons does not depend on the energy of the exciting radiation. This means that should an Auger peak fall on top of the photoemission line of a core level of interest, it is possible to move the photoemission line relative to the Auger peak by changing the energy of the ionizing radiation (when

kinetic energy is chosen for the abscissa of the spectrum).

### **Energy Loss Lines**

There can exist, in certain materials, an enhanced probability that the photoelectron lose a specific amount of energy through some particular interaction. In such cases a series of smaller peaks will appear to the left of the major photoemission peaks. These peaks are due to electrons that have lost energy an integer amount of times to the interaction in question. Plasmon loss peaks are the most common example of energy loss peaks in XPS. They arise when the photoelectron loses some energy to excite a plasmon at some point in the photoemission process.

### **Satellites and Non-monochromatic Effects**

The photon beam used in XPS experiments is often not entirely monochromatic. Instead the emission spectrum contains, in addition to the characteristic x-ray, some minor x-ray components at higher photon energies. These x-rays will also excite photoelectrons, albeit at a much lower rate than the primary x-ray. The peaks formed by photoelectrons generated in this manner are called x-ray satellites and generally appear as images of intense peaks. In addition to these, a different sort of satellite referred to as "ghost" peaks might appear in the spectrum. These are peaks caused by x-rays originating from an element other than the x-ray source anode material, typically from impurities in the source material. Again these peaks appear as images of the most intense peaks at an energy interval equal to the difference in photon energy between the main x-ray line and the ghost line.

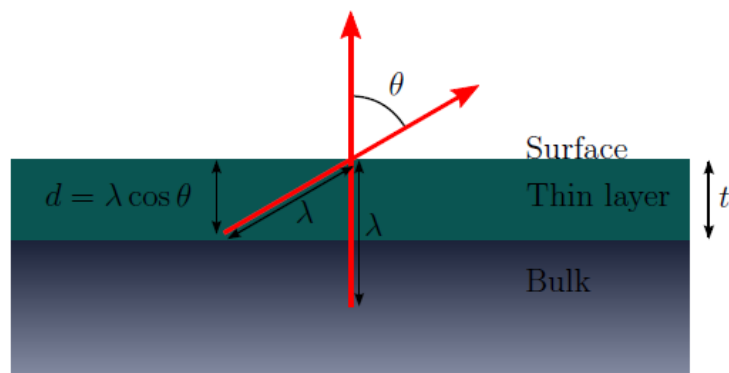


Figure 2.10: Illustration of the basic principle of ARXPS. It shows electrons (red arrows) escaping a sample consisting of a thin overlayer of thickness  $t$  on a bulk material. By changing the angle  $\theta$  between the surface normal and the analysis direction, the probing depth  $d$  is reduced by an amount equal to the cosine of that angle. The effective attenuation length  $\lambda$  is used as an approximation of the electron escape depth.

### 2.3.2 ARXPS

As mentioned before, the probing depth of an XPS experiment is determined by the kinetic energy of the excited photoelectrons, which in turn is governed by the energy of the x-rays employed. Meaning that it is possible to detect electrons coming from different depths in the sample by varying the photon energy. This, however, is not always practicable. Excluding synchrotron light sources, most lab based XPS setups only have access to a couple of different x-ray energies, providing at best a modest depth profiling capability. Luckily, the same effect can be achieved in a simpler way. By changing the angle between the surface normal and the analysis direction as seen in Figure 2.10, the probing depth can be reduced. This is the basic principle of angle-resolved XPS (ARXPS).

ARXPS data is usually acquired in one of two ways depending on the experimental setup. When using a one dimensional detector (the so called channeltron detector being the most common example) the lens system is set up to provide an angular resolution of about  $1^\circ$  to  $5^\circ$ . Then the sample is tilted relative to the lens axis in steps, with a spectrum being taken at each step. The other method involves using a two dimensional detector. With the proper lens setup such detectors are capable of dispersing photoelectron

energy along one of its axes and the angular distribution along the other. This method can produce a spectrum with an angular range of  $60^\circ$  with a resolution of about  $1^\circ$ . Different considerations must be made depending on which method is used. When tilting the sample one must take care to align the analysis position at each angle, as it will change if it is some distance away from the tilt axis. Secondly, one must be aware that the analysis area changes with the angle, the magnitude of the change depending on the lens settings used. Using a two dimensional detector these issues are sidestepped as the sample is not moved. It is, however, necessary to correct for the asymmetry factor which affects the angular dependence of the photoemission from a given orbital. This is not necessary when tilting the sample because the angle between the x-ray source and the emitted electrons is kept constant.

Regardless of the method used ARXPS is a powerful technique which enables depth profiling both of elemental concentrations and of chemical states. It is particularly useful for studies of thin films. The data it provides can be used, for example, to determine the thickness of an overlayer through the following relation:

$$\frac{I_A}{I_B} = \frac{I_A^\infty [1 - \exp(-t/\lambda_{A,A} \cos \theta)]}{I_B^\infty \exp(-t/\lambda_{B,A} \cos \theta)}. \quad (2.19)$$

The situation this equation applies to is similar to that depicted in Figure 2.10, i.e. an overlayer of material  $A$  of thickness  $t$  on a substrate of material  $B$ .  $I_A$ , and  $I_B$  are the intensities of the signal from the material given by the subscript.  $I_A^\infty$  and  $I_B^\infty$  are the equivalent intensities which would be obtained from infinitely thick layers of the materials. Finally,  $\lambda_{B,A}$  is the effective attenuation length (EAL) of an electron emitted in material  $B$  in material  $A$ , and analogously for  $\lambda_{A,A}$ . The effective attenuation length as a concept is similar to the IMFP[74], except it does not neglect elastic scattering of the electrons on their way out of the sample. A quick derivation of this result along with the necessary assumptions can be found in Appendix A. In addition to the film thickness ARXPS can provide some rudimentary information about the growth mode of the thin film.

For samples containing multiple layers the technique can give the thicknesses of the individual layers, the ordering of the layers, and even depth profiles within the layers.

ARXPS has a number of advantages over other depth profiling techniques such as for example sputtering (sputtering involves eroding away top layers of the sample by bombarding it with ions). First and foremost is the fact

that it can provide chemical state information in addition to elemental information. Second, it is non-destructive and can be applied to materials, such as polymers, which would be destroyed using other techniques. Finally it can be used on films that are too thin for other depth profiling techniques.

### 2.3.3 UPS

Ultraviolet photoelectron spectroscopy (UPS) as a technique is nearly identical to XPS with the exception that it uses ultraviolet photons (in the energy range  $\sim 6$ -50eV) instead of x-rays as an ionization source. This difference, however, has a profound impact on what the technique is used to study. UPS is perhaps the most powerful technique to study the electronic structure of valence states in atoms, molecules and solids. Valence states are the energy levels found at about 10-20eV below the vacuum level and are those states which are primarily involved in chemistry. As such they play a uniquely important role in determining many of the electrical and chemical properties of solids. UPS can be used for a host of different applications such as, for example, measuring the work function of materials.

It should be noted at this point that there is no well defined energy boundary which separates valence states from core levels. While valence states can extend to around 10-15eV in binding energy, there are core levels which are as shallow as a couple of eV. Furthermore, it is possible to measure valence bands using XPS, however, the spectra acquired will likely not match those taken using UPS. There are two main causes for this difference. In both cases the valence band spectra acquired reflect the density of (occupied) valence states to some degree. However, because the photoionization cross section depends on the photon energy, the density of states will be modified differently in both techniques. The second difference is related to the sudden approximation. In XPS the photoelectrons are excited with high enough kinetic energies ( $>100$ eV) that the density of states is relatively unmodified by final state effects. In UPS, however, the kinetic energy of the photoelectrons is comparable to the energy of the valence electrons, meaning that the density of states will be modified by all those interactions neglected by the sudden approximation. Because of these differences certain features of the valence band will be enhanced in UPS while others will be enhanced in XPS. There are a couple of significant advantages to using UPS for valence band spectroscopy however. First, the photoionization cross-section is generally much higher for ultraviolet radiation in the valence region. This means that

the count rate of detected electrons will be much higher for a beam of UV photons than for a beam of x-rays of similar flux. Second, UPS is clearly more useful if it is desired to study any of the interactions which modify the density of states mentioned previously. Finally, UPS offers both superior energy and momentum resolution to XPS. The reason for this is again two-fold. One, the natural line width of commonly used UV radiation is much smaller than that of commonly used x-rays. Two, the resolving power of most electron analyzers depends on the kinetic energy of the photoelectrons: in general the higher the energy, the lower the resolution.

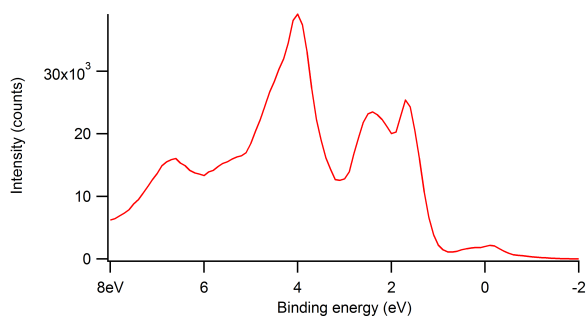


Figure 2.11: Example UPS spectrum on MoS<sub>2</sub> taken with HeI (21.2eV) radiation.

Figure 2.11 shows an example of a UPS spectrum taken on  $\text{MoS}_2$ . It shows a spectrum with peaks, corresponding to valence bands, along with the same background of secondary electrons found in XPS. The small peak at the Fermi level ( $E_B = 0$ ) is believed to be due to a secondary photon line from the UV source.

### 2.3.4 ARPES

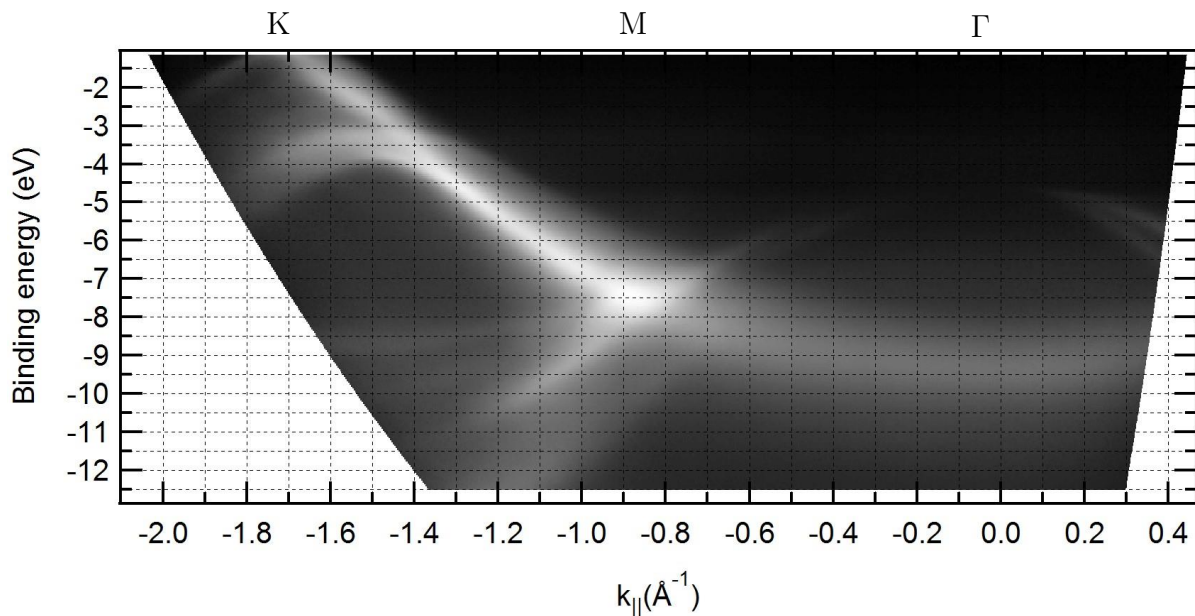


Figure 2.12: Example ARPES spectrum of graphite taken with a 2D detector. It shows dispersing bands in white on a black background. Visible below the  $\Gamma$  point are the two branches of the  $\sigma$ -bands. Running underneath the sigma bands and curving up in the  $\Gamma - M$  direction is the  $\pi$ -band.

Angle-resolved photoemission spectroscopy (ARPES)<sup>1</sup> or alternatively angle-resolved UPS (ARUPS) is well-established as an important tool for understanding the properties of solids. It is, in certain regards, an extension of UPS in much the same way ARXPS is an extension of XPS, at least in execution if not in purpose. As was the case for ARXPS, ARPES spectra are

<sup>1</sup>The interested reader is directed to a comprehensive review of ARPES written by Damascelli[63].

acquired in one of two ways depending on the type of detector available, with nearly all newer ARPES systems sporting 2D detectors for their increased resolution and added convenience. Unlike ARXPS, however, ARPES is not primarily a depth profiling technique. Rather the purpose of this technique is to map the momentum dependence of the electronic binding energy in the solid  $E_B(\mathbf{k})$ , the so called momentum dependent electronic band structure. This is achievable because, as mentioned earlier, the momentum of the electrons in the solid is related to the angle at which the photoelectrons are emitted (e.g. Equation 2.6). Another powerful aspect of ARPES is that, in addition to providing a direct method of mapping the single-electron band structure of materials, it sheds light on the strength and nature of many-body correlations present within the sample. These many-body interactions may profoundly affect the single-electron excitation spectrum and consequently the physical properties of the solid.

A major reason why the same thing cannot easily be done with ARXPS is traceable to the photon momentum. Unlike the low energy ultraviolet photons used in UPS, the momentum of an x-ray photon is often significant compared to the momentum of electrons in a solid. Meaning that the transitions they induce are not necessarily direct (a direct transition is one for which  $\mathbf{k}_i = \mathbf{k}_f$  or in the extended-zone scheme  $\mathbf{k}_f - \mathbf{k}_i = \mathbf{G}$ , where  $\mathbf{G}$  is a reciprocal lattice vector). This in turn means that knowing the momentum of the photoelectron in vacuum is no longer enough to uniquely determine the momentum of the electron in the solid. Additionally, from Equation 2.6 it can be seen that the high kinetic energy of photoelectrons excited by x-rays means that any given change in angle corresponds to a much larger distance in reciprocal space. Generally, the angle at the boundary of the first Brillouin zone will be only about  $1^\circ$ - $2^\circ$ . This, in combination with the worse angular resolution available in ARXPS, means that valence state spectra taken in XPS will often be angle integrated rather than angle resolved.

A spectrum taken in UPS such as the one in Figure 2.11, which shows an energy scan taken at a constant angle (momentum), is called an energy distribution curve or EDC for short. Figure 2.12 shows an example ARPES spectrum (technically a composite of several spectra) obtained using a 2D detector. An EDC corresponds to a vertical cut through such a spectrum. In an analogous fashion a horizontal cut, i.e. a momentum scan taken at a constant energy, is called a momentum distribution curve (MDC).

Determining the band structure from measured EDCs is not always a trivial undertaking, particularly with regards to the perpendicular compo-

ment of the electron momentum,  $\mathbf{k}_\perp$ , as described in the earlier section. For 2D and quasi-2D systems such as e.g. graphene or layered TMDCs, however, the dispersion in  $\mathbf{k}_\perp$  is less relevant and the band structure is well described in terms of  $E_B(\mathbf{k}_\parallel)$ . When this is not the case the situation is more complex, but in general the assumption of nearly free electron final states used to derive Equation 2.7 is a rather accurate approximation[57].

Finally, it should be noted that ARPES is also capable of mapping 3D band structures, though this requires a variable photon energy source (e.g. a synchrotron) to map the dispersion in  $\mathbf{k}_\perp$ .

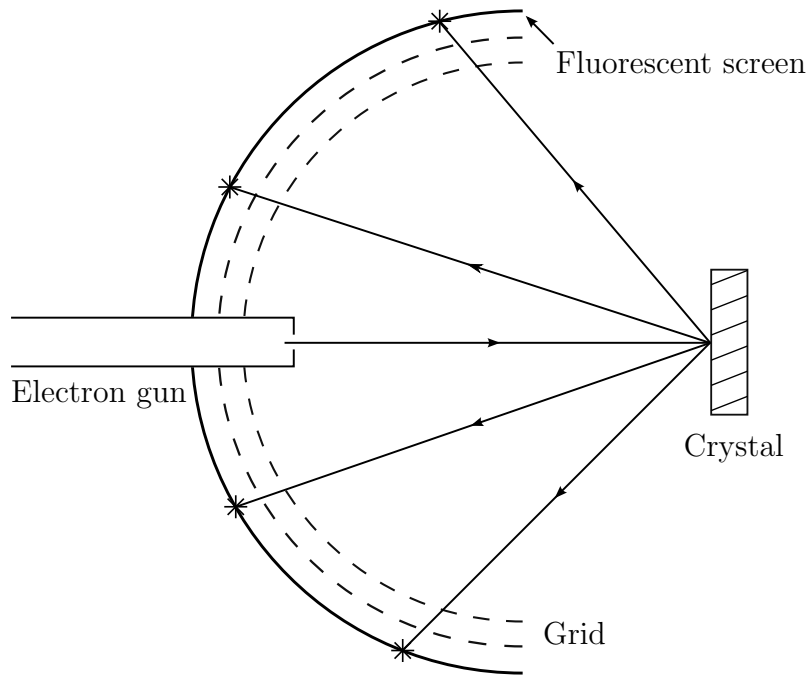


Figure 2.13: Schematic of a LEED experiment. Electrons emitted from an electron gun are backscattered from a crystal through a suppressor grid onto a fluorescent screen. The suppressor grid removes inelastically scattered electrons.

## 2.4 Low Energy Electron Diffraction (LEED)

Low Energy Electron Diffraction, or LEED, is an experimental technique used to study the surface structure of crystalline materials [75]. Figure 2.13 shows a basic LEED experiment. An electron gun emits a well collimated and monoenergetic electron beam towards a sample. Some of the electrons are diffracted from the surface of the crystal and travel back towards the grids. In the simplest case there are two grids, the first of which is grounded. The second grid is biased relative to the first so that only electrons having lost a small amount of kinetic energy may pass. This effectively ensures that only elastically scattered electrons are imaged. Finally, the screen is biased to a large accelerating voltage in order to give the electrons enough energy to excite the phosphor in the screen.

To understand the patterns formed from LEED experiments consider a

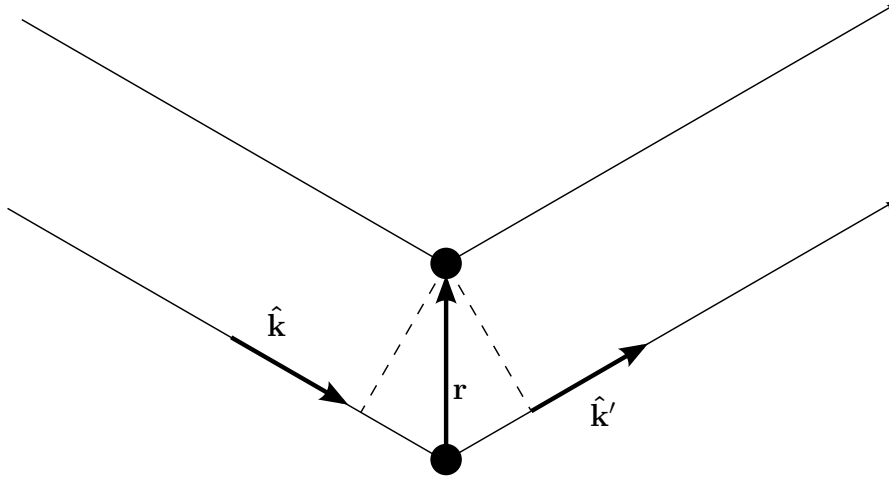


Figure 2.14: A beam of collimated electrons incident, along a direction  $\hat{\mathbf{k}}$ , on two atoms separated by a lattice vector  $\mathbf{r}$ . The electrons are scattered in direction  $\hat{\mathbf{k}}'$ .

collimated, monoenergetic beam of non-relativistic electrons incident on a well ordered surface as seen in Figure 2.14. Let the electron beam be represented by a plane wave with a de Broglie wavelength given by

$$\lambda = \frac{h}{p} = \frac{h}{\sqrt{2mE_{kin}}} \quad (2.20)$$

where  $p$ ,  $m$  and  $E_k$  are the momentum, the mass and the kinetic energy of the electron respectively. Note that the energies typically used in LEED, 20-200eV, give wavelengths from 2.7-0.87Å, on the scale of atomic dimensions. The wave is incident on the surface along a direction  $\hat{\mathbf{k}}$  with a wave vector  $\mathbf{k} = \frac{2\pi}{\lambda}\hat{\mathbf{k}}$  and is elastically scattered to a direction  $\hat{\mathbf{k}}'$  with a wave vector  $\mathbf{k}' = \frac{2\pi}{\lambda}\hat{\mathbf{k}}'$ . The condition for constructive interference is that the path difference between two beams shown in Figure 2.14 is equal to an integer,  $n$ , number of wavelengths. That is

$$(\hat{\mathbf{k}}' - \hat{\mathbf{k}}) \cdot \mathbf{r} = n\lambda, \quad (2.21)$$

where  $\mathbf{r}$  is a lattice vector. Multiplying this result by  $\frac{2\pi}{\lambda}$  gives

$$(\mathbf{k}' - \mathbf{k}) \cdot \mathbf{r} = 2\pi n \quad (2.22)$$

or equivalently

$$e^{i(\mathbf{k}' - \mathbf{k}) \cdot \mathbf{r}} = 1. \quad (2.23)$$

Which is precisely the condition that the scattering vector  $(\mathbf{k}' - \mathbf{k})$  is a reciprocal lattice vector,  $\mathbf{G}$ . The diffraction condition can thus be written as

$$\mathbf{k}' - \mathbf{k} = \mathbf{G}. \quad (2.24)$$

This condition is illustrated well by the construction of the Ewald sphere seen in Figure 2.15. The reciprocal lattice is represented by a periodic arrangement of rods because while there exists a well defined periodicity parallel to the surface, the same is not true perpendicular to the surface. This is due to the strong electron-electron interactions which give the low energy electrons a mean free path in the crystal of only a few angstroms. As such, only the outermost atomic layers contribute to the diffraction. The lack of a well defined periodicity in the direction perpendicular to the surface means that the reciprocal lattice vectors in this direction can take nearly any value. Every reciprocal lattice rod that intersects this sphere gives rise to a diffraction spot.

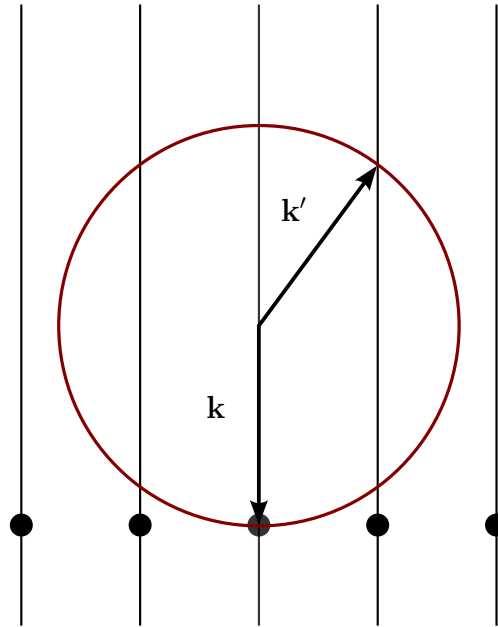


Figure 2.15: Ewald's sphere construction for the case of normal incidence diffraction from a 2D lattice. Every reciprocal lattice rod that intersects the sphere gives rise to a diffraction spot.

The low penetration depth of the electron beam has a number of consequences relevant to LEED experiments. First, this is what makes LEED a surface sensitive technique. Being surface sensitive, obtaining good quality results is highly dependent on having a clean sample surface. Second, it means the experiment must be performed in vacuum. Not only to avoid contamination of the sample, but also to limit the scattering of electrons by gas particles between the sample and the detector. Finally, it means that the chance of multiple scattering is high. If it is desired to extract quantitative data from a LEED experiment, e.g. for accurate structure determination, dynamic scattering theories are needed[75, 76]. However, LEED is still a highly valuable tool used qualitatively. The diffraction pattern gives much information on the symmetry of the surface structure.

## 2.5 Ultra High Vacuum

Ultra high vacuum (UHV) refers to the vacuum regime with pressures in the  $10^{-9}$  mbar range and below. Such high vacuums are required for a number of experimental techniques including PES and LEED. Achieving UHV is a process that involves different stages of pumping as well as heating the entire system to temperatures above  $100^{\circ}\text{C}$  in order to remove gases (primarily water) adsorbed onto the walls of the UHV vessel. The exigencies of UHV environments also places a number of restrictions on which materials can be used in the making of UHV systems. Any equipment going inside the vacuum system, along with the vacuum chamber itself, must be made from materials with low vapor pressures.

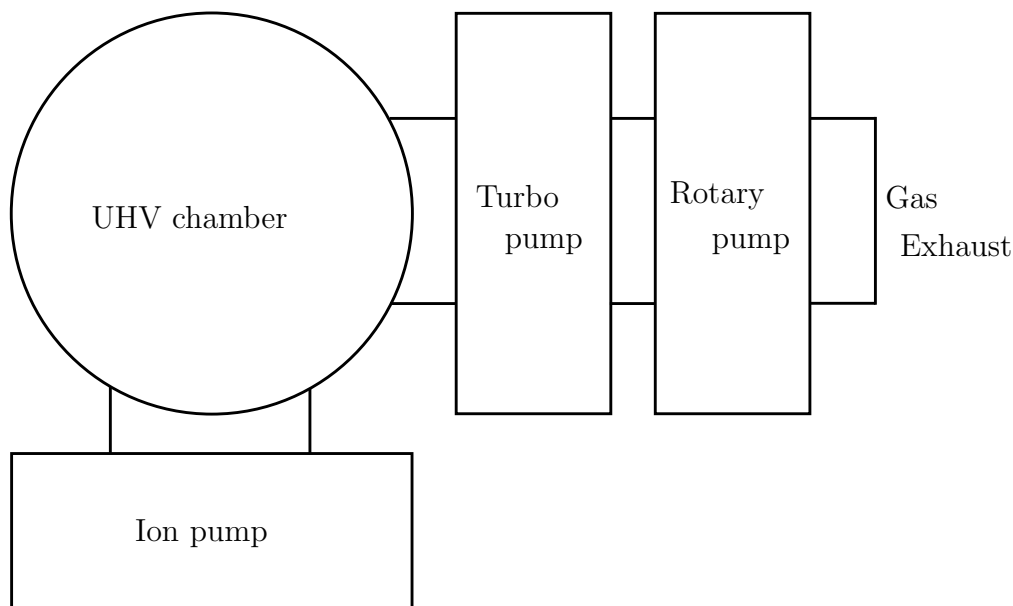


Figure 2.16: A schematic of a typical UHV pump setup. Adapted from Hofmann[59].

Figure 2.16 shows a typical pump setup used to achieve and maintain a UHV environment. The different pumping stages will be briefly discussed in the following.

## Positive Displacement Pumps

The first stage of the pumping process involves what are known as roughing pumps or positive displacement pumps. These are pumps which work in the viscous flow regime, i.e. when the particles in the fluid interact more with each other than the walls of the container, and are capable of reaching pressures of around  $10^{-3}$  mbar. Though there exists a multitude of designs for such pumps they all more or less work according to the same principle. The volume of a container open to the system is expanded, creating an artificial vacuum. This volume is filled with gas from the system, sealed off and then exhausted to outside the system. Figure 2.17 shows a rotary vane pump, a commonly used positive displacement pump.

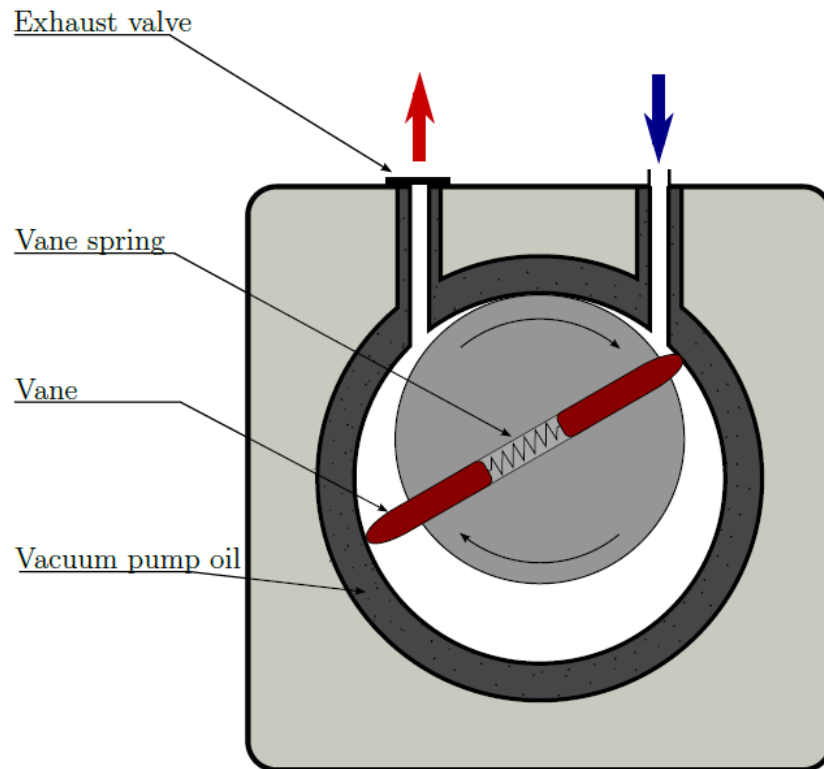


Figure 2.17: Illustration of a rotary vane pump, a type of positive displacement pump. As the inner disk rotates, the volume at the inlet (blue arrow) is expanded, closed off, and subsequently evacuated from the system through the exhaust valve (red arrow).

## Momentum Transfer Pumps

As the pressure in the system decreases the mean free path of gas molecules within the system quickly becomes very long. The molecules are at this stage much more likely to collide with the walls of the chamber than with each other, in other words the gas is in the molecular flow regime. Clearly the positive displacement pumps, which rely on viscous gas flow, are ineffective in such low pressures. This is where the second stage of pumping kicks in. These pumps, called momentum transfer pumps, work by imparting momentum to any particle which enters the pumps in such a way that the particle is more likely to be pushed through to the exhaust of the pump, than it is to escape back into the system. While these pumps can achieve pressures as low as mid  $10^{-11}$ mbar, they do not work in the viscous flow regime, meaning that they must be backed by roughing pumps. The most common type of momentum transfer pump used to reach the UHV regime is the turbomolecular pump depicted in Figure 2.18.

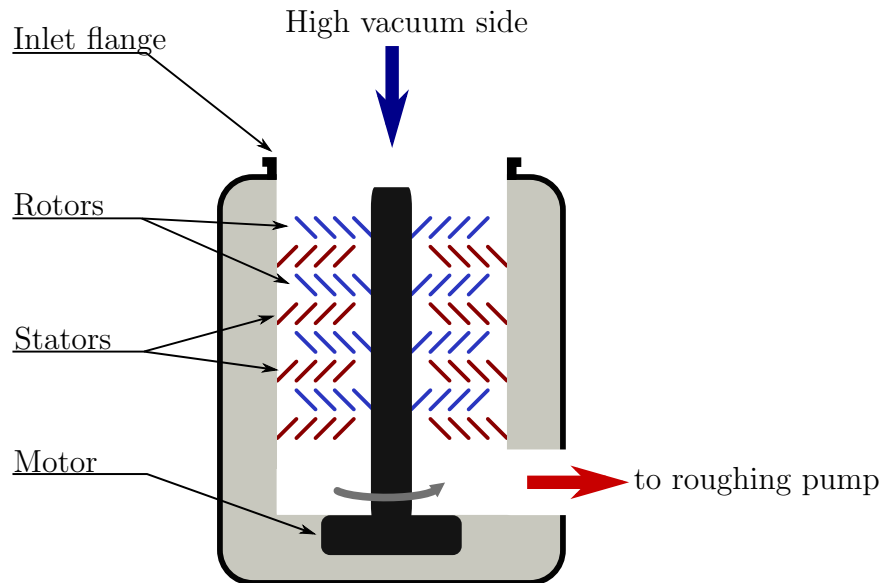


Figure 2.18: Illustration of a turbomolecular pump. In turbomolecular pumps a stack of turbine blades rotates at about 80000 rpm relative to a second set of stationary blades called stators. The blades impart momentum to the molecules, which are moved preferentially from the inlet to the exhaust because of the relative motion of the blades.

## Entrapment Pumps

A third set of pumps, known as entrapment pumps, are often used to maintain the UHV conditions. Contrary to the other pumps discussed, these pumps do not exhaust gas particles out of the system entirely. Rather, they entrap them within themselves. The two most common kinds of entrapment pumps for UHV systems are titanium sublimation pumps and ion pumps. Titanium sublimation pumps consist more or less of a titanium filament, which sublimates titanium onto the chamber walls. Because titanium is very reactive any rest gas that collides with the chamber walls will tend to react with the titanium and form solid compounds, reducing the pressure in the chamber. These pumps are particularly useful for removing light gas molecule, e.g. hydrogen, that the momentum transfer pumps are less efficient at removing. Figure 2.19 shows an illustration of an ion pump.

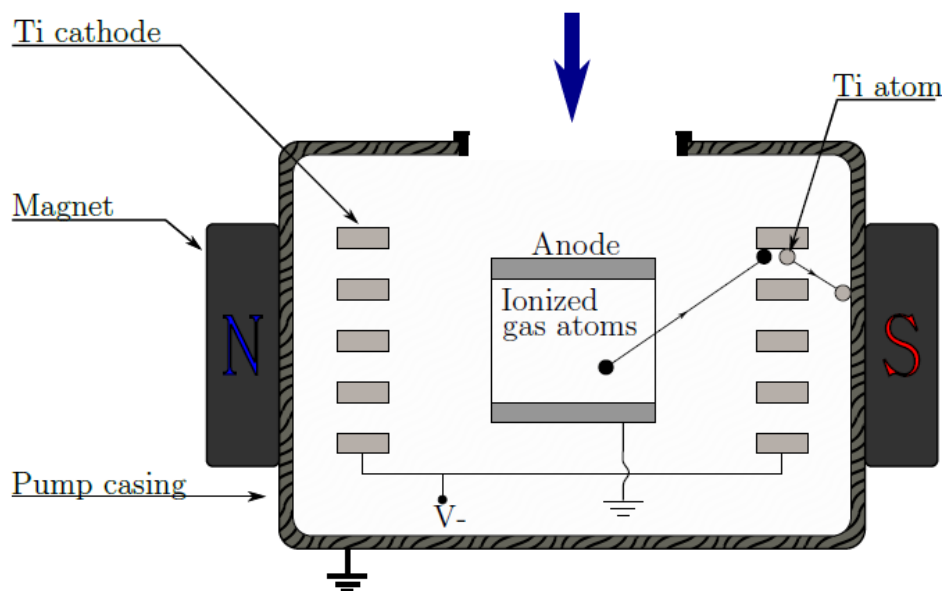


Figure 2.19: Illustration of an ion pump. Ion pumps use strong electrical fields to ionize rest gas and propel the resulting ions into a solid substrate where they are captured. A magnetic field applied to the pump causes charged particles to travel in spiral trajectories, increasing the ionization probability of gas atoms. Many ion pumps use titanium cathodes which can release titanium when struck by an ion. This will increase the amount of particles that get stuck to the pump walls because titanium is highly reactive.

# Chapter 3

## Procedure

The experiments in this thesis were performed in two main stages at two separate locations. Most of the preparatory work, i.e. sample characterization and growth rate determination, was performed at the home lab in Trondheim while the high resolution ARPES measurements were performed at Phil King's lab at St. Andrews university. This chapter will give a brief overview of the experimental setups at each of the two labs, describing a couple of key pieces of equipment in a bit more detail. Subsequently the sample preparation procedure will be explained, before a rough description of the treatment of the experimental data is given to conclude the chapter.

### 3.1 Experimental Setup

Figure 3.1 and Figure 3.2 show schematic representations of the lab setup in the Trondheim lab and the St. Andrews lab respectively. The two setups are both primarily intended for surface analysis by PES and consequently share a large number of features. Both systems consist of a series of compartmentalized chambers kept under UHV conditions, with each chamber serving a different purpose. Gate valves connect the chambers allowing the transfer of samples between them, yet at the same time giving the possibility of shutting the chambers off to one another. When the gate valves are closed any pressure change in one chamber will not affect the pressure in any of the others.

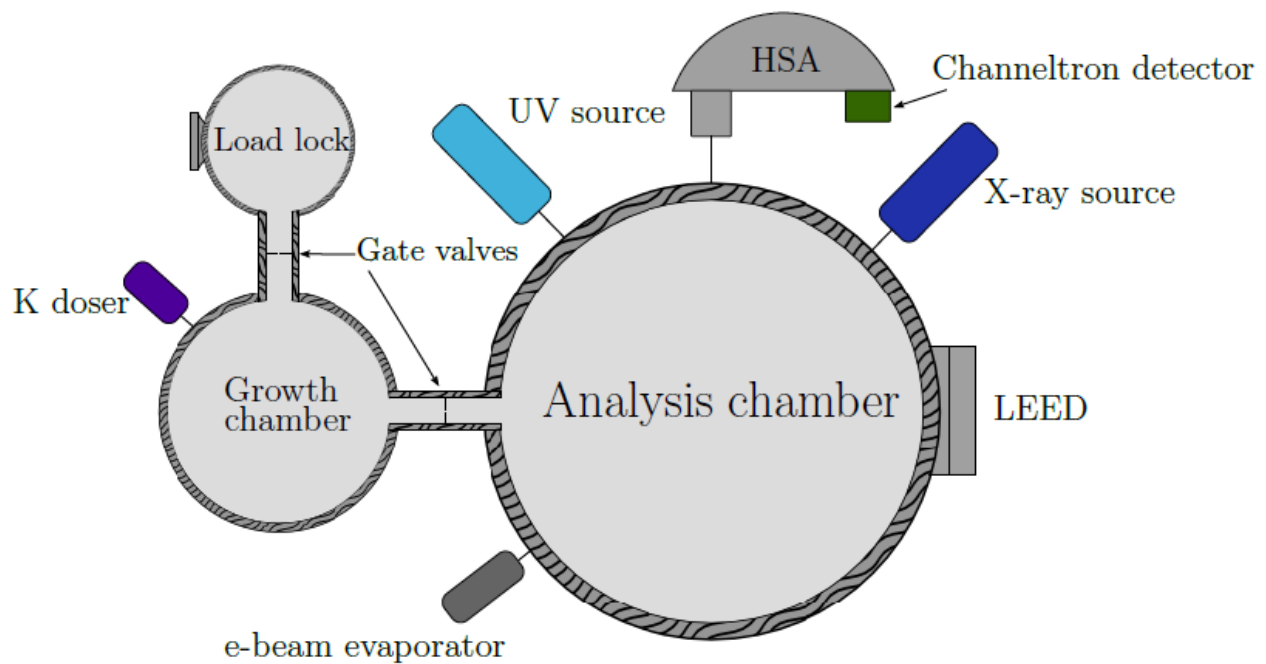


Figure 3.1: Schematic representation of the experimental setup at the home lab in Trondheim. The setup consists of three main chambers: a load lock, a growth chamber and an analysis chamber equipped to perform a number of surface techniques.

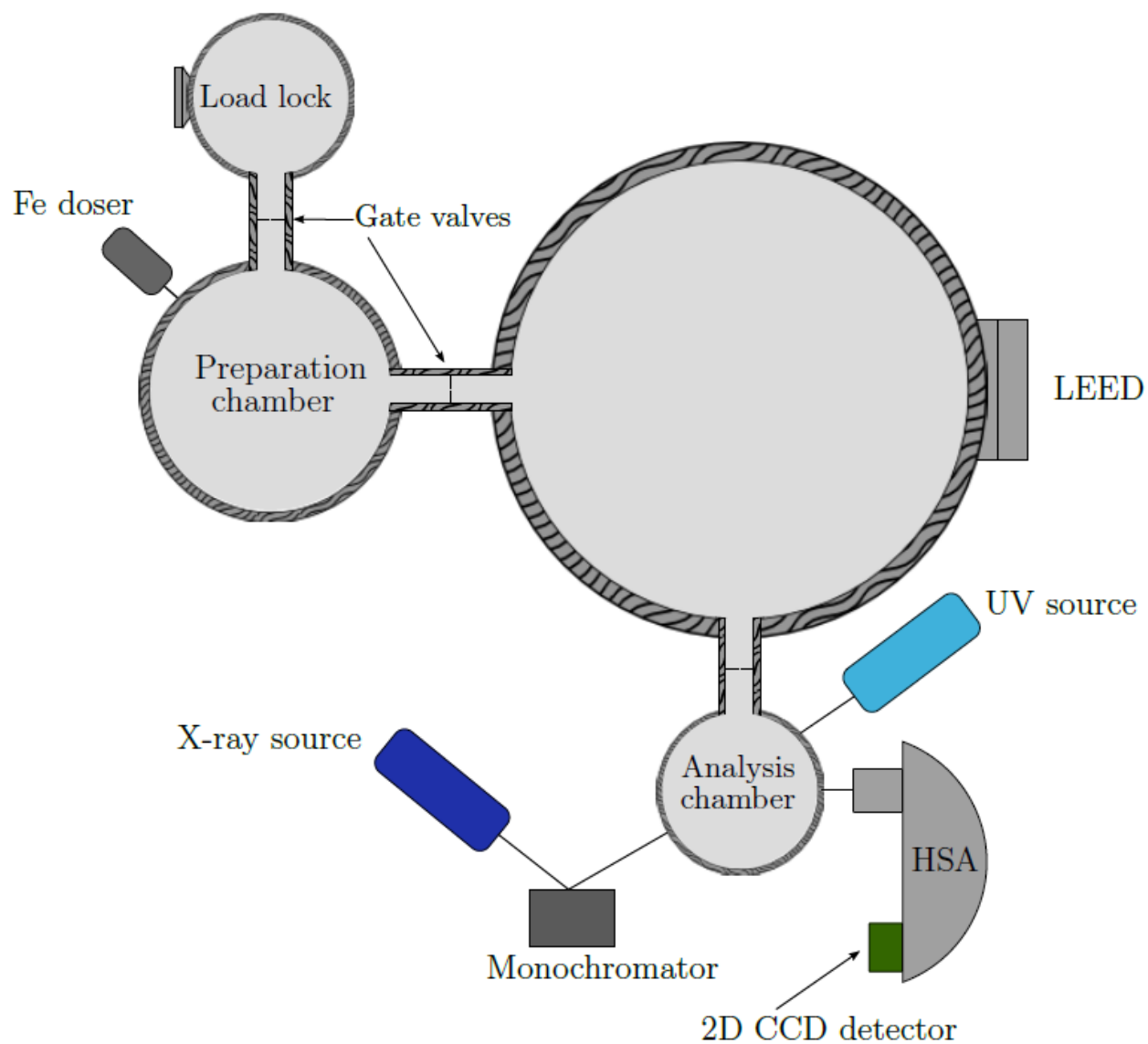


Figure 3.2: Schematic representation of the experimental setup at Phil King's lab in St. Andrews. It consists of four main chambers: a load lock, a preparation chamber, and two analysis chambers equipped for different techniques.

The load locks are the entry points of the systems. They permit moving samples in and out of the system without venting the main chambers, drastically speeding up the procedure. Rather than having to pump down the entire setup, which could take days as the system would have to be baked, only the small volume of the load lock itself must be brought back to vacuum. The latter can be done in minutes to an hour depending on the size of the load lock.

Both of the systems also have a growth or a preparation chamber. These are typically the chambers where any additional sample preparation requiring vacuum, e.g. dosing the sample with other materials, is done. This process is done outside of the analysis chambers whenever possible in order not to introduce rogue elements to these. Particularly important when using materials which are hard to remove from the vacuum system, such as a wide range of organic materials. The growth chamber in Trondheim was fitted with a potassium alkali metal dispenser (AMD) from SAES getters. AMDs are small sources capable of producing ultrapure vapors of alkali metals at reproducible rates. The preparation chamber in St. Andrews was equipped with an improvised iron doser consisting quite simply of a lump of pure iron trapped in a coiled filament. When current is passed through the filament the iron heats up and starts evaporating. For practical reasons the iron dosing in Trondheim was done in the Analysis chamber using an e-beam evaporator, which will be explained shortly.

The analysis chambers are equipped with a similar range of equipment with a couple of notable differences. Both systems are equipped with an x-ray source, a UV source, LEED optics as well as a hemispherical analyzer. The setup in St. Andrews additionally has a monochromator for its x-ray source and uses a different UV source which can also be monochromated. However, the principal difference between the two systems lies in the detectors. While the setup in Trondheim sports a 1D channeltron detector, consisting of nine electron multipliers in a line, the St. Andrews setup uses a 2D CCD detector. Each of these detector types has its own advantages and disadvantages. The channeltron detector has excellent counting efficiency, registering nearly all electrons that hit it, and is suitable even for very high count rates. This means that the setup in Trondheim is well suited for chemical analysis using XPS and non-angle resolved UPS. The 2D detector, as mentioned in an earlier chapter, has superior angle resolution and is in general much more convenient for angle resolved studies. As a consequence the setup in St. Andrews is better suited for angle resolved studies, ARPES in particular. Another reason

for this is that this setup has a 6-axis manipulator (three linear motions and three rotational), compared to the 4-axis manipulator (three linear and one rotational) in Trondheim. This makes it so that the sample can be aligned in directions of high symmetry. Finally, the St. Andrews system has a liquid helium cooling setup, compared to a liquid nitrogen setup in Trondheim, capable of maintaining the sample temperature at around 5K. This gives it an advantage for studying systems with transition temperatures lower than the temperature reachable with liquid nitrogen as well as a minor resolution advantage (though the thermal broadening is generally not the limiting factor of the resolution).

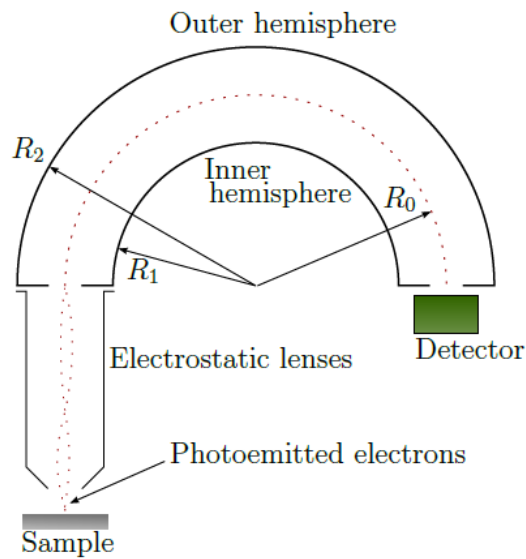


Figure 3.3: Illustration of a hemispherical sector analyzer.  $R_1$  and  $R_2$  are the radii of the inner and outer hemisphere respectively. A negative potential is applied to both hemispheres.  $R_0$  is the mean radius.

## Hemispherical Analyzer

The hemispherical sector analyzer (HSA), sometimes called the concentric hemispherical analyzer, is the most common electron energy analyzer design used for photoelectron spectroscopy. An illustration of an HSA is shown in Figure 3.3. It consists of two concentric stainless steel hemispheres: an inner hemisphere of radius  $R_1$  and an outer hemisphere of radius  $R_2$ . A negative potential is applied to each of the hemispheres, with the potential on the outer one being higher than that on the inner one. Any electron travelling through the analyzer will be deflected by an amount determined by its kinetic energy. When the potentials on the hemispheres are kept constant only electrons having a specific kinetic energy, called the pass energy  $E_p$ , or within a certain range of this energy, will reach the detector. Electrons having a higher or lower kinetic energy will be collected by one of the hemispheres. The analyzer can scan over energies in one of two principal ways. Either by varying the potential applied to the hemispheres and thus changing the pass energy or else by varying the lens settings. In the latter mode, known as fixed analyzer transmission (FAT), the pass energy of the analyzer is kept constant and instead the lens system is used to accelerate or retard a given kinetic energy channel to the pass energy. The main advantage to this for PES is that in this mode the energy resolution  $\Delta E$ , given by

$$\Delta E = E_p \frac{R_1 R_2}{2R_0 + \alpha^2}, \quad (3.1)$$

is constant for all kinetic energy values. Here  $R_0$  is the mean radius of the hemispheres and  $\alpha$  is the angular half aperture of the electron beam at the entrance slit determined by the lens system. As a result of this, and the fact that this mode generally provides greater signal intensity for low kinetic energy photoelectrons, most PES spectra are acquired using the FAT mode.

## Twin Anode X-ray Source

The twin anode x-ray source is perhaps the most common lab based x-ray source used for PES. It works according to a few relatively simple principles illustrated in Figure 3.4. X-rays are generated as an anode material is bombarded with high-energy electrons emitted from a thermal source. The energy of the resulting x-ray transition is determined by the anode material, chosen both for its energy and for its line width. A twin-anode x-ray

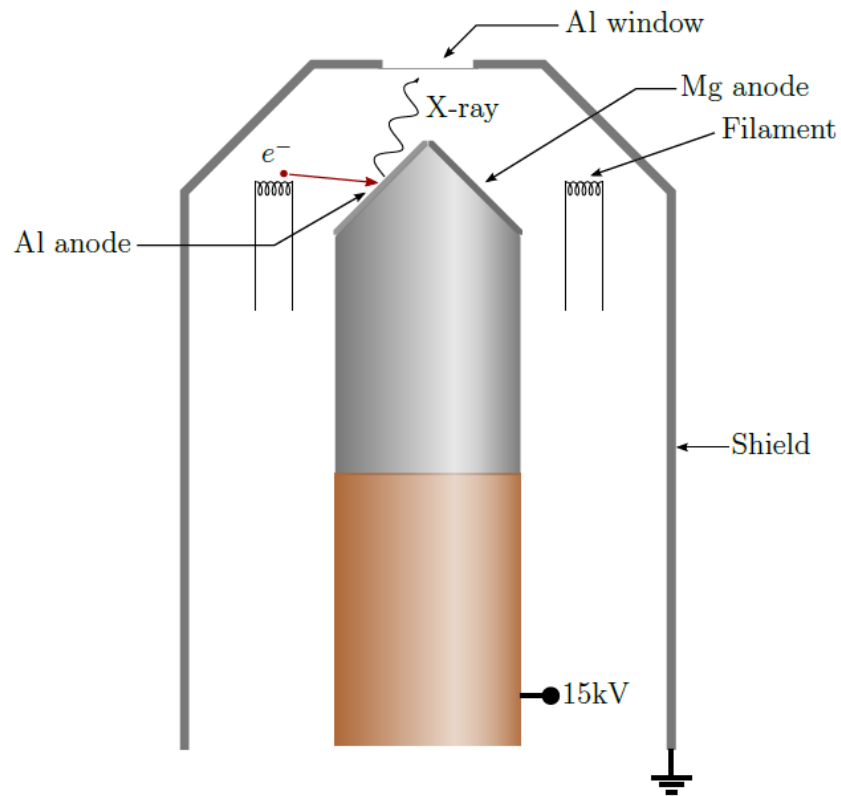


Figure 3.4: Illustration of the end of a twin-anode x-ray source. X-rays are produced as electrons emitted by filaments are accelerated on to an anode kept at high voltage. A twin-anode source is so named because its anode has two faces coated with different materials, enabling the production of two different sets of x-ray lines. The anode is housed within a shield which has an aluminium window at the end, permitting x-rays to travel through it.

source is so named because it has a twin-faced anode, each face coated with a different material, with aluminium and magnesium being the most common choices of anode material. The voltage applied to the anode can typically be set as high as 15kV, but the precise value which maximizes the efficiency of the x-ray emission depends on the anode material. Because the photon flux is proportional to the electron current hitting the anode it is generally desired to use as high values of current as possible. The electron bombardment of the anode produces a considerable amount of heat, however, and so the maximum current usable is limited by how fast this heat can be dissipated. Most twin-anode x-ray sources are therefore water cooled. As can be seen in Figure 3.4 the anode and the cathodes (filaments) are housed within a shield topped with an aluminium window. The purpose of this design is primarily to shield the sample from the high potential of the anode, but it has a couple of other advantages as well. Specifically from the aluminium window which filters out some of the bremsstrahlung radiation as well as certain secondary x-ray transitions.

Many setups using twin-anode x-ray sources also come equipped with monochromators, mostly in the form of quartz diffraction gratings. Using a monochromator provides a number of advantages. First and foremost, it reduces the x-ray line width (from  $\approx 0.9\text{eV}$  to  $0.25\text{eV}$  for  $\text{AlK}\alpha$ ) increasing the energy resolution of any measurements. A second advantage is naturally that it removes the unwanted portions of the x-ray spectrum, namely satellite peaks and the bremsstrahlung continuum. However, a certain amount of the x-ray flux is lost in the process, and so the choice of whether or not to use a monochromator is a trade off between resolving power and acquisition time.

## UV Sources

Although there exists a number of different ways to produce ultraviolet radiation, the most common UV sources used in PES experiments are plasma discharge lamps. These again come in many different designs, but this section will mainly concern itself with the two types of discharge lamps used in this experiment.

The lamp in the Trondheim setup is a SPECS UVS 10/35, a simple yet elegant and powerful design. It is a type of hollow cathode lamp which consists in simple terms of a large hollow cylinder cathode, an anode and a buffer gas. A large voltage applied across the cathode and anode ionizes some of the gas, creating a plasma. Atoms and ions in the plasma can become

excited by colliding with each other. When they subsequently relax to lower states they emit photons with energies characteristic of the atoms they came from. This light is then guided from the lamp towards the sample through a quartz capillary. In order for it to be possible to maintain high vacuum conditions in the analysis chamber while still allowing gas pressures in the lamp to be relatively high the device is differentially pumped.

The lamp in the St. Andrews setup, a SPECS UVS 300, is of a more complex design but in return is capable of offering both a higher photon flux as well as a smaller spot size than the UVS 10/35. It is a so called duoplasmatron light source. Meaning that it generates a plasma by guiding electrons emitted from hot filaments along the lines of a strongly inhomogeneous magnetic field towards a small discharge region. Within this region gas becomes ionized from the interactions with the electrons. As in the UVS 10/35 light produced in the plasma is guided to the sample through a quartz capillary. The UVS 300 can be fitted with a number of extra features such as a monochromator amongst others.

Both the UVS 10/35 and the UVS 300 can be operated with a number of noble gases, helium being the most common choice because it provides the best intensity and concentrates most of its spectral weight on one line, HeI (21.22eV). It is possible to adjust the relative output of HeI radiation to HeII (40.81eV) radiation by changing the pressure of Helium in the lamp. HeI radiation originates from unionized helium atoms while HeII radiation comes from singly ionized helium atoms. The UVS 300 is capable of producing a particularly high HeII intensity. While the UVS 300 produces more and better quality light, its more complex design means that it usually requires more maintenance than the simpler UVS 10/35. The addition of filaments in particular adds a potential source of disrepair.

## **e-Beam Evaporator**

An electron beam evaporator is a highly flexible tool that enables evaporating small quantities of almost any material at controlled and reproducible rates. The working principle of the device, illustrated in Figure 3.5, is fairly similar to that of the twin-anode x-ray source. A piece of material, either in the form of a rod or in a crucible, is kept at a 2kV potential and bombarded with electrons thermionically emitted from a filament. As the material heats up it starts to evaporate, releasing atoms with the thermal energy ( $< 1\text{eV}$ ).

The particular design employed in this experiment, the SPECS EBE-4,

has four pockets capable of simultaneous evaporation. Each of these pockets can also be run individually and is enclosed by a water cooled copper shroud preventing crosstalk between the pockets.

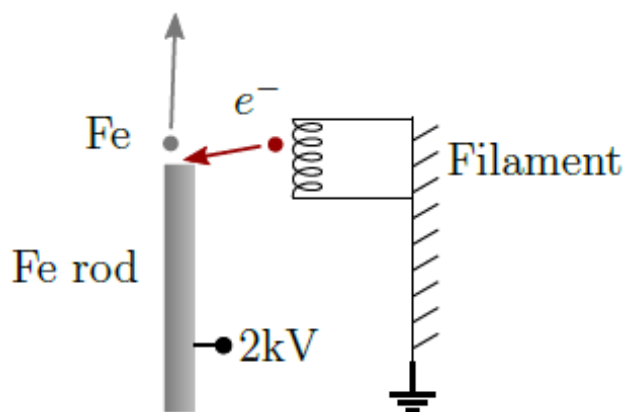


Figure 3.5: Illustration of the basic working principle of an e-beam evaporator. A piece of material, an Fe rod in this case, is kept at a 2kV potential and bombarded with electrons thermionically emitted from a filament. As the material heats up it starts to evaporate.



Figure 3.6: Naturally grown  $\text{MoS}_2$  crystal from a mine in Australia.

## 3.2 Sample Preparation

The experiments in this thesis were all performed on  $\text{MoS}_2$  samples taken from a naturally grown crystal. Figure 3.6 shows a picture of one such crystal. Being naturally grown, the crystal is polycrystalline, i.e. rather than being a large single crystal it is composed of a large amount of single crystals of varying sizes and orientations. In order to maximize the chance of obtaining a sample with sizable single domains, care was taken to extract them along the crystal's natural cleave planes whenever possible. The samples were then cut into appropriate sizes and affixed onto sample plates in one of two ways. Either by a silver epoxy adhesive, hardened by baking it at  $200^\circ\text{C}$  for about 20 minutes, or by tantalum clips spot welded onto the sample plate. In both cases it is important that the sample be in electrical contact with the sample plate in order to avoid charging problems, hence the choice of a conductive glue. Clips were used instead of the adhesive when the sample was to be subjected to temperatures higher than  $\approx 250^\circ\text{C}$  as the glue starts to degas above this point.

The techniques used in this experiment are surface sensitive and thus are reliant on samples having a clean surface in order to produce good results.

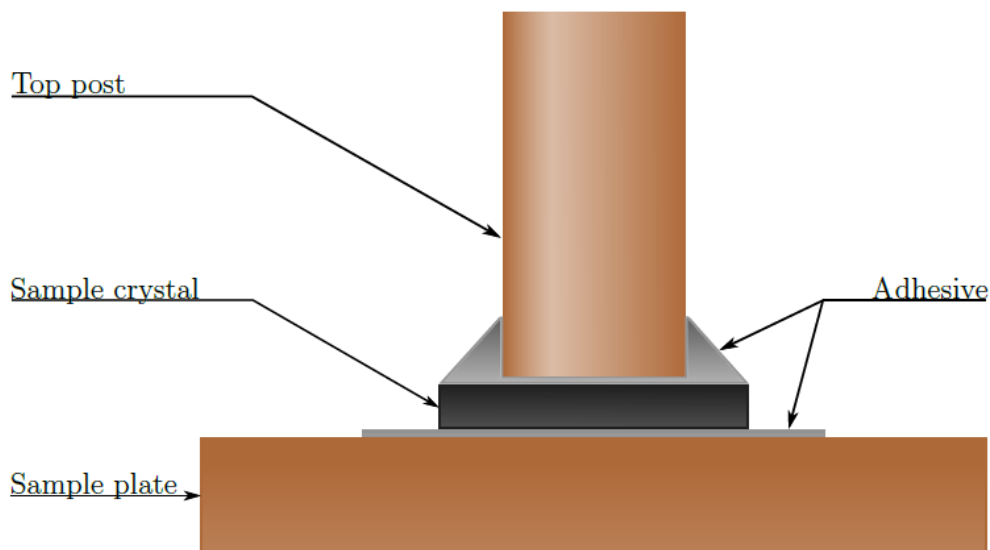


Figure 3.7: Schematic illustrating the top-post method of cleaving layered materials.

Typically surfaces are either grown in situ, or cleaned using a combination of sputtering and heat treatment techniques. Lamellar materials such as TMDCs, however, have a distinct advantage. Because of the weak inter-layer bonding it is relatively easy to remove the top layers of the sample, exposing a clean surface underneath. In this experiment two methods were used to mechanically cleave the  $\text{MoS}_2$ . The first method involved affixing a piece of adhesive tape to the top of the sample as well as to the load lock wall in such a way that the sample could be cleaved when it was moved further into the vacuum system. This method is commonly called the scotch tape method. The second method is known as the top-post method. It consists of gluing a post to the top surface of the material in the way shown in Figure 3.7. Once the sample has been transferred into the vacuum system this post can be knocked off, cleaving the sample. Unfortunately neither of these methods guarantee a good cleave. The surfaces exposed can be uneven and rough. Because of this the cleaving process was repeated until a good surface was exposed. The final step was to check the quality of the surface with LEED, and the sample for contaminants using XPS. For the ARPES measurements done in St. Andrews the sample was cooled to 20K using liquid helium and aligned in a direction of high symmetry using LEED.

### 3.3 Analysis of Experimental Data

#### XPS

An XPS spectrum can yield a wealth of information on both the elemental and chemical composition of whatever sample is being studied. Extracting this information, however, is not always straightforward. While a cursory analysis of a widescan, such as the one in Figure 2.8, can give an overview of what elements the sample contains, a more careful analysis of the various peaks in the spectrum is necessary to conclude anything precise on their chemical environment or even their relative quantities. The most important characteristics of a photoelectron peak in this respect are its location, i.e. at what binding energy it is centered, its shape and its area. In order to determine these with any degree of certainty, the former of the two in particular, it is typically necessary to curve fit peaks to the experimental data. A number of choices has to be made in doing this. It is necessary, for example, to choose the number of peaks to include in the fit, as well as the shape of each of these. Herein lies the central difficulty in analyzing XPS data. It is always possible to achieve a good fit simply by adding an arbitrary number of peaks, and there are a near infinite amount of ways to do it in. Clearly, it is difficult to say whether a given fit is representative of reality. A fit made without any constraints imposed upon it is unlikely to be correct. The choices made in the fitting process constitute assumptions about the physics involved and the state of the sample. As such the process must always be tempered and guided by knowledge of the photoemission process and of the sample chemistry. Spin-orbit split peaks are very useful in this regard, as the constant peak separation and peak area ratio provide constraints to use when fitting.

When fitting the photoelectron peaks it is necessary also to remove the background of inelastically scattered electrons. This can be done either simultaneously with the peak fitting or, as was the case in this experiment, as a separate step prior to the peak fitting. As explained in a previous section the shape of the background is determined by the loss processes electrons can undergo on their way out of the sample. It depends on a number of factors such as the material of the sample and the energy of the photoelectrons. Because of this a number of different approximations and models for the background exists. Figure 3.8 shows the removal of two different background types from the same example ARPES EDC. Although the backgrounds encountered in

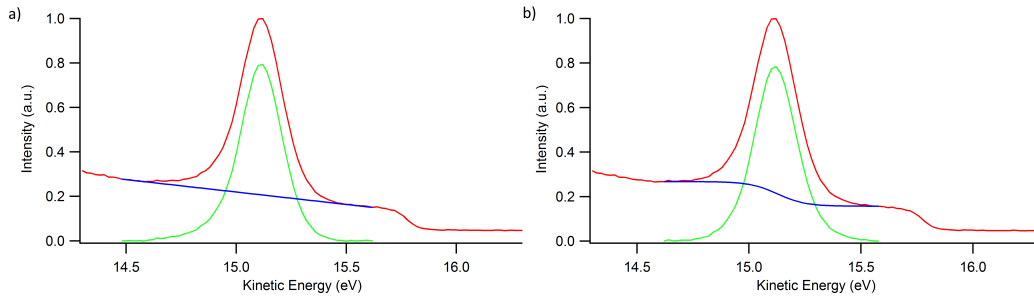


Figure 3.8: Illustration of the background removal process for an example ARPES EDC. Two different types of backgrounds are shown: a) linear background and b) Shirley background.

UPS, and ARPES by extension, are not entirely equivalent to those found in XPS (owing primarily to the kinetic energy dependence of the cross-section for the creation of secondary electrons[77]), the primary loss processes are the same and thus the background removal process is largely analogous to a first approximation. The linear background, shown in Figure 3.8 a), is the simplest approximation. It works best when the background changes little over the energy range spanned by the peak, e.g. in materials with large band-gaps, but is otherwise a rather arbitrary approximation. Figure 3.8 b) shows the background type used most frequently in this experiment, the Shirley background[78]. It is a better approximation that in a general way accounts for the inelastic scattering of the electrons. The main flaw in this background type comes from its most distinguishable feature, namely the sharp rise in the background at the peak. While this is a real effect its physical nature is misattributed by the Shirley background. The contribution to the energy loss background of a photoelectron peak arising from the transport of electrons through a solid is, by itself, not large enough at the peak location[79] to account for the rise. Instead a large fraction of this step corresponds to a shakeup excitation to a continuum of final states[80], and is thus intrinsic to the peak shape. This means that the Shirley background, although useful and widely used, has a couple of drawbacks. Naturally, using this background gives up the information which could otherwise be gained from the intrinsic part of the loss tail (it can for instance give some insights into bonding types). Furthermore, because this intrinsic loss depends on the chemical state the originating element is in, it could potentially lead to errors in quantification. Finally, the Shirley background is not well suited for more

complicated peaks with several components, as the background removed from the various components will be poorly defined. In such cases a different type of background defined by Tougaard[79] is more appropriate. Regardless of the method used, however, it is clear that the choice of background, as well as how it is removed, will change the shape and area of the photoelectron peaks and represents an additional source of error.

After the background has been removed, peaks are fit to the experimental data. The main choices to be made at this stage are the functional form of the peaks to fit and how many peaks to include. As was the case for the background a large number of synthetic line shapes exists. Recall that the line shape of most photoemission peaks will contain Lorentzian and Gaussian contributions both from physical and experimental origins. For this reason a natural choice for the peak shape, and the one most used in this experiment, is the so called Voigt profile, a convolution of a Gaussian and a Lorentzian. When fitting asymmetric peaks such as the Fe 2p peaks, either the Doniach-Sunjic[81] or a pseudo-Voigt profile with an asymmetry parameter[82] was used depending on what information was wanted. The former is a Gaussian-Lorentzian peak with a modified tail to account for the asymmetry of metallic peaks, and was used when precise peak positions and shapes were desired. The latter is a sum of a Gaussian and a Lorentzian, rather than a convolution, with an additional asymmetry parameter and was used when it was desired to extract the area of a peak. This was necessary because the Doniach-Sunjic profile does not have a well defined area. Choosing the number of peaks to include in a fit largely comes down to knowledge of the chemistry of the sample.

Analyzing UPS spectra was done in an analogous fashion.

## ARXPS

The main purpose of the angle-resolved XPS data collected in this experiment was to characterize the growth of the iron overlayer on the MoS<sub>2</sub> substrate, and to see whether the iron could be made to intercalate from heat treatment. To this end core level spectra of the relevant elements were acquired at various different sample tilt angles. Then the areas of these peaks were determined under the considerations outlined above. These were then normalized to each other at each angle step and plotted against the sample tilt angle. Rough relative depth plots were made by plotting the logarithm of the ratio of the peak area near grazing angle to that at normal emission for each species. This

plot is independent of any model and served as an aid in the analysis of the data. The thickness of the iron overlayers was calculated using equation 2.19. Additional considerations about this method of film thickness calculation are made in Appendix A.

## ARPES

Two different detector types, a one dimensional channeltron detector and a two dimensional CCD detector, were used to acquire ARPES data in this experiment. Consequently two different methods, outlined in section 2.3.2, were used to acquire the spectra. The treatment of the data varied accordingly.

Using the one dimensional channeltron detector in Trondheim each ARPES spectrum was composed of several UPS spectra taken at different sample tilt angles. These were combined postfact to create a two dimensional slice of the band structure. Acquiring ARPES spectra in such a manner is a time consuming process, a single spectrum could take upwards of five hours to acquire.

The situation is much improved when using a two dimensional detector such as the one in the St. Andrews lab. With this setup an equivalent ARPES spectrum can be taken in minutes rather than hours and with much better resolution. A different set of considerations must be made in the treatment of data acquired in this way. The prime example being that the recorded image of the photoemission intensity will initially be warped. Rather than being a rectangular grid in energy and angle it will instead be squeezed in angle at the lower electron energies due to the energy and angle dependence of the electron trajectory through the HSA. This was corrected for by applying a warp mesh supplied by the detector manufacturer to the image. Furthermore, the intensity scales of the spectra were corrected for dead pixels, i.e. pixels in the detector that always read out either nothing or maximum intensity.

Regardless of the detector used it is often desired to display the spectra as a function of  $\mathbf{k}$  rather than the angle. This is relatively straightforward for single images recorded at normal emission for which it suffices to use Equation 2.6.

After this it is common to extract EDCs or MDCs from the images and analyze them much as you would UPS spectra. In this experiment only EDCs were analyzed.

# Chapter 4

## Results

Over the course of this experiment measurements were carried out on a large number of different samples, prepared according to the exigencies of the experimental setups as well what they would be subjected to. Rather than give a precise accounting of each sample, this chapter will focus on the more important results and present them by theme. More details about the samples and their preparation will be provided where such information is necessary. The discussion and interpretation of the results will be left for a separate chapter following this one.

### 4.1 Sample Characterization

The samples studied in this experiment were all, without exception, extracted from the same naturally grown  $\text{MoS}_2$  crystal. Because of this, the initial stage of the experiment was dedicated to a brief check of the sample quality. Figure 4.1 shows XPS spectra of a clean  $\text{MoS}_2$  sample acquired in Trondheim using a  $\text{MgK}\alpha$  X-ray source. This sample was cleaved using the scotch tape method and measured at room temperature. The widescan in Figure 4.1 a) displays prominent molybdenum and sulfur peaks as would be expected. Other than a small amount of carbon, the spectrum does not indicate the presence of any other contaminating species in significant quantities. Figure 4.1 b) and c) show more detailed, fitted, core level spectra of the Mo 3d and S 2p peaks respectively. The binding energy of the Mo 3d  $5/2$  peak is found at 239.5eV, separated from the 3d  $3/2$  peak by a spin-orbit splitting of 3.15eV. Both of these results are in agreement with literature values for Mo in  $\text{MoS}_2$ [73, 83].

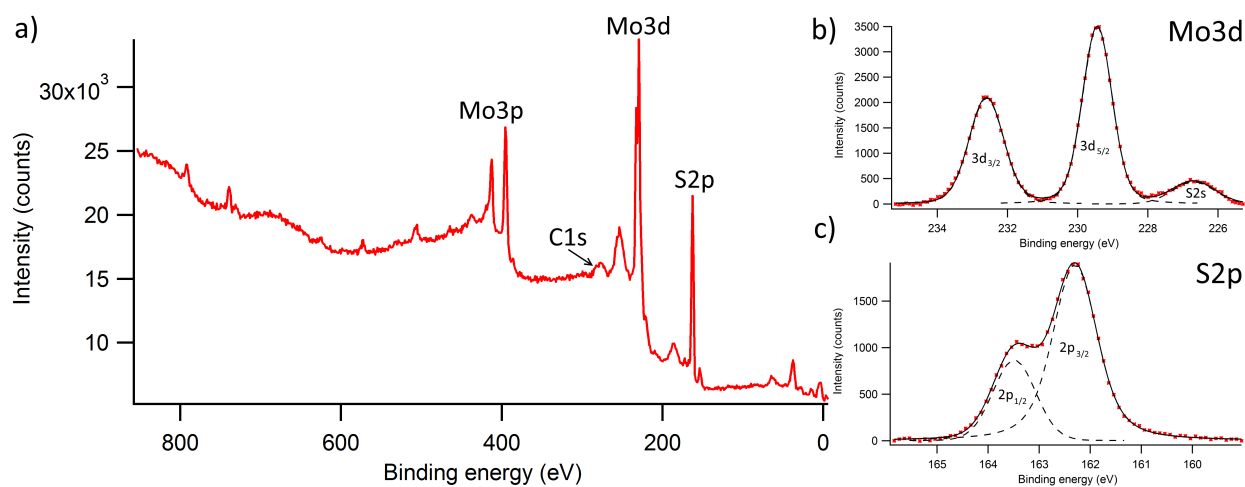


Figure 4.1: XPS spectra of a clean MoS<sub>2</sub> sample taken with MgK $\alpha$  radiation. a) shows a wide-scan with the major peaks labelled, while b) and c) show more detailed core level spectra of the Mo 3d and S 2p peaks respectively. In b) and c) the red markers indicate the experimental data while the black line is a fit to that data. The individual peaks making up the fit are marked by dashed lines.

The parameters of the S 2p peak, found to have a spin-orbit splitting of 1.2eV with the 2p 3/2 peak located at a binding energy of 162.3eV, are in similar agreement with literature values.

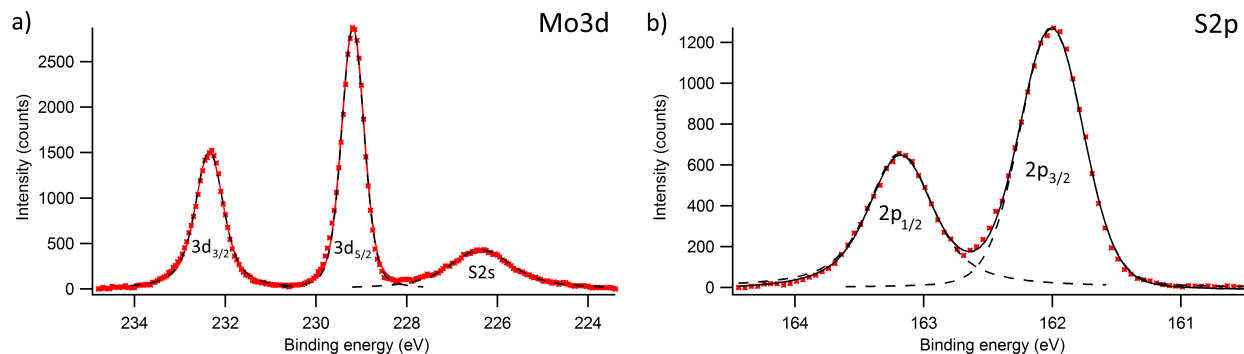


Figure 4.2: XPS spectra of a clean MoS<sub>2</sub> sample taken with monochromatized AlK $\alpha$  radiation. a) shows a fitted Mo 3d core level spectrum while b) shows a fitted S 2p core level spectrum.

A different set of Mo 3d and S 2p core level spectra taken in St. Andrews are included in Figure 4.2 for comparison. These are measurements of a top-post cleaved sample, taken using a monochromated AlK $\alpha$  source with the sample temperature at 20K. As is evidenced particularly well by the S 2p peak in Figure 4.2 b) (now resolved clearly into two separate peaks), the use of monochromatized radiation and to a lesser extent a reduced sample temperature results in better energy resolution. Both of these core levels display identical spin-orbit splitting to those in Figure 4.1 as would be expected. Interestingly, however, both the Mo 3d and S 2p peaks are shifted by 0.3eV towards lower binding energies.

In addition to verifying the chemical composition of the samples using XPS, the quality of the sample surfaces was investigated using LEED. Two LEED patterns taken at different electron beam energies are shown in Figure 4.3 a) and b). Both figures display distinct hexagonal patterns with little diffuse background scattering, indicative of a good quality surface. It was found that, provided a good cleave was obtained, most samples contained relatively large domains where good quality LEED patterns could be taken.

Figures 4.4 a) and b) show LEED patterns of two different, clean MoS<sub>2</sub> samples measured in St. Andrews. Although these patterns still demonstrate the hexagonal symmetry of the patterns in Figure 4.3, they are clearly of

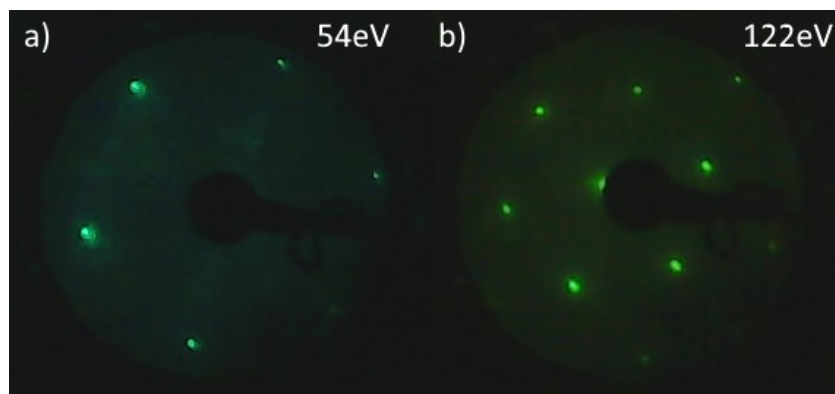


Figure 4.3: LEED patterns of a clean MoS<sub>2</sub> sample, cleaved using the scotch tape method, taken at 54eV a) and 122eV b) in Trondheim. The dark shadow in the centre of both images is the electron gun.

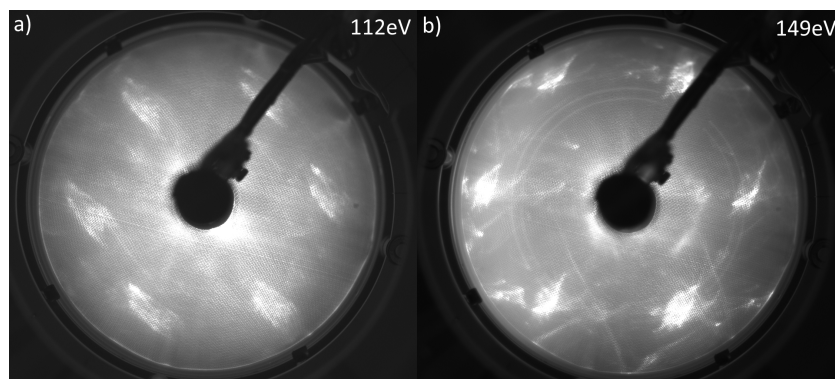


Figure 4.4: LEED patterns of two different clean MoS<sub>2</sub> samples both cleaved using the top-post method. The patterns were taken in St. Andrews using a beam energy of 112eV (a) and 149eV (b). It is not clear whether the poor quality of the patterns is due to optics, or to the sample surface quality.

lower quality. The spots appear to be split into several smaller spots and bright streaks can be seen in Figure 4.4 b). It is unknown whether the reduction in quality is due to the quality of the sample surface itself, or to the LEED optics. If it comes from the sample surface it could suggest the presence of stepped surfaces along with flat regions.

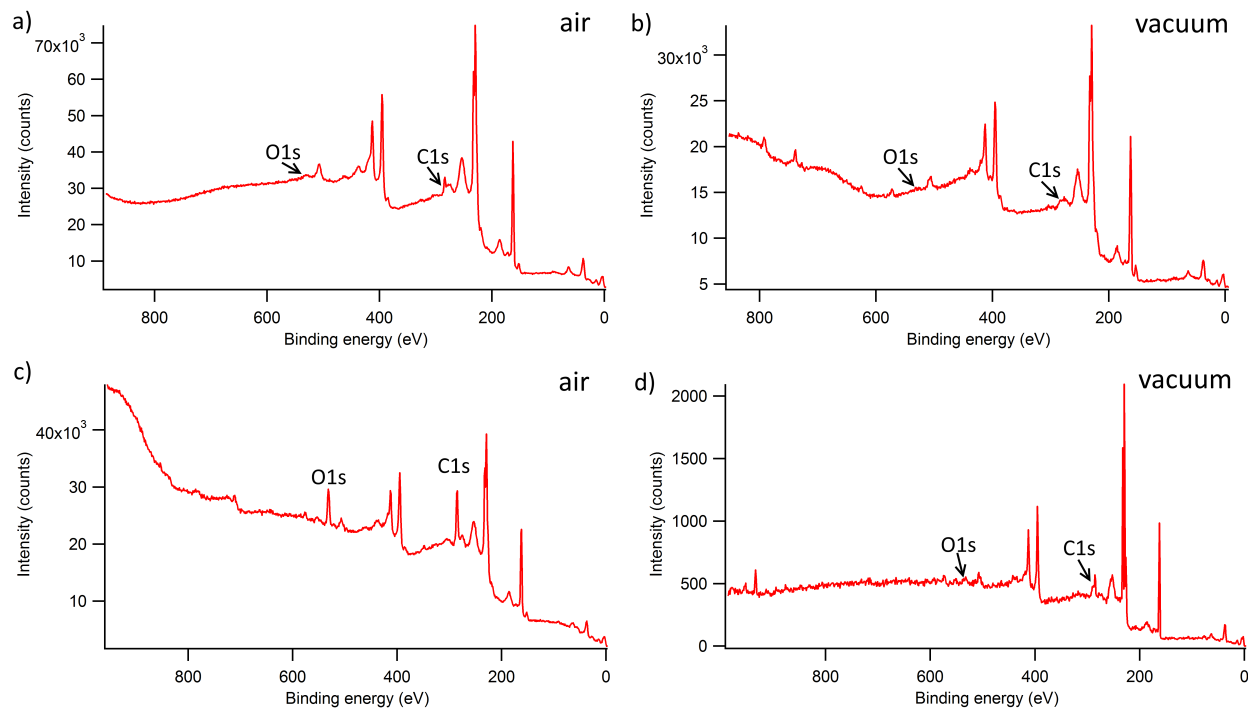


Figure 4.5: XPS widescans of four different  $\text{MoS}_2$  samples cleaved either in air (a) and c)) or in vacuum (b) and d)). All spectra were taken with  $\text{AlK}\alpha$  radiation (d) monochromatized  $\text{AlK}\alpha$ ). The positions of the O 1s and C 1s core levels are marked.

Although most samples were cleaved in vacuum in order to keep their surfaces clean, this was not practical in all cases. In particular the samples affixed to the sample plates using tantalum clips rather than glue did not reliably cleave well. Rather than gambling on getting a good cleave in vacuum these were instead cleaved in air immediately prior to loading them into the vacuum system. Figure 4.5 shows the resulting XPS spectra of four different samples, two cleaved in air (a) and c)) and two in vacuum (b) and d)). While samples cleaved in vacuum generally displayed lower amounts of carbon and

oxygen contamination, those cleaved in air remained remarkably clean due to the inertness of the  $\text{MoS}_2$  surface. Furthermore, much of the resulting contamination could be removed from the sample by heat treatment.

## 4.2 Fe Growth and Intercalation

Two different sources were used to evaporate iron onto the samples. The e-beam evaporator used in Trondheim produced iron at constant and reproducible rates, while the improvised iron doser used in St. Andrews proved more fickle. All film thicknesses reported in this section were calculated using Equation 2.19 with the areas of the Mo 3d and Fe 2p peaks. Values for the effective attenuation lengths were taken from the NIST EAL database[84].

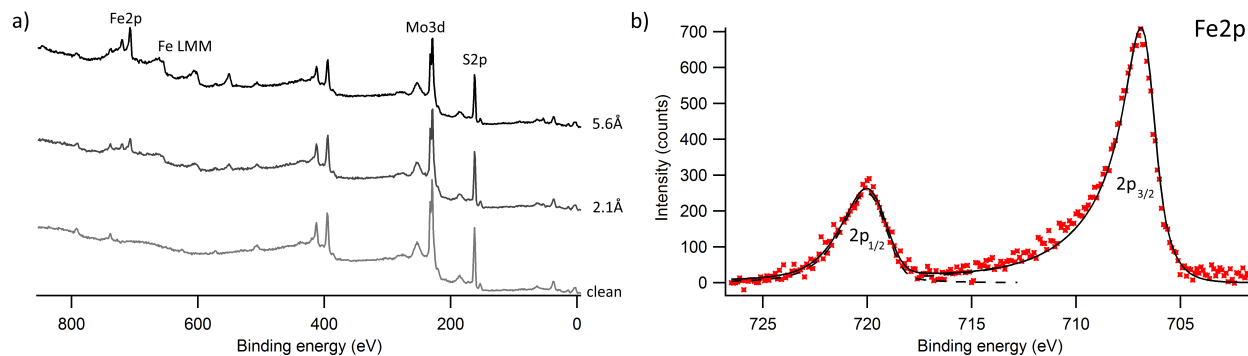


Figure 4.6: XPS spectra of  $\text{MoS}_2$  dosed with varying amounts of iron taken with  $\text{MgK}\alpha$  radiation. a) Three wide scans of  $\text{MoS}_2$  with (from bottom to top) no iron, a 2.1 Å overlayer and a 5.6 Å overlayer. b) shows a fitted Fe 2p core level from the sample with the 5.6 Å overlayer.

Figure 4.6 a) shows three widescans of the same sample dosed with different amounts of iron. Going from bottom to top it shows spectra of the sample with no iron, with a 2.6Å Fe overlayer, and with a 5.6Å Fe overlayer. It clearly shows how the both the Fe 2p and Fe LMM peaks increase in size with increasing amounts of iron. Additionally it shows, albeit less clearly, that the Mo and S peaks get progressively more attenuated. Next to it, in Figure 4.6 b), is a more detailed Fe 2p core level spectrum of the sample with the highest amount of iron. The 2p 3/2 peak is found at a binding energy of 706.8eV, consistent with metallic Fe. Figure 4.7 shows LEED patterns obtained on this sample before (a) and after the final deposition of Fe (b). Although there is an increase in the diffuse background scattering, the LEED spots remain sharp.

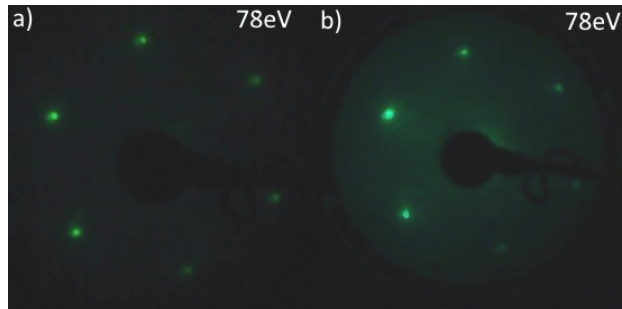


Figure 4.7: LEED patterns of MoS<sub>2</sub> before (a) and after (b) deposition of a 5.6Å Fe overlayer. Clearly the addition of iron does not destroy the pattern, but merely increases the diffuse background scattering.

A previous study has found that iron deposited on top of MoS<sub>2</sub> is only weakly bound to the substrate[51]. It has, however, also been shown that iron can be made to intercalate into MoS<sub>2</sub> to reside between layers[29, 85]. Left on the surface the iron will be more susceptible to oxidation and may be prone to thermal desorption. The latter arrangement therefore makes for a more robust and stable dopant configuration and is thus better suited for potential device applications. One possible way to achieve this is by annealing the iron dosed samples at elevated temperatures.

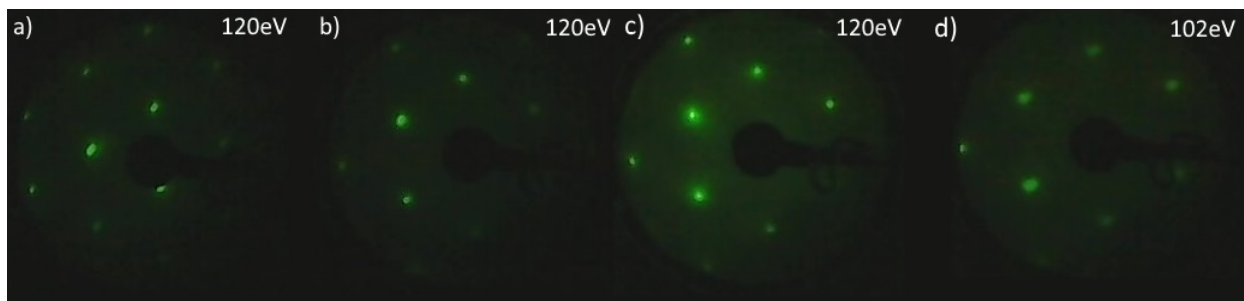


Figure 4.8: LEED patterns of a) clean  $\text{MoS}_2$ , b)  $\text{MoS}_2$  with a  $2.7\text{\AA}$  Fe overlayer, c) after annealing the sample to  $80^\circ\text{C}$ , and d) after exposing the sample to atmosphere.

Figure 4.8 shows a LEED series of such an experiment performed on a sample affixed to the sample plate with adhesive. By comparing the LEED pattern before iron dosing (Figure 4.8 a)) and after the addition of a  $2.7\text{\AA}$  overlayer (Figure 4.8 b)) it can be seen that, similar to the results in Figure 4.7, the addition of iron to the sample does not significantly alter the LEED pattern. Interestingly, there is in this case not an as noticeable increase in the diffuse background, likely because this sample has less iron on the surface. Following the iron dosing, the sample was annealed at  $80^\circ\text{C}$ . The temperature was not increased further due to significant pressure spikes during the annealing process. Again there was no major change to the LEED pattern, shown in Figure 4.8 c), but its diffraction spots are less sharp. Finally, as a preliminary check for intercalation, the sample was exposed to atmosphere. The thought being that, were the iron to have intercalated, it would not be oxidized. Evidently, the exposure to atmosphere did not destroy the resulting LEED pattern (Figure 4.8 d)), but again only made it more diffuse. This result suggests that the sample surface is not massively contaminated, but due to the small amounts of iron used it is not possible to conclude that the iron has intercalated. Indeed, the XPS spectra in Figure 4.9 confirms the former and contradicts the latter. From the widescan in Figure 4.9 a) it can be seen that the sample is only moderately contaminated by C and O. The Fe 2p core level in Figure 4.9, on the other hand, has shifted to a higher binding energy compared to the one in Figure 4.6 b). At a binding energy of  $711.1\text{eV}$  the Fe 2p  $3/2$  peak now demonstrates the presence of iron oxides. Furthermore, the lack of any peak distinguishable above the background at  $707\text{eV}$  suggests that most of the iron has oxidized. Of course, any amount of

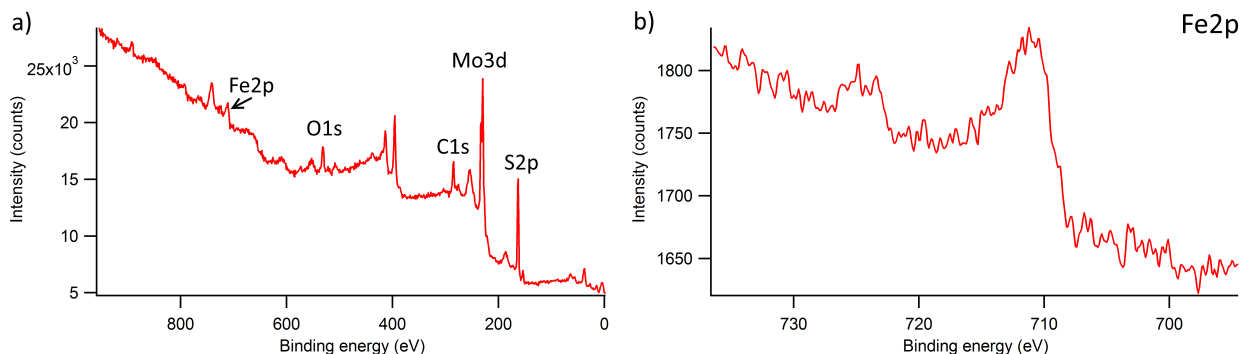


Figure 4.9: XPS spectra of annealed sample after exposure to atmosphere. The widescan (a) shows the presence of C and O on the surface while the Fe 2p core level (b) shows that the iron overlayer has oxidized.

iron that may have intercalated would be harder to detect due to attenuation by the overlayer.

These results, along with some preliminary ARXPS measurements, indicated that the iron did not intercalate in any significant quantities at temperatures of less than 100°C. However, raising the temperature of the samples above this point was accompanied by pressure spikes as well as a deterioration of the samples as shown in Figure 4.10. This figure displays XPS spectra of an iron dosed sample before and after annealing to 150°C. Both the widescan in Figure 4.10 a) and the C 1s and O 1s core level spectra in b) and c) show that the sample got more contaminated by C and O in the annealing process. The source of this contamination is believed to be the silver epoxy used to glue the samples to the sample plate. More specifically, air bubbles trapped in the glue which degassed during the heating. Another interesting point found in Figure 4.10 a) is the reduction in the Fe 2p peak. Naturally it would be expected to be somewhat attenuated due to the added surface contaminants, but the extent of the reduction in peak area suggests thermal desorption.

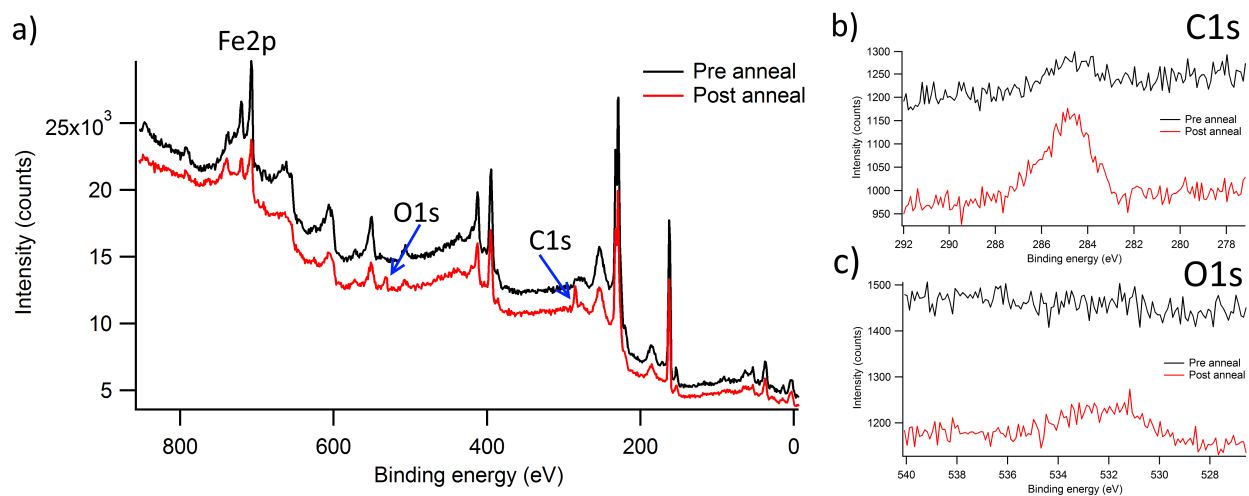


Figure 4.10: XPS spectra of an iron dosed  $\text{MoS}_2$  sample affixed by glue to the sample plate, before and after annealing to  $150^\circ\text{C}$ . The widescan (a) as well as the C 1s (b) and O 1s (c) core level spectra show that the sample got contaminated with C and O in the annealing process.

To combat the temperature constraints imposed by the glue, a new set of samples were prepared. Affixed this time by tantalum clips spot welded onto the sample plate. It was also desired to see what effect the annealing would have on the clean  $\text{MoS}_2$  surface. Figure 4.11 shows the resulting binding energy shifts in the Mo 3d core level (a) and in the S 2p core level (b) when annealing a clipped, clean  $\text{MoS}_2$  sample in stages up to a maximum of  $683^\circ\text{C}$ . Both core levels follow nearly precisely the same trend. Between room temperature and  $100^\circ\text{C}$  there is a shift of  $0.1\text{eV}$  towards higher binding energies. This shift remains constant until  $400^\circ\text{C}$  when the core levels shift again by another  $0.1\text{eV}$  towards higher binding energies. At the final stage the core levels shift back towards lower binding energies, ending up with a net  $0.11\text{eV}$  binding energy shift towards higher binding energies between the sample at room temperature and annealed to  $683^\circ\text{C}$ . Figure 4.11 c) shows the ratio of the areas of the Mo 3d and S 2p peaks plotted versus temperature. Interestingly the major changes in this plot occur at the same temperature steps as did the core level shifts. Those steps for which the Mo/S ratio is constant ( $100^\circ\text{C}$ ,  $200^\circ\text{C}$ ,  $683^\circ\text{C}$ ) had no core level shifts between them.

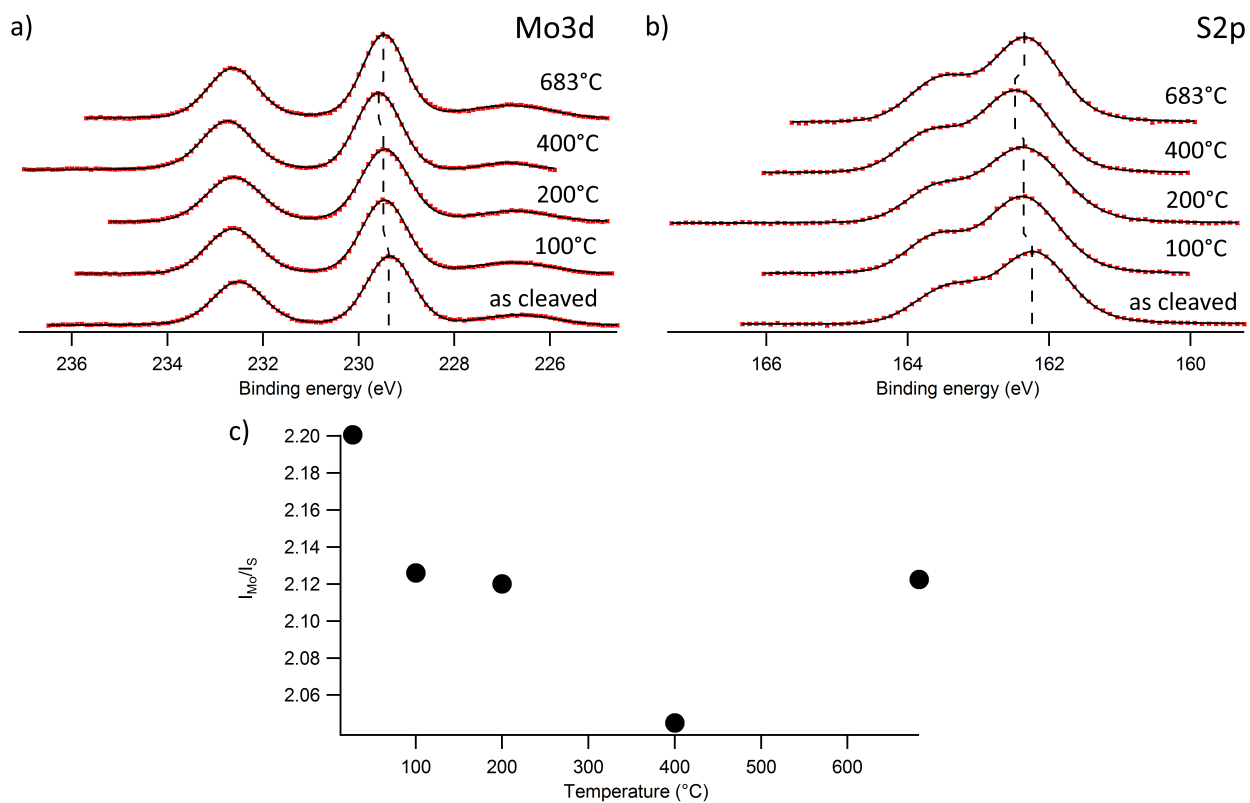


Figure 4.11: a) Mo 3d and b) S 2p core levels of clean MoS<sub>2</sub> sample annealed in increasing temperature steps. A dashed black line is included in both figures to help visualize the binding energy shifts. c) The ratio of the areas of the Mo 3d and S 2p peaks plotted versus temperature. Note that major changes to the core level binding energies occur at the same temperature steps as do the changes to the Mo/S ratio.

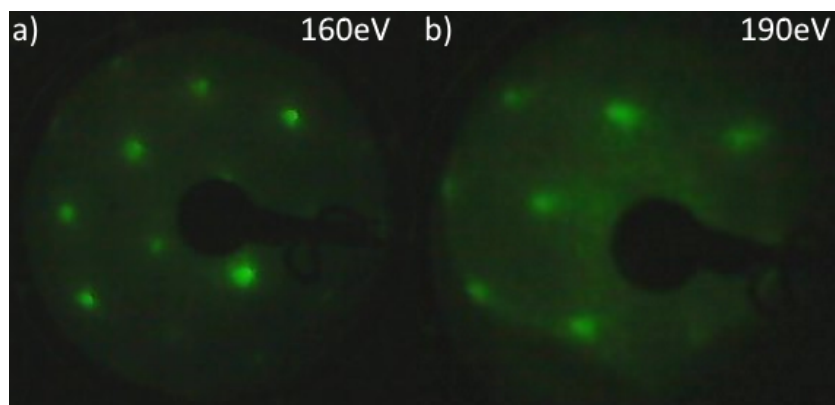


Figure 4.12: LEED pattern of clean MoS<sub>2</sub> sample before and after annealing to 683°C.

Figure 4.12 shows LEED patterns of the sample before (a) and after (b) the annealing process. It is included to show that the annealing process did not destroy the sample surface, though the pattern after annealing is more diffuse.

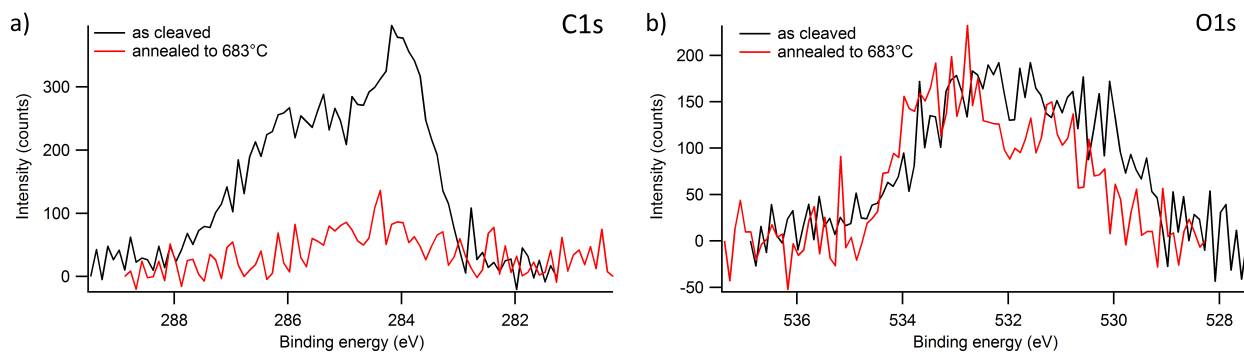


Figure 4.13: a) C 1s and b) O 1s core level spectra before and after annealing to 683°C. While the annealing process reduced the amount of carbon on the sample surface, it did not noticeably affect the amount of oxygen.

Contrary to what happened when annealing the glued samples Figure 4.13 a) shows that the annealing process removed physisorbed carbon from the sample. The amount of oxygen on the sample surface, however, remained more or less constant (Figure 4.13 b)).

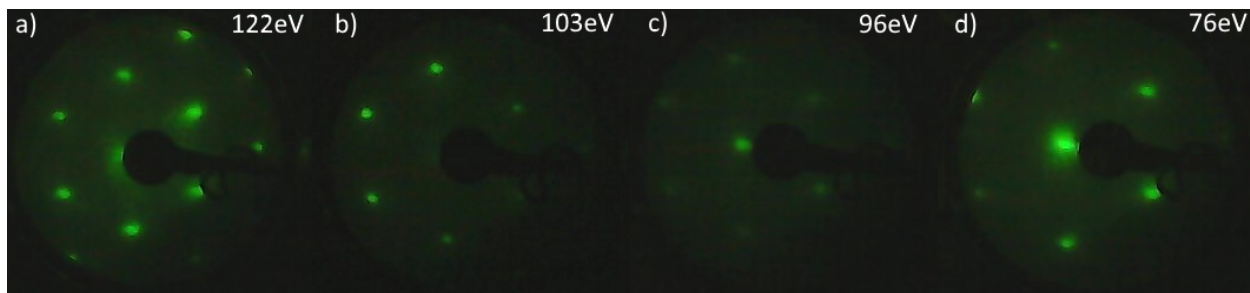


Figure 4.14: LEED patterns of a) clean MoS<sub>2</sub>, b) MoS<sub>2</sub> with a 2.4Å Fe overlayer, c) Fe dosed MoS<sub>2</sub> with the addition of a small amount of K, and d) after annealing the sample to 400°C.

The next step was naturally to dose a clipped sample with iron and then anneal it at high temperatures. Figure 4.14 shows a LEED series of one of these experiments, each pattern being representative of a unique stage of the experiment. The two leftmost subfigures show the diffraction patterns obtained before (a) and after (b) depositing a 2.4Å iron overlayer onto the sample. As has been well established by this point the addition of iron to the sample does not destroy the pattern. If anything the pattern after iron deposition shows less of a background, though this is likely caused by the settings of the LEED optics being better optimized in this case. Figure 4.14 c) shows the LEED pattern of the sample after deposition of a small amount of potassium onto the sample. The purpose and reasoning behind this will be refreshed in the next section. This time the addition of extra material to the surface resulted in a worsening of the pattern, with the diffraction spots being dimmer than they were before. The final pattern (Figure 4.14 d)) was taken after annealing the sample to 400°C. Evidently, the annealing process improved the LEED pattern: its spots are brighter though a bit less sharp.

Figure 4.15 are relative depth plots of the main species in the sample before (a) and after (b) annealing. It is meant to give a rough indication of the relative depth of these species in the sample. As would be expected, the relative depth plots place Mo and S furthest down both before and after annealing. Fe and K are both found nearer to the surface, with K above Fe as might be expected from the order of evaporation (first Fe and then K). Interestingly, the relative depth plot places C closest to the surface even though the amount of carbon appeared to remain unchanged after depositions (with a small attenuation after each deposition). There was, however, a 1.7eV

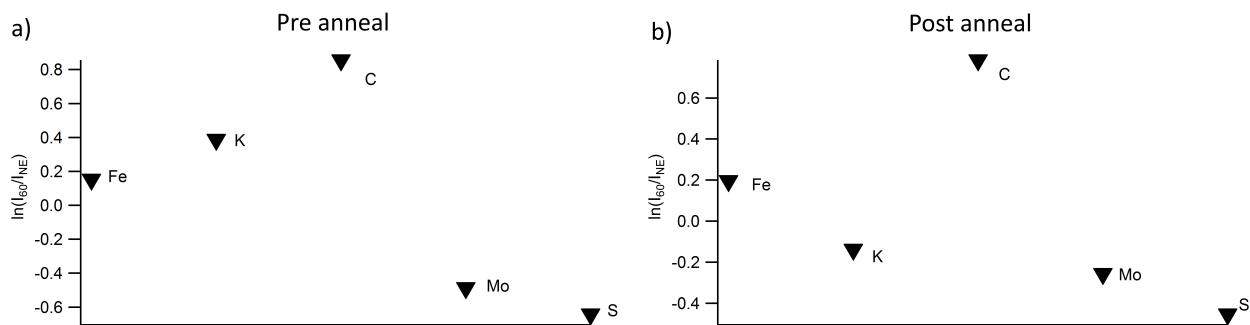


Figure 4.15: Relative depth plot of the species in the sample before (a) and after (b) annealing the sample to 400°C. This plot was constructed by taking the logarithm of the ratio of the peak area at high sample tilt to that at normal emission.

shift of the C 1s core level from a binding energy of 284.2eV to 285.9eV. This shift was not observed in any of the other core levels. The relative depth plot post annealing is similar to the one before with a few notable differences. Other than now placing K below Fe, the ordering of the species remains unchanged. It should be mentioned at this point that the data for K in the after plot carries a high degree of uncertainty because very little potassium remained after annealing. In addition to this it can be observed that the absolute difference between the Fe and Mo and S points has decreased.

Figure 4.16 displays the results of ARXPS measurements of the sample before (a) and after (b) annealing. It shows the areas of the most prominent core level peaks of the species of interest plotted versus sample tilt angle. The areas have been normalized to each other at each angle step. Two distinct trends make themselves clear in the series taken before annealing (Figure 4.16 a)): one for those elements determined to be closest to the surface in Figure 4.15 i.e. Fe, K and C, and another for Mo and S. The areas of Fe, K and C remain relatively constant at lower sample tilt angles before increasing more rapidly at higher angles. For the areas of Mo and S the situation is reversed. They too remain relatively constant at lower angles but instead decrease rapidly at higher angles. As a point of interest note that the areas of the C peaks show the most dramatic increase. Figure 4.16 b) shows the situation after annealing. Because both the K and C core levels were much diminished after the annealing, this figure includes only a few data points on these two elements, and even these should be considered with caution. The two

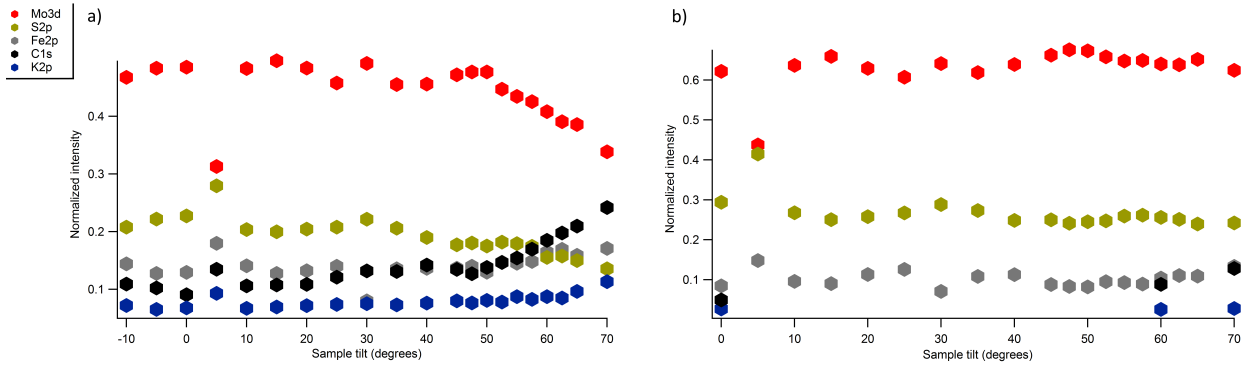


Figure 4.16: ARXPS measurements of a clipped  $\text{MoS}_2$  sample dosed with Fe and K before (a) and after (b) annealing to  $400^\circ\text{C}$ . The figures show the areas of the most prominent core level peaks (of Mo, S, Fe, K and C) normalized to each other and plotted as a function of the sample tilt angle.

trends identified before annealing appear to be mostly gone in this figure. Except for perhaps a slight increase in the Fe area at higher angles, most of the areas remain mostly constant over the angle series. In particular, the distinct drop in the Mo areas has disappeared.

Figure 4.17 is included to better illustrate the change in the ratio of the Fe and Mo areas. In it, this ratio is plotted versus sample tilt angle before (a) and after (b) annealing. A simple  $1/\cos(\theta)$  fit is marked by a blue line in both figures. While this appears to be a relatively good fit of the data prior to annealing, the same cannot be said for the data post annealing.

Both Figures 4.16 and 4.17 show indications of slight periodic variations in the peak area ratios. This variation is made explicit when plotting the ratio of the Mo and S areas as a function of sample tilt angle as is done in Figure 4.18 a) (pre anneal) and b) (post anneal). Both of these plots show clear peaks around 15 and 45 degrees. This is likely a diffraction effect occurring because the sample happens to be aligned along an axis of high symmetry. It can be seen in the LEED patterns in Figure 4.14 that the sample is aligned nearly precisely along  $\Gamma$ -M (keeping in mind that each of the diffraction spots represent  $\Gamma$  points). Whatever distance in the  $\text{MoS}_2$  crystal it corresponds to, it appears to be unaffected by the annealing and thus by the possible Fe intercalation.

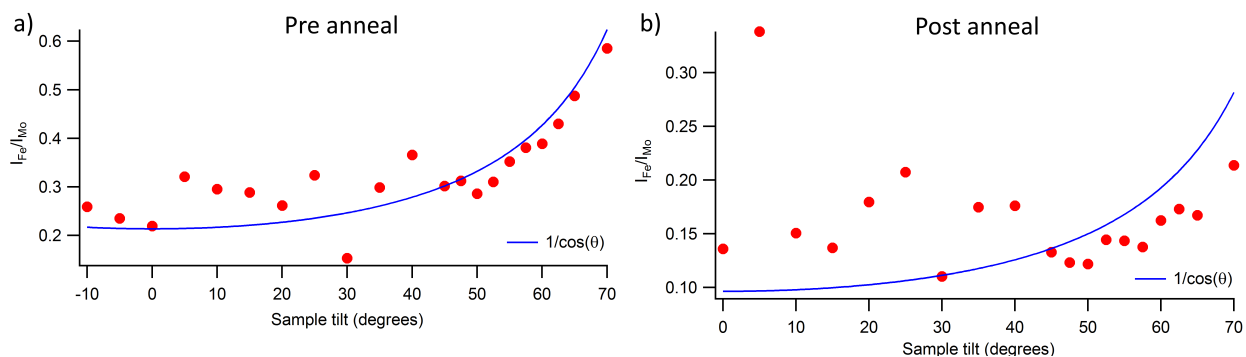


Figure 4.17: ARXPS measurements of a clipped  $\text{MoS}_2$  sample dosed with Fe and K before (a) and after (b) annealing to  $400^\circ\text{C}$ . It shows the ratio of the areas of the Fe 2p and Mo 3d core levels plotted versus the sample tilt angle. The blue line in each figure is a  $1/\cos(\theta)$  fit of the data.

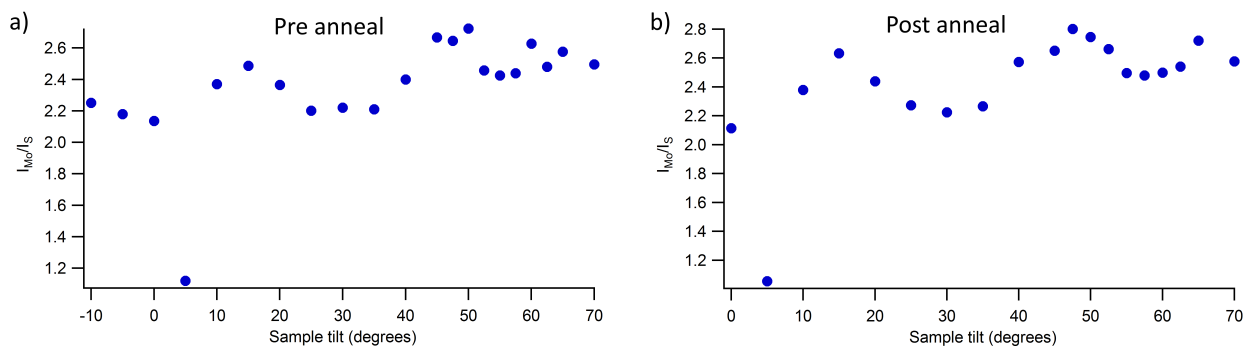


Figure 4.18: ARXPS measurements of a clipped  $\text{MoS}_2$  sample dosed with Fe and K before (a) and after (b) annealing to  $400^\circ\text{C}$ . It shows the ratio of the areas of the Mo 3d and S 2p core levels plotted versus the sample tilt angle. The plots show clear peaks at around 15 and 45 degrees.

### 4.3 Doping and Counter-doping

The addition of iron to the MoS<sub>2</sub> surface is expected to give rise to binding energy shifts of the core levels, either by doping or by other means. This section will present the core level shifts observed accompanying the Fe deposition.

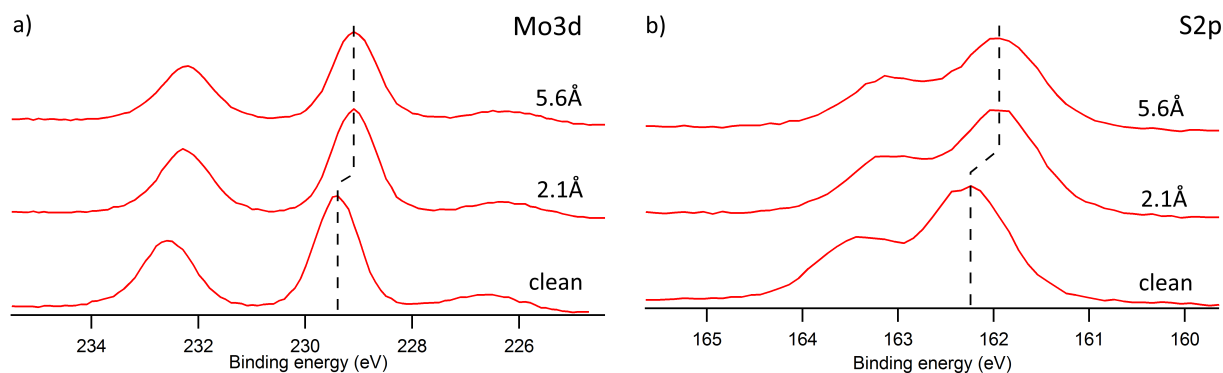


Figure 4.19: a) Mo 3d and b) S 2p core level spectra after successive depositions of Fe. These measurements were performed on a scotch tape cleaved sample at room temperature. The addition of a 5.6Å Fe overlayer to the sample causes a net shift of 0.3eV towards lower binding energies for both the Mo 3d and S 2p core levels.

Figure 4.19 shows the recorded Mo 3d (a) and S 2p (b) core levels following two successive iron depositions. Both core levels experienced a shift of 0.3eV towards lower binding energies after the deposition of a 2.1Å Fe overlayer. Increasing the amount of Fe on the surface to 5.6Å did not cause any further shifts. These measurements were performed in Trondheim on a scotch tape cleaved sample at room temperature.

Figure 4.20 displays a similar set of measurements performed in St. Andrews on a top-post cleaved sample at 20K. The results, however, are remarkably different. In this case the addition of Fe caused a net shift of 0.12eV towards higher binding energies for both the Mo 3d (Figure 4.20 a)) and S 2p (Figure 4.20 b)) core levels. Furthermore, this shift occurred gradually, increasing with each Fe deposition.

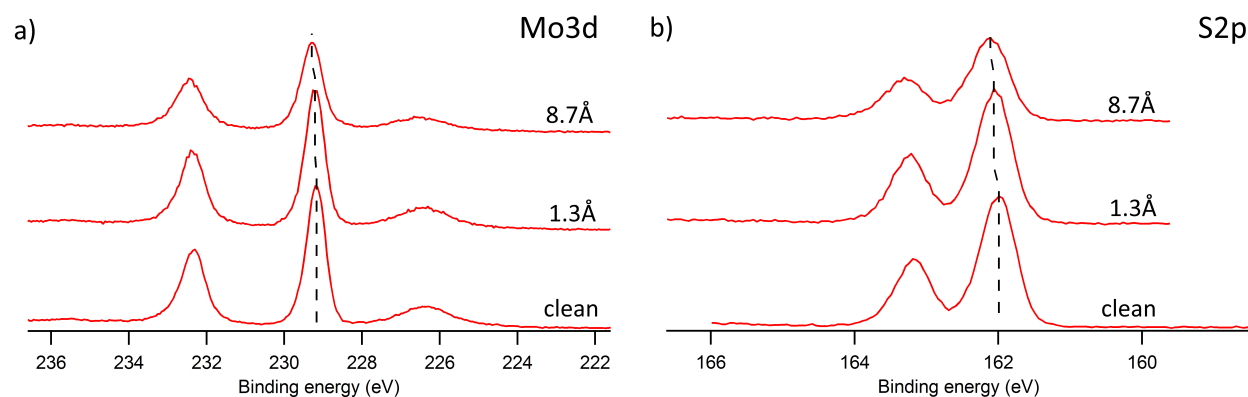


Figure 4.20: a) Mo 3d and b) S 2p core level spectra after successive depositions of Fe. These measurements were performed on a top-post cleaved sample at 20K. The addition of a 8.7Å Fe overlayer to the sample causes a net shift of 0.12eV towards higher binding energies for both the Mo 3d and S 2p core levels.

Figure 4.21 shows a widescan (a) and the Mo 3d (b) core level of a top-post cleaved sample after deposition of a large amount of Fe (estimated at 42Å). The Mo 3d core level now clearly has two components, marked in Figure 4.21 b) by 1 and 2 (though the fit overestimates the area of the leftmost peak of the second component). Additionally, both of these peaks are found at lower binding energies than the corresponding peak for clean MoS<sub>2</sub> in the same conditions. Referenced to the clean sample in Figure 4.20, the core level of the first component has been shifted by about 0.5eV to lower binding energies. The second component is shifted even further and is found at a binding energy of 227.7eV, consistent with metallic Mo. In addition to this, the S 2p peak in Figure 4.21 has been shifted to a binding energy of 161.5eV, consistent with sulfur in FeS.

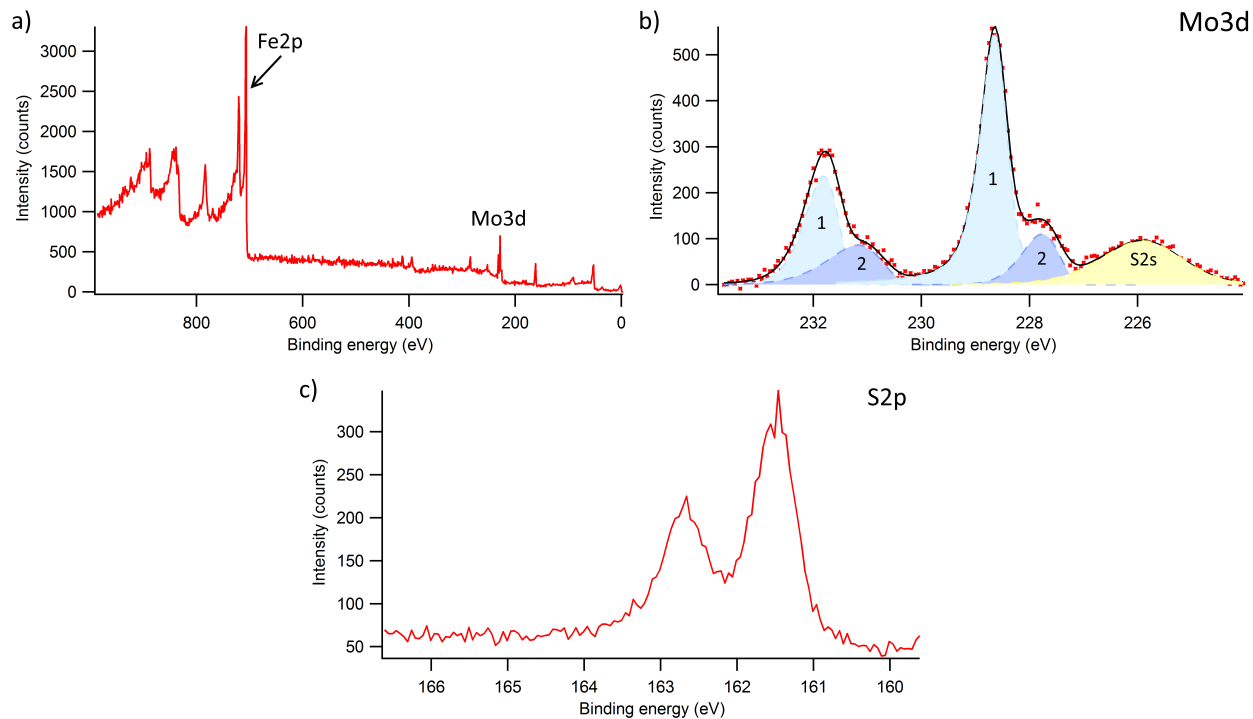


Figure 4.21: XPS widescan (a) and Mo 3d (b) and S 2p (c) core level spectra of a top-post cleaved MoS<sub>2</sub> sample with a 42 Å Fe overlayer. The Mo 3d core level has been fitted with asymmetric pseudo-Voigt profiles after the subtraction of a Tougaard background. It clearly shows two separate components marked by 1 and 2 (though the fit overestimates the area of the 3/2 peak of the second component). The S 2p core level has been shifted to lower binding energies compared to clean samples.

Following the observation in Trondheim that the Fe deposition shifted the core levels to lower binding energies, it was desired to explore whether it was possible to shift the core levels back by deposition of K, a known electron-dopant. The purpose of this being that any changes to the electronic band structure observed after Fe deposition could less ambiguously be attributed to magnetic effects. Figure 4.22 shows the resulting core level binding energy shifts of the experiment described in Figure 4.14. The separate stages of the experiment are marked by the numbers 1-5. These represent in order: the clean sample (1), the sample after Fe deposition (2), the sample after two successive K depositions (3 and 4), and after annealing the sample to 400°C. Similar to what was observed previously (Figure 4.19), the addition of a 2.1Å overlayer resulted in a 0.3eV shift towards lower binding energies in both the Mo 3d (a) and S 2p (b) core levels. The first dose of K caused a shift of around 0.5eV back towards higher binding energies in both core levels, while the second K dose caused a shift of 0.1eV towards lower binding energies. Annealing the sample caused a further shift by 0.2eV towards lower binding energies. From the results in Figure 4.22 c) it can be seen that the Fe 2p experienced a net shift of 0.2eV towards lower binding energies as a result of the K dosing. This shift was unaffected by the annealing, though clearly it served to diminish its area. Figure 4.22 d) shows the evolution of the K 2p and C 1s core levels in the last three stages of the experiment. Although it is difficult to say due to the low amounts of both elements present in the sample, there do not appear to be any shifts between the two successive K depositions. The annealing process caused most of both peaks to disappear. In what is left of the C 1s core level, however, it is possible to identify a shift of 1.3eV towards lower binding energies.

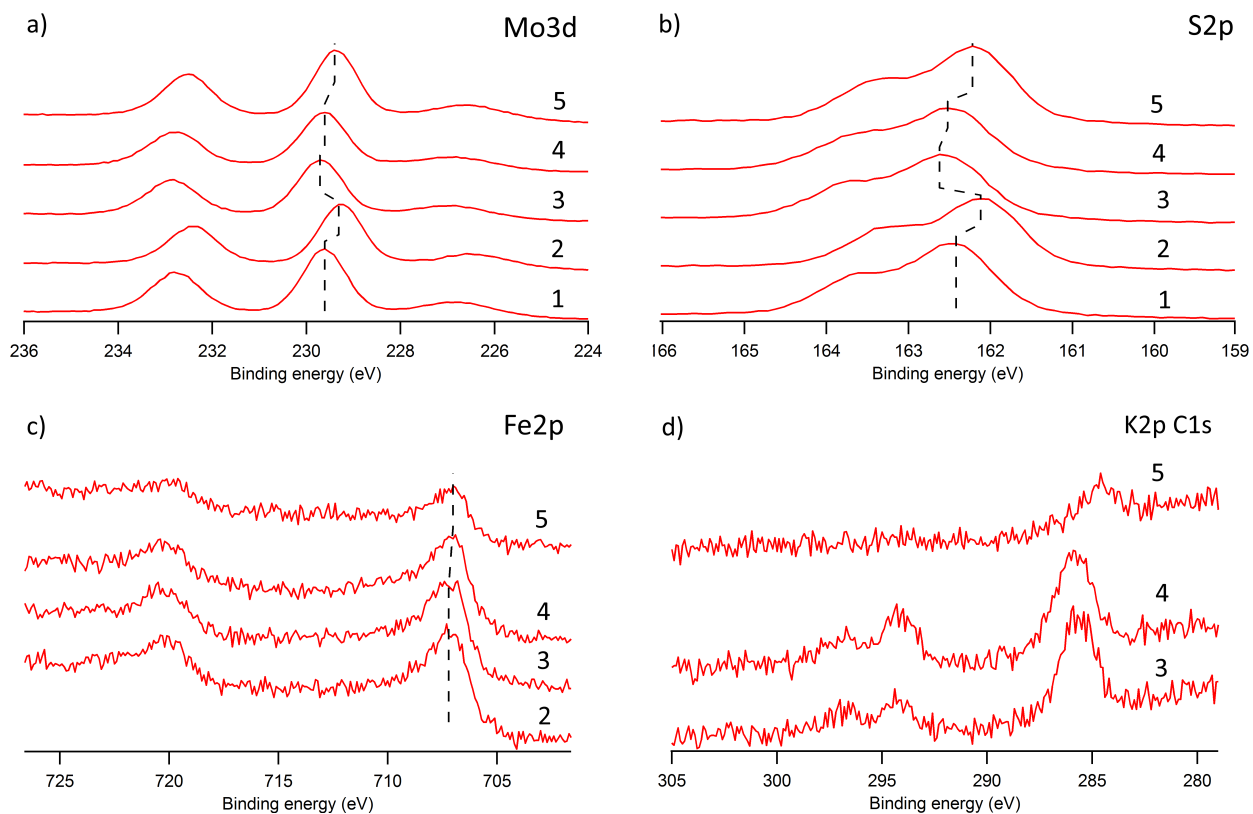


Figure 4.22: a) Mo 3d, b) S 2p, c) Fe 2p, and d) K 2p and C 1s core level spectra showing binding energy shifts through five stages of an experiment. The stages are labelled 1-5 in the following manner: 1: clean MoS<sub>2</sub>, 2: Deposition of a 2.1Å Fe overlayer, 3 and 4: two successive K depositions, and 5: after annealing the sample to 400°.

## 4.4 Preliminary Band Structure Measurements

As a conclusion to the experiments a series of preliminary ARPES measurements were made to look for any changes in the electronic band structure brought about by the magnetic doping.

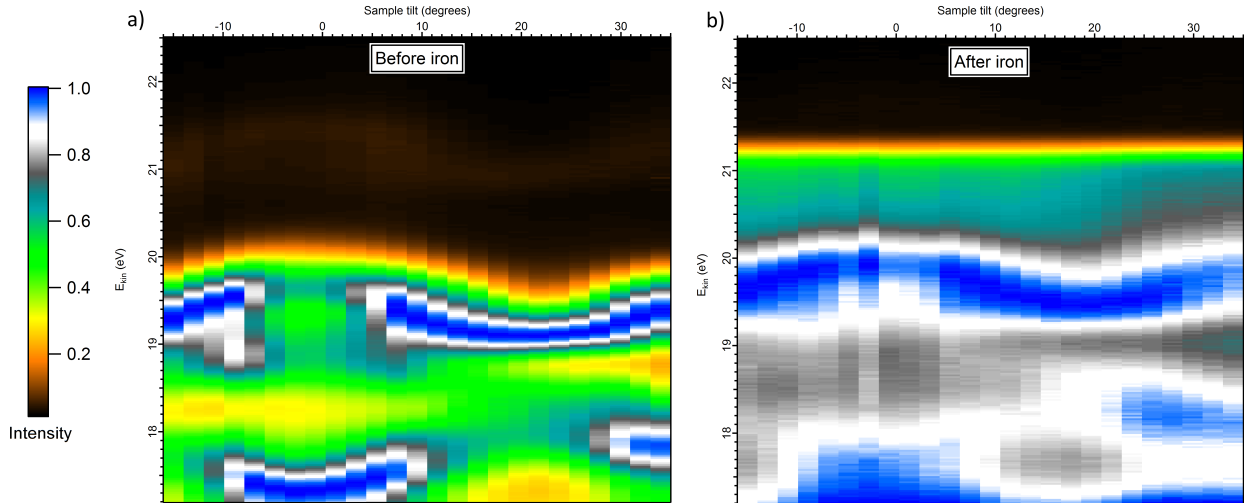


Figure 4.23: ARPES spectra taken using a 1D detector and the He I $\alpha$  resonance line of a MoS<sub>2</sub> sample before (a) and after (b) deposition of a 6.8Å Fe overlayer. The addition of Fe to the sample introduces a clear Fermi edge to the spectrum post deposition.

Figure 4.23 show a couple of ARPES spectra taken of an MoS<sub>2</sub> sample before (a) and after (b) deposition of a 6.8Å Fe overlayer acquired using a 1D detector. The LEED pattern of this same sample presented in Figure 4.3 shows that the ARPES spectra represent cuts approximately through  $\Gamma$ -K. Albeit of relatively poor angular resolution both the spectrum before and after iron deposition show clearly dispersing bands. Figure 4.24 contains two of the UPS spectra used to construct the ARPES images, both taken at a sample tilt angle of 7.45 degrees. The most striking change to the band structure following the iron deposition, seen both in Figure 4.23 b) and 4.24, is the appearance of a distinct Fermi edge. In addition to this the band structure of the iron doped sample has been shifted by 0.3eV towards higher kinetic energies (or lower binding energies), comparable to the shift seen in the core levels for the similarly scotch tape cleaved samples. As can be seen

particularly well from the EDCs in Figure 4.24, the peaks in the EDC after Fe deposition are less clearly resolvable above the background.

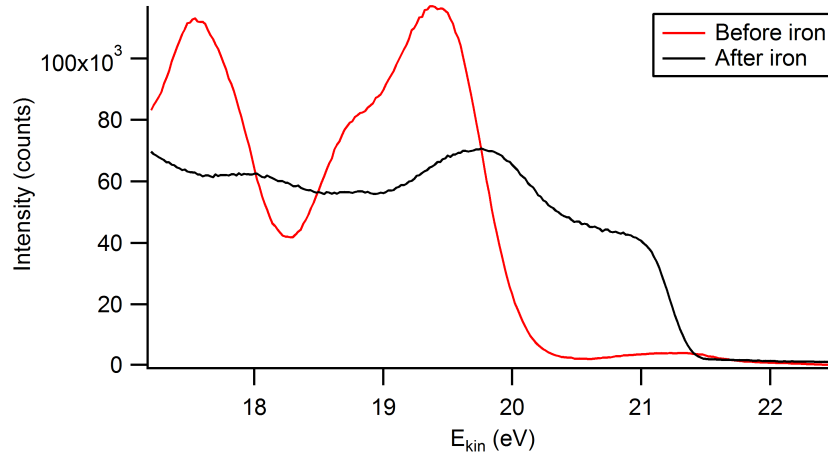


Figure 4.24: UPS spectra taken using the He I $\alpha$  of a MoS<sub>2</sub> sample before (red line) and after (black line) deposition of a 6.8Å Fe overlayer taken at a sample tilt angle of 7.45 degrees.

Figure 4.25 is a composite image showing the dispersion along  $\Gamma$ -K acquired on a clean MoS<sub>2</sub> sample using a 2D detector. As already indicated from the measurements in Figure 4.23, the sample displays well-resolved, clearly dispersing bands.

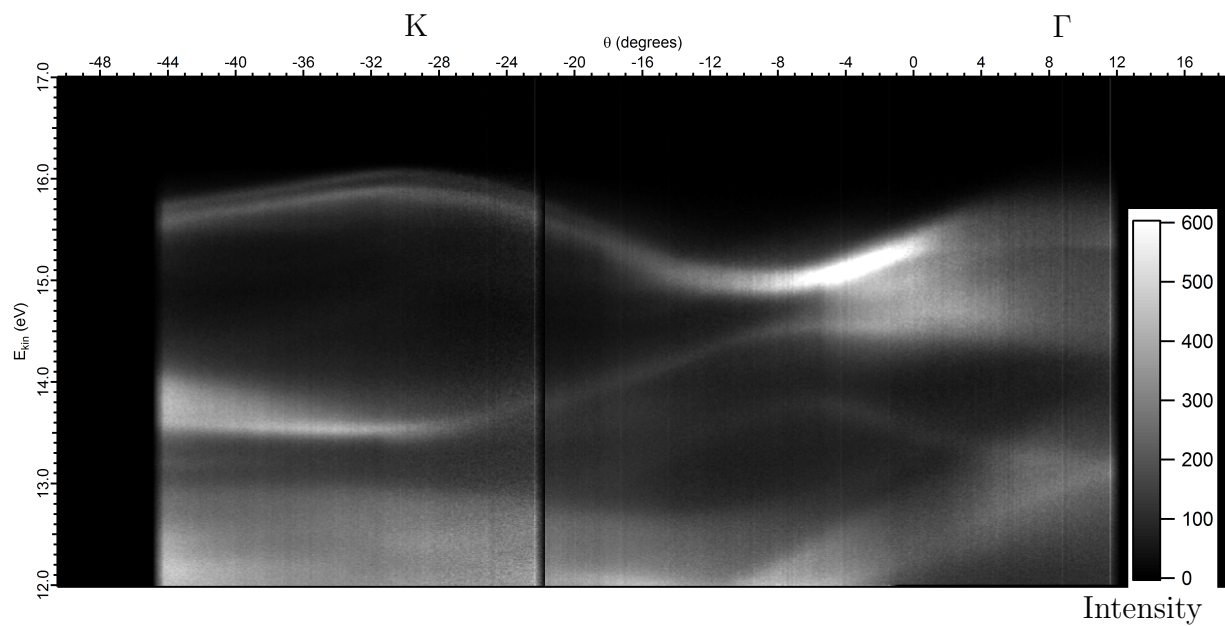


Figure 4.25: ARPES spectrum of  $\text{MoS}_2$  taken using the He  $I\alpha$  resonance line and a 2D detector. It is a composite image, made up of several individual spectra, showing the dispersion along  $\Gamma$ -K. The dark line at -22 degrees comes from an interruption in the functioning of the UV source.

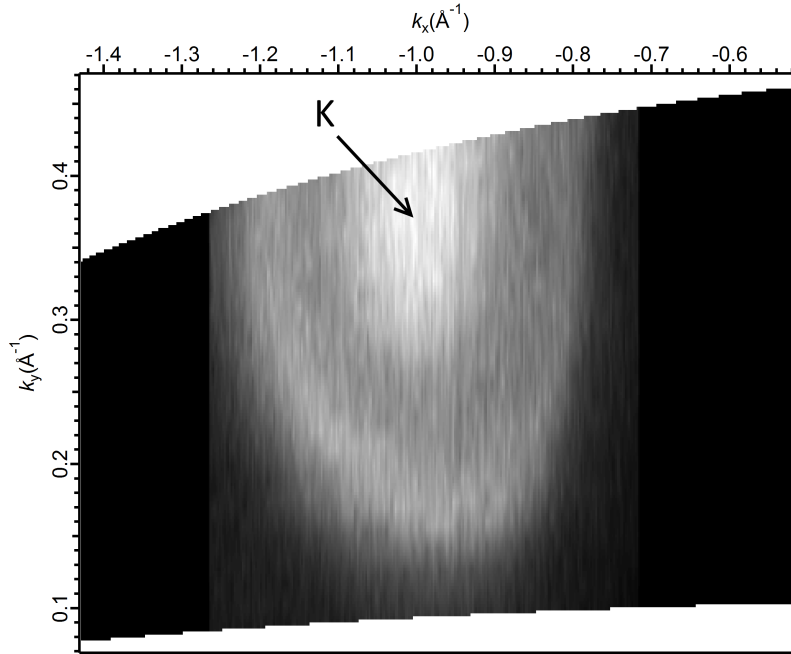


Figure 4.26: Constant energy cut at 15.92eV (kinetic energy) in the vicinity of the K point. A map such as this can be used to precisely orient the sample to the desired place in the Brillouin zone.

Understanding the nature and origins of valence band splitting is important because it plays a large part in governing the spin and valley physics of materials. In MoS<sub>2</sub> it has been found that a combination of spin-orbit coupling and interlayer coupling plays a significant role in the splitting of the valence bands at the K point[86]. This, along with their interesting spin texture, make these bands a reasonable choice for assessing the effects of the Fe doping. Figure 4.26 is a constant energy cut (at 15.92eV) in the vicinity of the K point. Such maps were used to precisely align the sample at the correct location in reciprocal space.

Figure 4.27 shows the measured valence band structure around the K point of a MoS<sub>2</sub> sample before and after deposition of a 1.3Å Fe overlayer. EDCs extracted at the K point ( $k_{||} = 0$ ) are presented in Figure 4.28 a) (before) and b) (after). Both the spectrum and the EDC of the clean sample show two clearly distinct valence bands separated by an energy of about 0.17eV. The difference in energy scale between these spectra and those taken

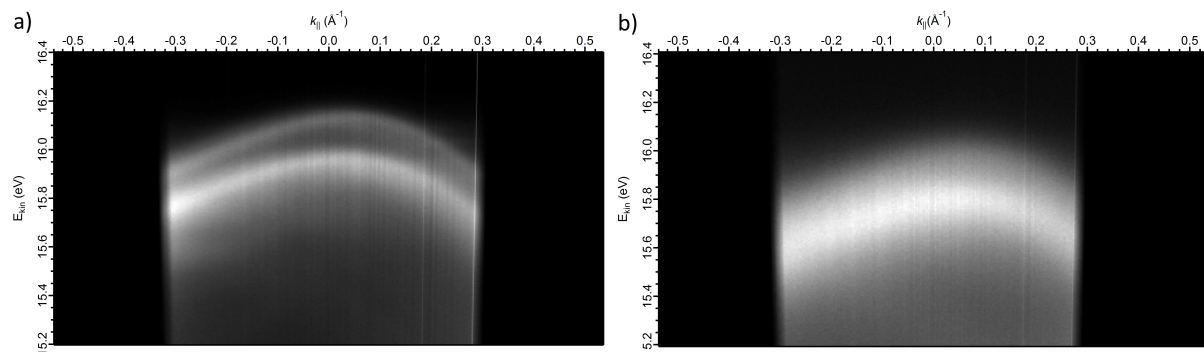


Figure 4.27: ARPES spectra taken using the He I $\alpha$  resonance line. The figures show the valence band structure around the K point of MoS<sub>2</sub> before (a) and after (b) deposition of a 1.3  $\text{\AA}$  Fe overlayer.

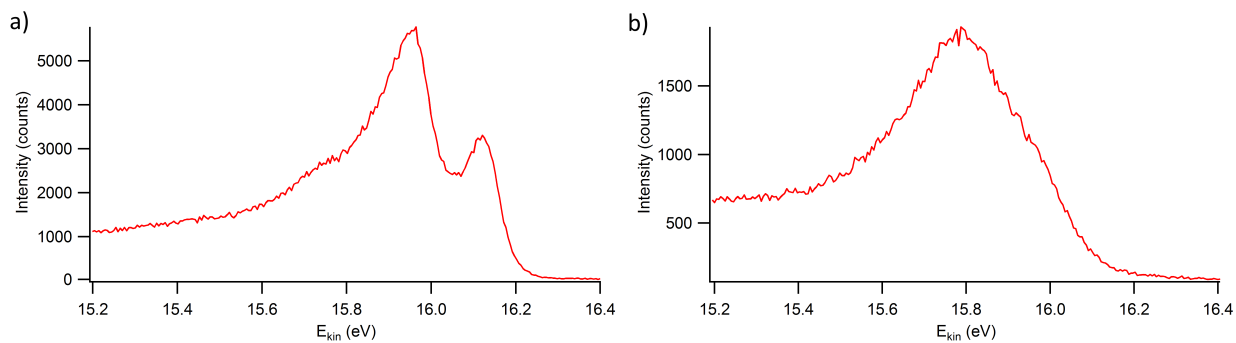


Figure 4.28: EDCs extracted from the ARPES spectra in Figure 4.27 directly at the K points. As in that figure, a) is the sample before Fe deposition and b) is the sample after.

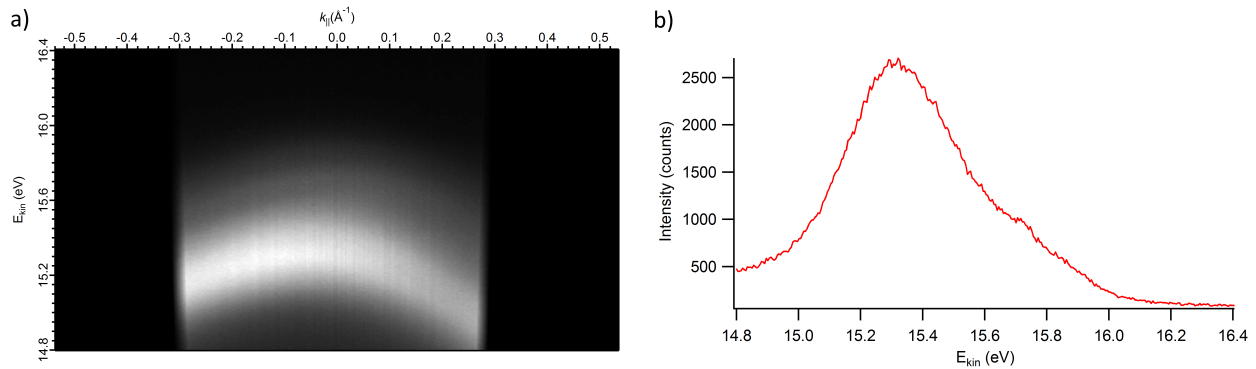


Figure 4.29: a) Measured valence band spectrum at the K point for a  $\text{MoS}_2$  sample with a  $1.2\text{\AA}$  Fe overlayer. b) EDC extracted at the K point.

with the 1D detector is mostly due to the work function (around  $4.35\text{eV}$ ) not being accounted for in the 2D data. As can be seen in Figures 4.27 b) and 4.28 b), the addition of Fe to the sample resulted in the bands becoming more diffuse. The two valence bands are no longer clearly distinct, but are hinted at in the EDC (by the main peak and a shoulder in Figure 4.28 b)). Though the separation between the bands appear to remain unchanged at  $0.17\text{eV}$ , the whole feature has been shifted by  $0.17\text{eV}$  towards lower kinetic energies (higher binding energies). Unlike what was the case for the shift in the spectra in Figure 4.23, this shift does not mirror the shift seen in the sample's core levels which can be seen in Figure 4.20. Instead it is greater by a factor of about 2.5. If the Fe dosing caused any of the bands to split further, no clear evidence for this can be seen in this data. Following this, more Fe was deposited onto the sample, increasing the Fe overlayer thickness to  $8.7\text{\AA}$ . This, however, had the result of making the bands too diffuse to be discerned.

Figure 4.29 a) shows the same valence bands recorded on a different  $\text{MoS}_2$  sample with a  $1.2\text{\AA}$  Fe overlayer, while Figure 4.29 b) is the EDC extracted at the K point. Despite being dosed with a comparable amount of Fe the resulting spectrum is noticeably different. First of all the most intense part of the spectrum is found at a kinetic energy of  $15.3\text{eV}$ , around  $0.65\text{eV}$  further towards lower kinetic energies than that of the clean sample in Figure 4.27 a). The energy span of this bright feature is comparable to the energy separation of the valence bands found in the clean sample. Furthermore, this spectrum has what appears to be an additional band at around  $15.7\text{eV}$  kinetic energy.

# Chapter 5

## Discussion

As mentioned in the previous chapter the work presented in this thesis included measurements on a large number of samples. While that chapter focused on the key results from the best samples, this chapter will attempt to give a more holistic description of the experiment and its findings. The intent being to distill from the experiment that knowledge which will be most useful to further, more detailed investigations of the effects of magnetically doping TMDCs. To that end this chapter will largely follow the structure of the previous chapter, discussing and interpreting the results of the major stages of the experiment. In addition, some of the more interesting results will receive special attention.

### 5.1 Sample Characterization

Overall the quality of the samples extracted from the naturally grown MoS<sub>2</sub> crystal exceeded expectations. As demonstrated by the XPS results in Figure 4.1 the sample was found to contain no major impurities. Certain parts of the crystal, however, were found to contain slightly higher amounts of carbon and oxygen than elsewhere in the crystal. The samples were mostly found to cleave well, depending primarily on how it was extracted from the natural crystal. With those samples cleanly extracted along natural cleave planes cleaving consistently well. Such samples contained relatively large domains wherein good quality LEED patterns, such as the ones in Figure 4.3, could be obtained. The most telling gauge of the sample quality, however, came in the form of the band structure measurements. Both the spectrum in Figure

4.23 a) taken with a 1D detector, as well as the spectrum in Figure 4.25 taken with a 2D detector show clearly resolved dispersing bands.

The data acquired in this experiment are on their own not sufficient to conclude with absolute certainty which polytype (or polytypes) of MoS<sub>2</sub> is present in the sample. However, the rarity of the 3R polytype in naturally grown MoS<sub>2</sub>[41] combined with the fact that it is most often observed alongside some impurity[40], makes it likely that the majority of the natural crystal is made up of the 2H polytype. This is further backed up by the band structure measurements, more specifically by the energy separation between the two valence bands at the K point seen in Figure 4.27 a). The magnitude of this splitting has been calculated to be smaller for 3R-MoS<sub>2</sub> than it is for 2H-MoS<sub>2</sub>[28], at 0.14eV for the former and 0.17eV for the latter, precisely what was observed in this experiment.

Most samples studied in this experiment were cleaved in vacuum in order to minimize the amount of contamination on their surfaces. Some, however, were cleaved in air immediately prior to insertion into the vacuum system. The results showcased in Figure 4.5, though of extreme cases, are representative of both methods. While cleaving in vacuum generally yielded cleaner sample surfaces, samples cleaved in air generally displayed relatively small amounts of contamination due to the inertness of the MoS<sub>2</sub> surface. Furthermore, most of this contamination could be removed by heating the sample (exemplified in Figure 4.13). In situations where cleaving in vacuum proves impractical (due to sample mounting, setup of the vacuum system or otherwise), cleaving the sample in air is an acceptable substitute.

An interesting difference in the Mo 3d and S 2p core levels was observed between samples measured in Trondheim and samples measured in St. Andrews. While those measured in Trondheim were consistently found at binding energies matching literature values for MoS<sub>2</sub>, the same was not the case for those measured in St. Andrews. The Mo 3d and S 2p core levels were measured on two different clean MoS<sub>2</sub> samples in St. Andrews. In both cases they were found shifted towards lower binding energies, by 0.3eV in one case (displayed in Figure 4.2) and by 0.8eV in the other. There were two major differences to the measurements made in the separate locations which might aid in explaining the shift.

The first is the sample temperature. In Trondheim the measurements were made with the samples at room temperature, in St. Andrews on the other hand the samples were kept at 20K. Thus the observed shift may be a temperature effect, either related to the lattice parameters (thermal expan-

sion) or to some more subtle alterations to the electrostatic interactions of core electrons with their environment. Such effects, however, are small compared to the observed shift even for materials which exhibit greater thermal expansion (on the order of 10meV rather than 100)[87, 88]. Furthermore, there is the problem of the two samples, measured at the same temperature, displaying considerably different shifts.

The second major difference was the method employed to cleave the sample. In Trondheim all samples were cleaved using the scotch tape method, while all samples in St. Andrews were cleaved using the top-post method. This difference might cause the shift through a band bending effect arising from surface steps and dislocations. In MoS<sub>2</sub> the edge states at the steps have a metallic character[89] and can cause a shift to lower binding energies in the core and valence bands. Alternatively the shift may be caused by a surface electric field gradient imposed by charged dislocations. Similar results have already been observed in MoS<sub>2</sub> and presented in a paper[90]. The authors of this paper attribute the results to local Fermi level pinning effects arising from charged dislocations. However, the shifts observed in that work were larger than those observed in this experiment and persisted through an Ag film deposition. The latter led the authors to conclude that the metallic edge-atom states played little role in the origins of the shift, invoking instead the presence of negatively charged dislocations to explain the shift to lower binding energies.

If the sample did indeed have a high density of step defects this should show up in LEED patterns through spot splitting[91]. Accepting that the patterns of these samples, displayed in Figure 4.4, are true (i.e. not due to instrumental effects), they are consistent with this explanation. This explanation leads to the conclusion that the cleaves in St. Andrews were worse than those in Trondheim. Either through worse sample choices, improper cleaving methods or any combination thereof.

A third possible explanation is that the shifts arise through sample charging. This, however, is unlikely given the mounting method (silver epoxy) and previous studies showing no charging effects in MoS<sub>2</sub>[90].

As a final point about the sample characterization it is worth mentioning that the size and orientation of domains in the crystal could affect the observed spin texture. If, for example, one domain has spin polarization in one particular direction and the next has spin polarization in the opposite direction, these would average out to no spin polarization if the analysis area included both domains. It might therefore be interesting to examine the

domains more closely using different techniques (e.g. Transmission electron microscopy).

## 5.2 Fe Growth and Intercalation

Previous work done on Fe thermally evaporated onto MoS<sub>2</sub> can provide insights concerning its growth on the same substrate. It has been found that Fe is only weakly interacting with the MoS<sub>2</sub> surface, preferring to form nanoparticles nucleated on defect sites[51]. Starting out in an island growth mode, the coverage becomes more continuous with increasing amounts of Fe. Previous XPS measurements from the same paper showed the iron grew as a pure Fe state (Fe 2p 3/2 at 707eV) without any observable shift at the interface.

The results observed in this experiment are mostly consistent with this. As is seen in Figure 4.7 the deposition of Fe on the surface did not result in any major alterations to the sample's LEED pattern. The only noticeable difference was an increase in the diffuse background scattering, with higher amounts of Fe increasing the severity of this effect. This can signify a couple of different things. The absence of any new superstructure visible in the LEED patterns could mean that the Fe grows in a commensurate manner, with the same lattice spacings as the MoS<sub>2</sub> substrate. Considering the increase in the background, however, this appears unlikely. Instead, it is more likely that the Fe adsorbs amorphously on the surface, and that the amount employed in this experiment is not enough to by itself destroy the LEED pattern of the MoS<sub>2</sub>. The increase in the background with increasing amounts of Fe supports this claim.

XPS measurements of the Fe dosed samples were mostly in line with expectations. The Fe 2p 3/2 peak was observed at around 707eV, i.e. as pure, metallic Fe. Neither were any new components observed in the Mo 3d or S 2p peaks indicating the formation of new compounds. An interesting result was observed, however, in a sample dosed with large amounts of Fe (Figure 4.21). While the Fe 2p peak remains as metallic Fe, with no other clearly resolvable components, the same is not the case for the Mo 3d and S 2p peaks. In the Mo 3d peak a new component appears at 227.7eV, corresponding to the presence of metallic Mo. The S 2p peak has shifted towards lower binding energies compared to clean MoS<sub>2</sub> and is now found at 161.5eV, where one would expect to find this peak in FeS. Clearly, it appears that some of the Fe has reacted with the surface to form ferrous sulfide and metallic Mo. A curious

finding considering the Fe deposition was done at near room temperature before the sample was cooled to 20K. Assuming the reaction taking place is



a quick calculation of the standard-state free energy of reaction

$$\Delta G^\circ = \Delta H^\circ - T\Delta S^\circ \quad (5.2)$$

finds that this reaction does not occur spontaneously below 1094K. In this equation  $\Delta H^\circ$  is the standard enthalpy of reaction,  $\Delta S^\circ$  is the standard entropy change and  $T$  is temperature. Consistently with this, no similar changes were ever observed when annealing Fe dosed samples to temperatures up to 873K. A similar rough thermodynamical calculation reveals the reaction is endothermic, requiring 35.1kJ/mol or alternatively about 0.36eV per reaction. Considering the Fe atoms leave the doser with an energy corresponding to the thermal energy and assuming the Fe sphere is at 1800K (a generous estimate, right below the melting point of Fe) this puts a rough estimate of the average thermal energy at less than half of this (0.155eV). While not impossible it appears unlikely that it is this energy that drives the reaction. Nor was it observed in any other samples dosed with the same Fe doser but in lower quantities. It might also be that the quick reaction model presented here is inaccurate. Though a similar calculation for the reaction with Mn in place of Fe, finds that this reaction should be spontaneous at room temperature. This has been observed to be the case[92]. One possible explanation can be found in a study that concluded that in sulfur rich MoS<sub>2</sub> Fe is thermodynamically driven to form iron sulfides[93]. However, all measurements presented in this work were done on samples annealed to at least 923K before showing the presence of iron sulfides.

XPS measurements such as the ones in Figure 4.10 all showed a similar reduction in the Fe 2p peak associated with annealing. This indicates that the Fe on the surface is prone to thermal desorption.

On the possibility of intercalating the Fe into the MoS<sub>2</sub> previous studies indicate that incorporating magnetic ions into the fully crystallized compound is challenging[94]. It has, however, been demonstrated that annealing Fe dosed MoS<sub>2</sub> causes some of the Fe to intercalate and reside in the gaps between molecular layers[85]. Similar to the results of this experiment it was found that a large part of the Fe was thermally desorbed in the process. The intercalated Fe atoms were found to be restricted near the surface layers and

were suspected to form  $\text{FeMo}_2\text{S}_4$ [95]. Density functional theory calculations have confirmed that the intercalation site is among the most thermodynamically stable dopant sites in multilayer  $\text{MoS}_2$ [29].

ARXPS measurements on Fe dosed samples at room temperature, and samples annealed up to  $100^\circ\text{C}$ , all showed a similar dependence on sample tilt angle of the core levels as those in Figure 4.16 a). That is, a decrease in the areas of the substrate core levels (Mo and S) and an increase in the overlayer core level (Fe) at higher sample tilt angles. This is precisely what would be expected from a sample with a uniform Fe overlayer on top of a  $\text{MoS}_2$  substrate. The  $1/\cos(\theta)$  relationship displayed in Figure 4.17 a) is a particularly good representation of this. It arises because of the increasingly long path electrons coming from the bulk have to travel through to escape the sample as the sample tilt increases. As is illustrated by Figure 2.10 this length varies with the cosine of the sample tilt angle. This result indicates that the Fe film is relatively uniform and possibly hints that the growth occurs in the layer mode. However, scanning tunneling microscopy measurements of a previous study showed high coverage (small nanoparticles, spread out) even for small amounts of Fe on the surface[51]. In other words, no evidence of intercalation was seen on the samples at room temperature, or those annealed to temperatures below  $400^\circ$ .

The results on the samples annealed to higher temperatures were more promising. Following the annealing process an improvement in the sample's LEED pattern was generally observed. As is exemplified in Figure 4.14 the improvement typically included a lower background and sharper spots. This likely results from a reduction in the amount of material on top of the  $\text{MoS}_2$  surface. Although this could be taken as evidence of intercalation, likely the greater part of the improvement comes about from thermal desorption of the deposited Fe.

As can be seen in the spectra labelled by the number 5 in Figure 4.22 a)-c) the annealing process did not give rise to the appearance of any new components in the major core levels (Fe 2p, Mo 3d, S 2p). In other words no evidence of the Fe forming  $\text{FeMo}_2\text{S}_4$  was found in this experiment. If this compound were to be formed one would expect to see the appearance of new components in both the Fe 2p and Mo 3d peaks. Based on the valence states of Fe and Mo in  $\text{FeMo}_2\text{S}_4$  (+2 and +3 respectively), the new Fe 2p component would be expected to be shifted towards higher binding energies while the new Mo 3d component would be expected to be shifted towards lower binding energies. Although the absence of such observations does not

by itself rule out the possibility of intercalation it should be mentioned that different studies of Fe intercalated MoS<sub>2</sub> have also reported the Fe to be found in II and III oxidation states[96].

As presented in Figure 4.16 b) annealing the samples to temperatures of about 400°C changed the angular dependence of the core levels. Unlike what was the case before annealing, the areas of the Mo 3d, S 2p and Fe 2p peaks were now found to remain relatively constant at all sample tilt angles. This could be evidence for intercalation, as the intercalation process would naturally reduce the angle dependence of the overlayer and substrate peak areas. As is seen in Figure 4.17 b) the annealing also destroyed the  $1/\cos(\theta)$  relationship seen in the Fe/Mo peak area ratios prior to annealing. The main problem with concluding that the Fe intercalated is that only a very small amount of Fe remained on the sample after the annealing (as seen in XPS). For small coverages an island growth mode would also display less angular dependence. Unfortunately these samples were never exposed to atmosphere and then remeasured. Depending on how much of the Fe oxidized it would give a clear indication of whether it had intercalated or not. Alternatively the question can be decided by sputtering the sample and noting the changes in the Mo and Fe peak areas.

### 5.3 Film Thickness Estimation

As mentioned previously, all film thicknesses reported in this thesis were calculated using Equation 2.19. Due to the assumptions involved in deriving this expression, listed in Appendix A, it might not be entirely accurate under certain circumstances. The primary assumption which might cause trouble is of course the assumption of a continuous and flat overlayer. First of all, this will not be satisfied for any overlayer thicknesses less than a monolayer. In the context of this experiment a monolayer of Fe can be considered to correspond to an overlayer thickness of roughly 2.7Å. For amounts of Fe considerably less than this, there simply are not enough Fe atoms to ensure a continuous coverage. Furthermore, if the Fe growth does indeed proceed by the island mode, the overlayer will remain discontinuous even after deposition of several equivalent monolayers. In this case the thicknesses reported can both over and underestimate the amount of Fe on the sample, depending on the size and placement of the islands.

The expression in Equation 2.19 does not account for any potential pho-

toelectron diffraction effects either. Thus for samples where they are in fact present, such as the one in Figure 4.18, the calculated thickness may be inaccurate. It is, however, possible to calculate the film thickness at several sample tilt angles and perform an average. Naturally, the model does not account for any reactions which might cause the sample to deviate from the model (i.e. overlayer of material A on substrate of material B). The thickness reported for the sample in Figure 4.21, for example, is likely inaccurate due to the reaction happening at the surface.

Despite these issues it must be said that the thicknesses reported were very consistent with the deposition rates and times. At least for those samples dosed using the e-beam evaporator in Trondheim. Meaning that a set deposition time at a given deposition rate (as determined by a flux measurement of the e-beam evaporator) always produced roughly the same calculated thickness. The thicknesses reported should serve as a good estimate for the relative amount of Fe between different samples, even should they prove inaccurate.

It is for the reasons listed here that no film thicknesses were reported for the K depositions. Though it is a simple matter to extend the calculations in Appendix A to a case with two thin films on a substrate, the second deposition compounds the problems encountered with the first. Particularly due to the very small amounts of K used in the experiment. A better way to ensure the reproducibility of the results is to rely instead on the steady and consistent deposition rates of the alkali metal dispensers, controlled primarily by the current fed them.

## 5.4 Doping and Counter-doping

Over the course of the experiment several general shifts in the core level spectra were observed. Some of the more important of these will be summarized and discussed in this section.

The first point to be discussed will be the shifts observed from annealing a clean MoS<sub>2</sub> sample in stages to 683°C. Specifically, the shifts in the Mo 3d and S 2p core levels presented in Figure 4.11 a) and b). When heating the sample two successive shifts by 0.1eV towards higher binding energies were observed after heating the sample to 100°C and 400°C. In the final heating stage, to 683°C, a shift by 0.1eV back towards lower binding energies was observed. Importantly, these shifts were more or less identical in both the

Mo 3d and S 2p core levels, indicating that the shifts arise from final state effects as opposed to initial state effects. A clue to the potential origin of the shift is given by the ratio of the areas of the Mo and S peaks shown in Figure 4.11 c). As was noted in the previous chapter, the core level shifts occur simultaneously with changes in the relative amount of Mo and S. The shifts towards higher binding energies coincided with a reduction in the relative amount of Mo in the sample. Conversely, the shift toward lower binding energies coincided with a reduction in the relative amount of S in the sample. This latter result is similar to what was observed in a previous work which may shed some light on the situation. In this work it was found that annealing MoS<sub>2</sub> to temperatures above 200°C caused sulfur desorption in the sample[97]. The resulting sulfur vacancies were found to introduce surface states in the band gap which in turn caused a rigid shift in the core levels to lower binding energies due to upward band bending. It is possible that it is the same effect that causes the final shift observed in this data. Notably, the magnitude of the reported shift for bulk MoS<sub>2</sub> (0.15eV) matches well with the shift observed here. In a similar vein it could be that the formation of Mo vacancies could give rise to surface states which cause downward band bending. This hypothesis could be checked by measuring the valence bands with UPS or ARPES after annealing a clean sample.

The next point to be discussed is the effect of Fe deposition on the MoS<sub>2</sub> core levels. Here, two different trends were observed. Dosing samples with Fe in Trondheim consistently produced a shift towards lower binding energies in both the Mo 3d and S 2p core levels. The observed shift was identical in both core levels (see Figure 4.19) as well as in the valence bands (Figure 4.23). This indicates the shift is of electrostatic nature, and is consistent with the expected behavior due to surface doping. The magnitude of the observed shift was generally around 0.3-0.5eV and most often occurred in a single deposition step. That is, a shift was observed after deposition of a small amount of Fe, then no further shift was observed from depositing more Fe. This could be related to the previously reported tendency of Fe to nucleate at the more reactive defect sites at the MoS<sub>2</sub> surface[51]. After these sites are occupied by Fe, any further Fe deposited onto the sample will interact less with the MoS<sub>2</sub> surface. The change in the magnitude of the shift observed across different samples, seemingly unrelated to the amount of Fe deposited, could then be explained by different samples having different surface qualities (either as a result of the sample selection or from the cleave) with more or less such defect sites.

Doping samples with Fe in St. Andrews, however, produced nearly the opposite result. Here the deposition of Fe caused a comparatively smaller shift of the Mo 3d and S 2p towards higher binding energies rather than lower. And, while the shift was identical across both core levels, it did not match the shift observed in the valence bands (compare the middle core levels in Figure 4.20 with Figure 4.27). The different reaction to the Fe deposition is likely connected with the shift observed in the core levels of the clean samples measured in the same location. It could be that the dosing of Fe reduces the influence of potential metallic edge states, which would naturally induce a shift in the core levels towards lower binding energies. This would serve to shift the core levels back towards higher binding energies, towards where they are found in flat MoS<sub>2</sub>. Added to this would be the doping effect of the Fe observed in Trondheim. Consider the middle core level in Figure 4.20, a MoS<sub>2</sub> sample with a 1.3Å Fe overlayer. This is also the sample on which the ARPES spectrum in Figure 4.27 b) was taken. Compared to the clean sample the Mo 3d core level displays a shift of 0.04eV towards higher binding energies. If instead it is compared to the literature values for MoS<sub>2</sub>, 229.4-229.5eV, it displays a shift of 0.2-0.3eV towards lower binding energies, consistent with the magnitudes of the Fe doping shifts seen in Trondheim. The difference between the shift observed in the core levels and the one observed in the valence bands at the K points is trickier to explain. Compared to the spectrum of the clean sample, the bands display a shift of about 0.17eV towards higher binding energies. Because of the absence of any new components in the Mo 3d and S 2p peaks, and because the shift was the same for both peaks, it is unlikely the core level shift arises from the formation of new compounds. It can perhaps be explained through an inhomogeneous band bending effect arising from the defects.

The final point to be discussed in this section is the result of the K doping experiments. As exemplified by the LEED pattern in Figure 4.14 c), the deposition of K onto the sample had much the same effect on the LEED pattern as did the Fe deposition. That is, it did not give rise to any visible superstructures but rather served to increase the diffuse background scattering. As was concluded for the Fe, this indicates that the K adsorbs amorphously to the MoS<sub>2</sub> surface. A similar conclusion was reached in a previous work on Cs deposited on MoS<sub>2</sub>[50] as well as on WSe<sub>2</sub>[49]. The K deposition did not give rise to new components in any of the major core levels (i.e. Mo 3d, S 2p, Fe 2p). It did, however, cause a shift of about 1.5eV in the C 1s peak from 284.3eV to 285.8eV. This shift appeared with the first K deposition and did

not increase with successive depositions. Before K deposition the C 1s peak is found close to where the peak of adventitious carbon would be expected. The binding energy of the peak after the deposition could indicate a C-O-C type bond. It is possible that the K deposition results in the formation of some carbon/oxygen/potassium compound. There was no visible change in the O 1s peak as a result of the K deposition, though this peak was already located at a binding energy where O in C-O would be found. Such a reaction could explain how the carbon remains closest to the surface after successive Fe and K depositions as seen in the relative depth plot in Figure 4.15.

Though no drastic changes to the sample chemistry were observed, the K deposition did induce a shift in the Mo 3d, S 2p and Fe 2p core levels. As is shown in Figure 4.22 the first deposition of K successfully reversed the shift in the Mo and S core levels induced by the Fe deposition, and shifted them a further 0.2eV towards higher binding energies. This is along the lines of what would be expected as alkali metals adsorbed on MoS<sub>2</sub> are known to n-type dope it[98]. These results show that it is possible to counter-dope MoS<sub>2</sub> with K to reverse the doping shift induced by Fe deposition. The next K deposition shifted the core levels back towards lower binding energies, placing them more or less where they were before the Fe deposition. It is unclear why the second K deposition caused a shift in the opposite direction. Perhaps the alteration of the conditions at the surface somehow changed the type of the interaction of the K with the surface. Similar results to those presented in Figure 4.22 were observed in all of the experiments involving K deposition. When annealing the sample to 400°C a shift of 0.2eV was observed towards lower binding energies. The largest part of this shift can likely be explained by the thermal desorption of the K.

## 5.5 Band Structure Measurements

Among the experiments performed as part of this thesis were a couple of preliminary band structure measurements. These measurements were done on samples dosed with Fe, but which had not been heat treated. There were a couple of interesting take aways from these results.

First of all the ARPES measurements, both the ones taken using a 1D detector and the ones taken using a 2D detector, confirm the quality of the samples extracted from the naturally grown crystal. Samples from this crystal, and others like it, should serve as excellent candidates for further

investigations into the effects of magnetically doping TMDCs.

Second, it was observed across all samples that the Fe deposition caused a shift in the valence bands. For the spectra acquired Trondheim this shift (towards lower binding energies) matched the shift of the core levels due to the Fe deposition and can thus be attributed to a surface doping effect. The situation for the samples measured in St. Andrews is not as clear. Although the direction of the shift (towards higher binding energies) matched that of the core levels, its magnitude was greater by a factor of about 2.5. Furthermore, noticeably different results were obtained from different samples dosed with similar amounts of Fe. Compare the two K point spectra in Figure 4.27 b) and Figure 4.29. These are spectra of two different samples, one with a 1.3Å Fe overlayer and the other with a 1.2Å Fe overlayer. The former displays a shift by 0.17eV towards higher binding energies compared to the spectrum taken on the clean sample. While no measurements were made on the latter sample before Fe deposition, it is shifted by roughly 0.5eV towards higher binding energies compared to the other sample with similar amounts of Fe. Interestingly, this sample's Mo 3d core level is shifted by 0.2eV towards lower binding energies compared to the Mo 3d core level of the other sample. However, without measurements on the clean sample it is impossible to relate the shifts of the core and valence states with any certainty. In addition to this, the spectrum in Figure 4.29 appears to have an additional set of bands at a lower binding energy than the brightest feature. This may be the surface bands separating from the bulk bands due to the (electric) surface doping of the Fe. The differences observed between the two samples likely comes down to the quality of the respective sample surfaces, specifically the density and type of defects present.

In all measurements the addition of Fe to the surface caused the valence spectra to become more diffuse, the severity of which increased with increasing amounts of Fe. With as little as an 8Å Fe overlayer this effect was enough to render the bands too diffuse to be discerned. Essentially the same as what was observed in LEED, the effect is more pronounced in these measurements because of the increased surface sensitivity of ARPES.

If any alterations to the band structure of magnetic origin occurred it is hard to say from this data. Other than the extra feature in Figure 4.29, no evidence of band splitting was resolved. Nor was a change in the energy separation between the two valence bands at the K point observed.

## 5.6 Future work

Although the experiments in this thesis produced hints that the Fe intercalated into the  $\text{MoS}_2$ , it did not find conclusive evidence for it. The logical next step would be to confirm that Fe intercalation happens. To this end a sample could be dosed with a larger amount of Fe than what was common in this experiment (e.g.  $\approx 15\text{\AA}$ ), and annealed at  $>800\text{K}$  for a longer time period (on the time scale of about 1 hour). After this XPS and ARXPS measurements should be done to check for intercalation. Particular attention should be paid to the Fe 2p core level for the appearance of any oxidation states of Fe. If no oxidation states appear, the sample can be exposed to atmosphere as a complementary test of intercalation. Should too much Fe be lost to thermal desorption, Fe can be dosed in stages or directly onto the hot sample. In the event that Fe proves too difficult to intercalate into the  $\text{MoS}_2$ , other potential magnetic dopants can be explored, e.g. Ni and Mn. These should intercalate more uniformly into the  $\text{MoS}_2$ [85, 94].

Once a magnetic dopant has been successfully intercalated into the  $\text{MoS}_2$  detailed ARPES measurements should be made. Because any potentially resulting band splitting might be small, the final experiments might have to be done using synchrotron radiation. Other techniques such as spin-ARPES could reveal changes to the spin polarization of the valence bands. Again because the potential effects might be small this work would benefit from cooperation with a theoretical investigation (e.g. DFT calculations).

# Chapter 6

## Conclusion

All of the samples studied as part of this thesis were extracted from the same naturally grown MoS<sub>2</sub> crystal. These samples were found to contain few impurities and yielded excellent band structure measurements. They should be well suited as a platform for investigating the effects of magnetically surface doping TMDCs. It should be mentioned that slightly different behavior in the core levels and valence bands were seen across samples. This is believed to be due to defects introduced in the cleaving of the samples.

Fe thermally evaporated onto the MoS<sub>2</sub> surface was found to be only weakly interacting with it, easily desorbing during heating. For the quantities of Fe used in this experiment the growth appeared to be uniform. The areas of the Mo 3d and Fe 2p core levels displayed an angular dependence unlikely to be seen in a pure island growth mode. When deposited at room temperature, and when annealed at temperatures up to 100°C, the Fe did not show any signs of having intercalated into the MoS<sub>2</sub>. On Fe dosed samples annealed at higher temperatures (400°C+), ARXPS measurements revealed hints that the Fe may have intercalated. However, due to the small amounts of Fe remaining on the sample after the annealing process it cannot be concluded with any certainty that this was the case. Neither was the formation of any intercalation compounds observed.

In most cases the deposition of Fe onto the sample caused an identical shift (of a magnitude of about 0.5eV) in the Mo and S core levels and in the valence bands towards lower binding energies. This is consistent with the behavior expected from surface doping. It was additionally found that this shift could be reversed by deposition of K, a known electron dopant, onto the sample.

A series of preliminary band structure measurements were made on samples with Fe overlayers. The addition of Fe to the surface in all cases made the measured band structures more diffuse. Due to this, no clear evidence of band structure alterations due to magnetic effects were observed.

While the experiments in this thesis were conducted exclusively on MoS<sub>2</sub>, a number of the results can be expected to be relevant also for other TMDCs. As materials of this class largely have similar surface chemistry, the results concerning the growth and intercalation of the Fe, along with the K doping, should apply more or less also to all the other TMDCs. Any findings related to the band structure will be most relatable to the other group VI TMDCs.

# Bibliography

- [1] F.J. Clauss. *Solid lubricants and self-lubricating solids*. Elsevier, 2012.
- [2] Q.H. Wang, K. Kalantar-Zadeh, A. Kis, J.N. Coleman, and M.S. Strano. Electronics and optoelectronics of two-dimensional transition metal dichalcogenides. *Nature nanotechnology*, 7(11):699–712, 2012.
- [3] K.S. Novoselov, A.K. Geim, S.V. Morozov, D. Jiang, Y.-Zhang, S.V. Dubonos, I.V. Grigorieva, and A.A. Firsov. Electric field effect in atomically thin carbon films. *science*, 306(5696):666–669, 2004.
- [4] R. Peierls. Quelques propriétés typiques des corps solides. In *Annales de l'institut Henri Poincaré*, volume 5, pages 177–222, 1935.
- [5] L.D. Landau. Zur theorie der phasenumwandlungen ii. *Phys. Z. Sowjetunion*, 11:26–35, 1937.
- [6] G. Fiori, F. Bonaccorso, G. Iannaccone, T. Palacios, D. Neumaier, A. Seabaugh, S.K. Banerjee, and L. Colombo. Electronics based on two-dimensional materials. *Nature nanotechnology*, 9(10):768–779, 2014.
- [7] J.A. Wilson and A.D. Yoffe. The transition metal dichalcogenides discussion and interpretation of the observed optical, electrical and structural properties. *Advances in Physics*, 18(73):193–335, 1969.
- [8] H. Yuan, M.S. Bahramy, K. Morimoto, S. Wu, K. Nomura, B.J. Yang, H. Shimotani, R. Suzuki, M. Toh, C. Kloc, et al. Zeeman-type spin splitting controlled by an electric field. *Nature Physics*, 9(9):563–569, 2013.
- [9] G. Dresselhaus. Spin-orbit coupling effects in zinc blende structures. *Physical Review*, 100(2):580, 1955.

- [10] Y.A. Bychkov and E.I. Rashba. Properties of a 2d electron gas with lifted spectral degeneracy. *JETP lett*, 39(2):78, 1984.
- [11] S. Murakami, N. Nagaosa, and S. Zhang. Dissipationless quantum spin current at room temperature. *Science*, 301(5638):1348–1351, 2003.
- [12] J.P. Lu, J.B. Yau, S.P. Shukla, M. Shayegan, L. Wissinger, U. Rössler, and R. Winkler. Tunable spin-splitting and spin-resolved ballistic transport in gaas/algaas two-dimensional holes. *Physical review letters*, 81(6):1282, 1998.
- [13] J. Nitta, T. Akazaki, H. Takayanagi, and T. Enoki. Gate control of spin-orbit interaction in an inverted i n 0.53 g a 0.47 as/i n 0.52 a l 0.48 as heterostructure. *Physical Review Letters*, 78(7):1335, 1997.
- [14] A.D. Caviglia, M. Gabay, S. Gariglio, N. Reyren, C. Cancellieri, and J.M. Triscone. Tunable rashba spin-orbit interaction at oxide interfaces. *Physical review letters*, 104(12):126803, 2010.
- [15] R. Winkler. Spin orientation and spin precession in inversion-asymmetric quasi-two-dimensional electron systems. *Physical Review B*, 69(4):045317, 2004.
- [16] K. Gong, L. Zhang, D. Liu, L. Liu, Y. Zhu, Y. Zhao, and H. Guo. Electric control of spin in monolayer wse<sub>2</sub> field effect transistors. *Nanotechnology*, 25(43):435201, 2014.
- [17] Z.Y. Zhu, Y.C. Cheng, and U. Schwingenschlögl. Giant spin-orbit-induced spin splitting in two-dimensional transition-metal dichalcogenide semiconductors. *Physical Review B*, 84(15):153402, 2011.
- [18] Y. Saito, Y. Nakamura, M.S. Bahramy, Y. Kohama, J. Ye, Y. Kasahara, Y. Nakagawa, M. Onga, M. Tokunaga, T. Nojima, et al. Superconductivity protected by spin-valley locking in ion-gated mos<sub>2</sub>. *Nature Physics*, 2015.
- [19] D. Xiao, G.B. Liu, W. Feng, X. Xu, and W. Yao. Coupled spin and valley physics in monolayers of mos<sub>2</sub> and other group-vi dichalcogenides. *Physical Review Letters*, 108(19):196802, 2012.

- [20] J.M. Riley, F. Mazzola, M. Dendzik, M. Michiardi, T. Takayama, L. Bawden, C. Granerød, M. Leandersson, T. Balasubramanian, M. Hoesch, et al. Direct observation of spin-polarized bulk bands in an inversion-symmetric semiconductor. *Nature Physics*, 10(11):835–839, 2014.
- [21] L. Bawden, S.P. Cooil, F. Mazzola, J.M. Riley, L.J. Collins-McIntyre, V. Sunko, K.W.B. Hunvik, M. Leandersson, C.M. Polley, T. Balasubramanian, et al. Spin-valley locking in the normal state of a transition-metal dichalcogenide superconductor. *Nature communications*, 7, 2016.
- [22] X. Zhang, Q. Liu, J.W. Luo, A.J. Freeman, and A. Zunger. Hidden spin polarization in inversion-symmetric bulk crystals. *Nature Physics*, 10(5):387–393, 2014.
- [23] D. Xiao, W. Yao, and Q. Niu. Valley-contrasting physics in graphene: magnetic moment and topological transport. *Physical Review Letters*, 99(23):236809, 2007.
- [24] A.R. Akhmerov and C.W.J. Beenakker. Detection of valley polarization in graphene by a superconducting contact. *Physical review letters*, 98(15):157003, 2007.
- [25] K.F. Mak, K. He, J. Shan, and T.F. Heinz. Control of valley polarization in monolayer  $\text{mos}_2$  by optical helicity. *Nature nanotechnology*, 7(8):494–498, 2012.
- [26] H. Zeng, J. Dai, W. Yao, D. Xiao, and X. Cui. Valley polarization in  $\text{mos}_2$  monolayers by optical pumping. *Nature nanotechnology*, 7(8):490–493, 2012.
- [27] W. Yao, D. Xiao, and Q. Niu. Valley-dependent optoelectronics from inversion symmetry breaking. *Physical Review B*, 77(23):235406, 2008.
- [28] R. Suzuki, M. Sakano, Y.J. Zhang, R. Akashi, D. Morikawa, A. Harasawa, K. Yaji, K. Kuroda, K. Miyamoto, T. Okuda, et al. Valley-dependent spin polarization in bulk  $\text{mos}_2$  with broken inversion symmetry. *Nature nanotechnology*, 9(8):611–617, 2014.
- [29] H. Shu, P. Luo, P. Liang, D. Cao, and X. Chen. Layer-dependent dopant stability and magnetic exchange coupling of iron-doped  $\text{mos}_2$

- nanosheets. *ACS applied materials & interfaces*, 7(14):7534–7541, 2015.
- [30] Z. Zhang, X. Zou, V.H. Crespi, and B.I. Yakobson. Intrinsic magnetism of grain boundaries in two-dimensional metal dichalcogenides. *ACS nano*, 7(12):10475–10481, 2013.
- [31] S. Mathew, K. Gopinadhan, T.K. Chan, X.J. Yu, D. Zhan, L. Cao, A. Rusydi, M.B.H. Breese, S. Dhar, Z.X. Shen, et al. Magnetism in  $\text{mos}_2$  induced by proton irradiation. *Applied Physics Letters*, 101(10):102103, 2012.
- [32] H. Shi, H. Pan, Y.W. Zhang, and B.I. Yakobson. Strong ferromagnetism in hydrogenated monolayer  $\text{mos}_2$  tuned by strain. *Physical Review B*, 88(20):205305, 2013.
- [33] Y. Li, Z. Zhou, S. Zhang, and Z. Chen.  $\text{Mos}_2$  nanoribbons: high stability and unusual electronic and magnetic properties. *Journal of the American Chemical Society*, 130(49):16739–16744, 2008.
- [34] D. Gao, M. Si, J. Li, J. Zhang, Z. Zhang, Z. Yang, and D. Xue. Ferromagnetism in freestanding  $\text{mos}_2$  nanosheets. *Nanoscale research letters*, 8(1):1–8, 2013.
- [35] Q. Chen, Y. Ouyang, S. Yuan, R. Li, and J. Wang. Uniformly wetting deposition of co atoms on  $\text{mos}_2$  monolayer: A promising two-dimensional robust half-metallic ferromagnet. *ACS applied materials & interfaces*, 6(19):16835–16840, 2014.
- [36] S.Y. Wang, T.S. Ko, C.C. Huang, Y.S. Huang, et al. Optical and electrical properties of  $\text{mos}_2$  and fe-doped  $\text{mos}_2$ . *Japanese Journal of Applied Physics*, 53(4S):04EH07, 2014.
- [37] D. Naveh and A. Ramasubramaniam. Mn-doped monolayer  $\text{mos}_2$ : An atomically thin dilute magnetic semiconductor. In *APS Meeting Abstracts*, volume 1, page 48004, 2014.
- [38] Y.C. Cheng, Z.Y. Zhu, W.B. Mi, Z.B. Guo, and U. Schwingenschlöggl. Prediction of two-dimensional diluted magnetic semiconductors: doped monolayer  $\text{mos}_2$  systems. *Physical Review B*, 87(10):100401, 2013.

- [39] Y.C. Cheng, Q.Y. Zhang, and U. Schwingenschlögl. Valley polarization in magnetically doped single-layer transition-metal dichalcogenides. *Physical Review B*, 89(15):155429, 2014.
- [40] R.J. Newberry. Polytypism in molybdenite (i); a non-equilibrium impurity-induced phenomenon. *American mineralogist*, 64(7-8):758–767, 1979.
- [41] J.W. Frondel and F.E. Wickman. Molybdenite polytypes in theory and occurrence. ii. some naturally-occurring polytypes of molybdenite. *THE AMERICAN MINERALOGIST*, 55, 1970.
- [42] K.K. Kam and B.A. Parkinson. Detailed photocurrent spectroscopy of the semiconducting group vib transition metal dichalcogenides. *The Journal of Physical Chemistry*, 86(4):463–467, 1982.
- [43] J.A. Venables, G.D.T. Spiller, and M. Hanbucken. Nucleation and growth of thin films. *Reports on Progress in Physics*, 47(4):399, 1984.
- [44] C. Argile and G.E. Rhead. Adsorbed layer and thin film growth modes monitored by auger electron spectroscopy. *Surface Science Reports*, 10(6-7):277–356, 1989.
- [45] K. Reichelt. Nucleation and growth of thin films. *Vacuum*, 38(12):1083–1099, 1988.
- [46] J.M. Thomas and E.L. Evans. Enhanced reactivity at dislocations in layer structures. *Nature*, 1967.
- [47] W. Kautek and H. Gerischer. Anisotropic photocorrosion of n-type  $\text{mos}_2$   $\text{mose}_2$ , and  $\text{wse}_2$  single crystal surfaces: the role of cleavage steps, line and screw dislocations. *Surface Science*, 119(1):46–60, 1982.
- [48] W. Jaegermann and D. Schmeisser. Reactivity of layer type transition metal chalcogenides towards oxidation. *Surface science*, 165(1):143–160, 1986.
- [49] S. Ladas, S. Kennou, M. Kamaratos, S.D. Foulas, and C. Papageorgopoulos. The adsorption of cs on  $\text{wse}_2$ . *Surface Science*, 189:261–267, 1987.

- [50] S. Kennou, S. Ladas, and C. Papageorgopoulos. The behavior of cs on mos<sub>2</sub>. *Surface Science*, 152:1213–1221, 1985.
- [51] H.C. Hsu, C.B. Wu, K.L. Hsu, P.C. Chang, T.Y. Fu, V. R. Mudinepalli, and W.C. Lin. Surface morphology, magnetism and chemical state of fe coverage on mos<sub>2</sub> substrate. *Applied Surface Science*, 357:551–557, 2015.
- [52] H. Hertz. Ueber einen Einfluss des ultravioletten Lichtes auf die elektrische Entladung. *Annalen der Physik*, 267:983–1000, 1887.
- [53] A. Einstein. Über einen die erzeugung und verwandlung des lichtes betreffenden heuristischen gesichtspunkt. *Annalen der Physik*, 322(6):132–148, 1905.
- [54] J.B. Metson. Charge compensation and binding energy referencing in xps analysis. *Surface and interface analysis*, 27(12):1069–1072, 1999.
- [55] G. Barth, R. Linder, and C. Bryson. Advances in charge neutralization for xps measurements of nonconducting materials. *Surface and Interface Analysis*, 11(6-7):307–311, 1988.
- [56] P.J. Feibelman and D.E. Eastman. Photoemission spectroscopy — correspondence between quantum theory and experimental phenomenology. *Physical Review B*, 10(12):4932, 1974.
- [57] S. Hüfner. *Photoelectron spectroscopy: principles and applications*. Springer Science & Business Media, 2013.
- [58] M.P. Seah and W.A. Dench. Quantitative electron spectroscopy of surfaces: a standard data base for electron inelastic mean free paths in solids. *Surface and interface analysis*, 1(1):2–11, 1979.
- [59] P. Hofmann. *Surface Physics: An Introduction*. Philip Hofmann, 2013.
- [60] J. Schnadt, J. Knudsen, J.N. Andersen, H. Siegbahn, A. Pietzsch, F. Hennies, N. Johansson, N. Mårtensson, G. Öhrwall, S. Bahr, et al. The new ambient-pressure x-ray photoelectron spectroscopy instrument at max-lab. *Journal of synchrotron radiation*, 19(5):701–704, 2012.

- [61] M. Salmeron and R. Schlögl. Ambient pressure photoelectron spectroscopy: A new tool for surface science and nanotechnology. *Surface Science Reports*, 63(4):169–199, 2008.
- [62] D.F. Ogletree, H. Bluhm, E.D. Hebenstreit, and M. Salmeron. Photoelectron spectroscopy under ambient pressure and temperature conditions. *Nuclear Instruments and Methods in Physics Research Section A: Accelerators, Spectrometers, Detectors and Associated Equipment*, 601(1):151–160, 2009.
- [63] A. Damascelli. Probing the electronic structure of complex systems by arpes. *Physica Scripta*, 2004(T109):61, 2004.
- [64] W. Schattke. Photoemission within and beyond the one-step model. *Progress in Surface Science*, 54(3):211–227, 1997.
- [65] C.N. Berglund and W.E. Spicer. Photoemission studies of copper and silver: theory. *Physical Review*, 136(4A):A1030, 1964.
- [66] REB. Makinson. The surface photoelectric effect. *Physical Review*, 75(12):1908, 1949.
- [67] J.J. Barton. Photoelectron holography. *Phys. Rev. Lett.*, 61:1356–1359, Sep 1988.
- [68] L. Hedin and J.D. Lee. Sudden approximation in photoemission and beyond. *Journal of Electron Spectroscopy and Related Phenomena*, 124(2–3):289 – 315, 2002.
- [69] N.V. Smith, P. Thiry, and Y. Petroff. Photoemission linewidths and quasiparticle lifetimes. *Physical Review B*, 47(23):15476, 1993.
- [70] A. Bödicker and W. Schattke. Theoretical photoemission line shapes and many body correlations. *Journal of electron spectroscopy and related phenomena*, 76:265–270, 1995.
- [71] C. Nordling, E. Sokolowski, and K. Siegbahn. Precision method for obtaining absolute values of atomic binding energies. *Phys. Rev.*, 105:1676–1677, Mar 1957.
- [72] J.F. Watts and J. Wolstenholme. *An Introduction to Surface Analysis by XPS and AES*. Wiley Online Library, 2004.

- [73] C.D. Wagner, W.M. Riggs, L.E. Davis, J.F. Moulder, and G.E. Muilenberg. Handbook of x-ray photoelectron spectroscopy: A reference book of standard spectra for identification and interpretation of xps data. *Perkin-Elmer Corporation*, 1979.
- [74] A. Jablonski and C.J. Powell. Relationships between electron inelastic mean free paths, effective attenuation lengths, and mean escape depths. *Journal of electron spectroscopy and related phenomena*, 100(1):137–160, 1999.
- [75] J.B. Pendry. *Low Energy Electron Diffraction: The Theory and Its Application to Determination of Surface Structure*. Techniques of Physics Series. Academic Press, 1974.
- [76] M.A. VanHove, W.H. Weinberg, and C. Chan. *Low-energy electron diffraction: experiment, theory and surface structure determination*, volume 6. Springer Science & Business Media, 2012.
- [77] X. Li, Z. Zhang, and V.E. Henrich. Inelastic electron background function for ultraviolet photoelectron spectra. *Journal of electron spectroscopy and related phenomena*, 63(3):253–265, 1993.
- [78] D.A. Shirley. High-resolution x-ray photoemission spectrum of the valence bands of gold. *Physical Review B*, 5(12):4709, 1972.
- [79] S. Tougaard. Practical algorithm for background subtraction. *Surface Science*, 216(3):343–360, 1989.
- [80] J.E. Castle and A.M. Salvi. Interpretation of the shirley background in x-ray photoelectron spectroscopy analysis. *Journal of Vacuum Science & Technology A*, 19(4):1170–1175, 2001.
- [81] S. Doniach and M. Sunjic. Many-electron singularity in x-ray photoemission and x-ray line spectra from metals. *Journal of Physics C: Solid State Physics*, 3(2):285, 1970.
- [82] M. Schmid, H.P. Steinrück, and J. M. Gottfried. A new asymmetric pseudo-voigt function for more efficient fitting of xps lines. *Surface and Interface Analysis*, 46(8):505–511, 2014.

- [83] National Institute of Standards and Technology. X-ray photoelectron spectroscopy database, version 4.1, 2012.
- [84] C.J. Powell and A. Jablonski. The nist electron effective-attenuation-length database. *Journal of Surface Analysis*, 9(3):322–325, 2002.
- [85] M. Kamaratos and C. Papageorgopoulos. Intercalation of mos<sub>2</sub> (0001) with fe, ni and pd. *Solid state communications*, 61(9):567–569, 1987.
- [86] X. Fan, D.J. Singh, and W. Zheng. Valence band splitting on multi-layer mos<sub>2</sub>: Mixing of spin–orbit coupling and interlayer coupling. *The Journal of Physical Chemistry Letters*, 7:2175–2181, 2016.
- [87] D.M. Riffe, W. Hale, B. Kim, and J.L. Erskine. Thermally induced core-electron binding-energy shifts in transition metals: An experimental investigation of ta (100). *Physical Review B*, 54(23):17118, 1996.
- [88] D.M. Riffe, G.K. Wertheim, D.N.E. Buchanan, and P.H. Citrin. Thermal and surface core-electron binding-energy shifts in metals. *Physical Review B*, 45(11):6216, 1992.
- [89] M.V. Bollinger, J.V. Lauritsen, K.W. Jacobsen, J.K. Nørskov, S. Helveg, and F. Besenbacher. One-dimensional metallic edge states in mos<sub>2</sub>. *Physical review letters*, 87(19):196803, 2001.
- [90] S.K. Mahatha and K.S.R. Menon. Inhomogeneous band bending on mos<sub>2</sub> (0001) arising from surface steps and dislocations. *Journal of Physics: Condensed Matter*, 24(30):305502, 2012.
- [91] M. Henzler. Leed-investigation of step arrays on cleaved germanium (111) surfaces. *Surface Science*, 19(1):159–171, 1970.
- [92] S.V. Didziulis and P.D. Fleischauer. Applications of surface science to solid lubricants. *Surface Diagnostics in Tribology—Fundamental Principles and Applications, Series in Modern Tribology*, 1:135–182, 1993.
- [93] J.S. Zabinski, T. George, and B.J. Tatarchuk. Chemical reactivity at buried-interfaces: Ii. iron on nonstoichiometric and/or defected molybdenite. *Surface science*, 241(1-2):171–189, 1991.

- [94] T.E. Kidd, A. O'Shea, Z. Griffith, S. Leslie, P.M. Shand, K.R. Boyle, and L.H. Strauss. Synthesis of magnetic 1d dichalcogenide nanostructures. *Journal of Nanoparticle Research*, 14(6):1–10, 2012.
- [95] T. Bakas and H.H.J. Gangas. Mossbauer investigation of the layered compound  $\text{femO}_2\text{S}_4$ . *Journal of Physics C: Solid State Physics*, 13(22):L561, 1980.
- [96] M. Danot, J.L. Mansot, A.S. Golub, G.A. Protzenko, P.B. Fabritchnyi, Y.N. Novikov, and J. Rouxel. Iron-intercalated molybdenum disulfide obtained from single-layer dispersion. *Materials research bulletin*, 29(8):833–841, 1994.
- [97] M. Donarelli, F. Bisti, F. Perrozzi, and L. Ottaviano. Tunable sulfur desorption in exfoliated  $\text{mos}_2$  by means of thermal annealing in ultra-high vacuum. *Chemical Physics Letters*, 588:198–202, 2013.
- [98] K. Dolui, I. Rungger, C.D. Pemmaraju, and S. Sanvito. Possible doping strategies for  $\text{mos}_2$  monolayers: An ab initio study. *Physical Review B*, 88(7):075420, 2013.
- [99] R. Hesse, P. Streubel, and R. Szargan. Improved accuracy of quantitative xps analysis using predetermined spectrometer transmission functions with unifit 2004. *Surface and interface analysis*, 37(7):589–607, 2005.
- [100] M.P. Seah and D. Briggs. *Practical Surface Analysis: Auger and X-ray Photoelectron Spectroscopy*. John Wiley & Sons, 1990.
- [101] F. Song, Å.F. Monsen, Z.S. Li, J.W. Wells, and E. Wahlström. The layer-by-layer stoichiometry of  $\text{la}_0.7\text{sr}_0.3\text{mno}_3/\text{srtio}_3$  thin films and interfaces. *Surface and Interface Analysis*, 45(7):1144–1147, 2013.

# Appendix A

## Film Thickness

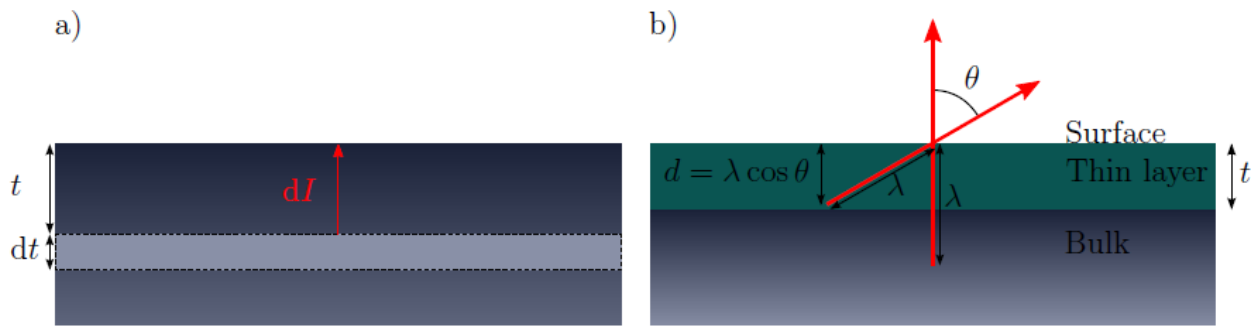


Figure A.1: Illustrations of a couple of basic concepts important to ARXPS. (a) A layer of material of thickness  $dt$  at a depth  $t$ , gives rise to a photoemission intensity  $dI$  in a direction parallel to the surface normal. (b) A thin overlayer of a material of thickness  $t$  on a bulk material. It illustrates how the probing depth  $d$  varies with the emission angle.

Consider the situation presented in Figure A.1 a), of a material irradiated with photons of sufficient energy to induce photoemission. In this material, a layer of thickness  $dt$  at a depth  $t$  will give rise to a photoemission intensity  $dI$  in a direction parallel to the surface normal. This intensity can be written

$$dI = Cdt, \tag{A.1}$$

where  $C$  is a constant determined by various factors related both to the material and to the experimental conditions. On its way out of the sample

this intensity will be attenuated according to the Beer-Lambert law. At the surface the intensity will be

$$dI = C \exp(-t/\lambda)dt, \quad (\text{A.2})$$

where  $\lambda$  is the attenuation length of the electrons in the material. For electrons collected at an angle  $\theta$  with respect to the surface normal this expression instead becomes

$$dI = C \exp(-t/\lambda \cos \theta)dt \quad (\text{A.3})$$

as is seen from the geometry in Figure A.1 b). By integrating Equation A.2 from 0 to infinity one obtains

$$I^\infty = \int_0^\infty C \exp(-t/\lambda)dt = C\lambda, \quad (\text{A.4})$$

the photoemission intensity at normal emission of an infinitely thick sample (or a bulk sample for which  $t \gg \lambda$ ). For a given material and a specified photoelectron kinetic energy  $E$ , determined by the photon energy and the originating core level, this intensity is given by[99, 100]

$$I^\infty = N\sigma\lambda(E)T(E). \quad (\text{A.5})$$

Here  $N = N_0\rho/A$  is the atomic density ( $N_0$  is Avogadro's constant,  $\rho$  is the density of the material and  $A$  is the relative atomic mass),  $\sigma$  is the photoionization cross-section of the specified core level at the employed photon energy,  $\lambda(E)$  is the effective attenuation length of electrons with energy  $E$  in the material, and  $T(E)$  is the transmission function of the spectrometer used.

Consider now the situation presented in Figure A.1 b), of a thin layer of material A of thickness  $t$  on top of a substrate B. The photoelectron signal from A is obtained by integrating Equation A.3 from 0 to  $t$  and is

$$I_A = I_A^\infty [1 - \exp(-t/\lambda_{A,A} \cos \theta)] \quad (\text{A.6})$$

where  $\lambda_{A,A}$  is the effective attenuation length of an electron emitted in material A in that material. Assuming the thickness of B is large compared to  $\lambda_{B,B}$ , the signal from B arriving at the B-A interface is  $I_B^\infty$ . This signal is then attenuated by passing through the overlayer A and becomes

$$I_B = I_B^\infty \exp(-t/\lambda_{B,A} \cos \theta). \quad (\text{A.7})$$

Finally, by taking the ratio of the signal intensities from the overlayer and the substrate one obtains

$$\frac{I_A}{I_B} = \frac{I_A^\infty [1 - \exp(-t/\lambda_{A,A} \cos \theta)]}{I_B^\infty \exp(-t/\lambda_{B,A} \cos \theta)}. \quad (\text{A.8})$$

If both the intensities  $I_A$  and  $I_B$  are measured, this equation can be solved for the film thickness.

The result reached in Equation A.8 hinges on a number of simplifying assumptions. First, it is assumed that the intensity of the exciting radiation remains constant in the analyzed volume. Second, the layers are assumed to be homogeneous. That is, both the atomic densities and electron attenuation lengths are assumed to be constant within the layers. The latter are also assumed to be independent of the direction of analysis. Furthermore, the layers are assumed to be flat and continuous. Finally, no photoelectron diffraction effects have been accounted for.

The basic concepts presented here can be extended and used to make more complex models. For example it is possible to make a model calculating the layer by layer stoichiometry and chemical state of materials, which can then be compared with measured data[101].